An Electronic Model of the ATLAS Phase-1 Upgrade Hadronic Endcap Calorimeter Front End Crate Baseplane

by

Ryan Porter
B.Sc., University of Victoria, 2013

A Thesis Submitted in Partial Fulfillment of the
Requirements for the Degree of

MASTER OF SCIENCE

in the Department of Physics and Astronomy

An Electronic Model of the ATLAS Phase-1 Upgrade Hadronic Endcap Calorimeter Front End Crate Baseplane

by

Ryan Porter
B.Sc., University of Victoria, 2013

Supervisory Committee

Dr. R. Keeler, Supervisor
(Department of Physics and Astronomy)

Dr. R. McPherson, Departmental Member
(Department of Physics and Astronomy)

Dr. R. Sobie, Departmental Member
(Department of Physics and Astronomy)

Supervisory Committee

Dr. R. Keeler, Supervisor
(Department of Physics and Astronomy)

Dr. R. McPherson, Departmental Member
(Department of Physics and Astronomy)

Dr. R. Sobie, Departmental Member
(Department of Physics and Astronomy)

ABSTRACT

This thesis presents an electrical model of two pairs of interconnects of the ATLAS Phase-1 Upgrade Hadronic Endcap Front End Crate prototype baseplane. Stripline transmission lines of the baseplane are modeled using Keysight Technologies' Electromagnetic Professional's (EMPro) 3D electromagnetic simulation (Finite Element Method) and the connectors are modeled using built-in models in Keysight Technologies' Advanced Design System (ADS). The model is compared in both the time and frequency domain to measured Time Domain Reflectometer (TDR) traces and S-parameters. The S-parameters of the model are found to be within 5% of the measured S-parameters for transmission and reflection, and range from 25% below to 100% above for forward and backward crosstalk. To make comparisons with measurements, the cables used to connect the prototype HEC baseplane to the measurement system had to be included in the model. Plots of the S-parameters of a model without these cables are presented for one pair of interconnects for which the crosstalk is expected to be the higher than most other interconnects of the baseplane.

Contents

List of Tables

List of Figures

List of Abbreviations

ADS	Advanced Design System (Electronic design and simulation software)
EM	Electromagnetic
EMPro	Electromagnetic Professional (3D electromagnetic simulation software)
ERNI Connector	The connector used for the LTDB
$\mathbf{E_T}$	Transverse Energy
FCI Connector	The connector used for the FEB and TDB
FEB	Front End Board
FEM	Finite Element Method
HEC	Hadronic Endcap Calorimeter
LAr	Liquid Argon (Referring to a set of calorimeters on the ATLAS detector that use Liquid Argon technology)
LHC	Large Hadron Collider
LTDB	LAr Trigger Digitizer Board
$\mathbf{p_T}$	Transverse Momentum
TDB	Tower Driver Board
TDR	Time Domain Reflectometer, Time Domain Reflectometry or Time Domain Reflection
TDT	Time Domain Transmission

ACKNOWLEDGEMENTS

I would like to thank my supervisor, Dr. Richard Keeler. His advice has been crucial in conducting this research and in shaping my future career. I would also like to thank my committee members, Dr. Robert McPherson and Dr. Randall Sobie, for taking the time to read my thesis and agreeing to examine me.

There are several people who must be thanked for their contributions to this work: Dr. Paul Poffenberger for his assistance in learning to use EMPro and IConnect, setting up and acquiring equipment, and his advice on various aspects of this research; Nicolas Braam for creating the patch cables; Colin Leavett-Brown for assistance with acquiring and using computer equipment; and Dr. Leonid Kurchaninov for the advice and knowledge he provided throughout this research.

Finally, I would like to thank my friends and family for their love and support. My apologies for the many occasions during which I was too busy to see you. Special thanks to my mother, Jacqueline, and Hannah, who have been tremendously encouraging and supportive throughout my master's degree.

DEDICATION

Dedicated to my mother and father.

Chapter 1

Introduction

This thesis is about modeling a prototype baseplane for the ATLAS Hadronic Endcap Calorimeter front end electronic crates. The baseplane is part of an upgrade of the ATLAS detector at the European Organization for Nuclear Research (CERN). ATLAS is one of four multi-purpose detectors at the Large Hadron Collider (LHC), the most powerful particle collider in the world. The data gathered using the ATLAS detector during the first run (that ended in 2012) was used to establish the existence of the Higgs boson [1], a particle predicted by the Standard Model.

Although the Higgs boson has been discovered–one of the reasons for building the Large Hadron Collider and the ATLAS detector–the particle discovered may have properties that are different from the Standard Model theoretical descriptions; many non-Standard Model theories have a particle similar to the Higgs boson, but not exactly the same. There are many other unsolved problems in particle physics which are being explored using the LHC and the ATLAS detector. The ATLAS detector could discover what dark matter is. Evidence for a variety of popular theoretical models, such as supersymmetry, could also be revealed.

During the current run (2015 to 2017) the LHC will start at 6.5 TeV/beam and then the beam energy will be increased to its nominal design energy of 7 TeV/beam and its nominal luminosity[1]. The increase in the energy of the beam could lead to whole new processes becoming energetically favourable, potentially leading to new

[1]The luminosity, L $[cm^{-2}s^{-1}]$, is the number of particles per unit area per unit time where the counter rotating beams intersect each other. The event rate, N, for a process is the cross section of that process, σ, times the luminosity [2, p. 194].

$$N = \sigma L \tag{1.1}$$

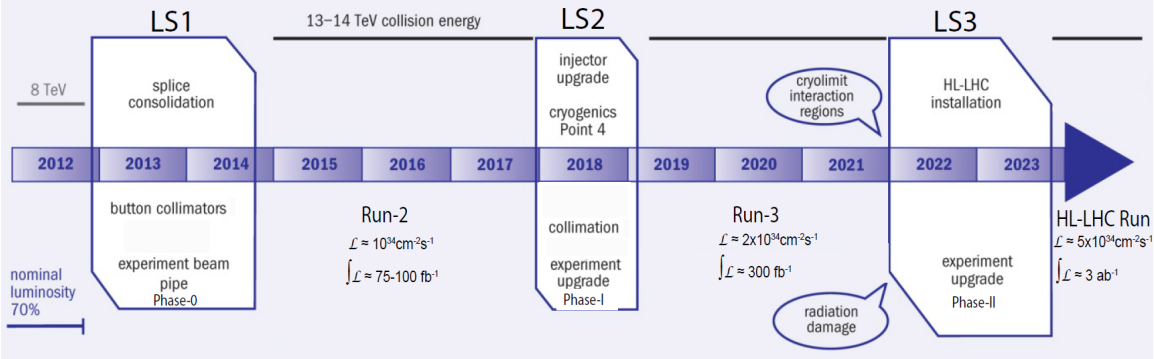

Figure 1.1: A timeline of the Large Hadron Collider showing runs, long shutdown periods and expected beam energies and luminosities [3, p. 3].

physics discoveries. Unfortunately, the maximum field produced by the bending magnets (8 T) limits the energy of the LHC to the current design energy. Increasing the luminosity, the density of particles in bunches, however, is possible. Higher density bunches produce more interactions per collision, improving the likelihood of an interesting interaction occurring. The more likely an interaction is to occur, the faster data can be gathered to confirm new phenomena. Not only does this increase the speed at which particle physics discoveries occur, it also pushes the limit of accelerator technology, advancing that field. This form of increase is being pursued and the luminosity in the 2019 run is expected to be above the nominal design value (see figure 1.1 for the energy and luminosity schedule of the LHC).

The ATLAS detector was only designed for the nominal energies and beam intensities which will be achieved in Run 2 (current run lasting until the end of 2017). The increased luminosity will cause problems for the triggering system of ATLAS–the subsystem which determines which collisions are recorded.

Bunch crossings in the ATLAS detector occur at a very high rate (one bunch crossing every 25 ns) [4]. The inelastic non-diffractive cross section for proton-proton (p-p) collisions is sufficiently high that there are multiple collisions at each beam crossing even at the design luminosity. Recording every event would be impossible to implement and would present data storage problems (this would generate terabytes of data each second). Most of the collisions do not have any interesting interactions so, instead, a triggering system is used to decide which of the collisions are interesting enough to be recorded within a 400 Hz limit (during run 1, increasing to 1000 Hz in run 2). This is a 3 tiered system (level 1 trigger, level 2 trigger and event filter) where each tier must select a subset of the events given to it by the last system, but

has more time to process events. Because collisions occur every 25 ns, the first level of this system, the level 1 trigger, must make decisions very quickly. This limits the amount of inline processing that can applied to the data for decision making. Because of this, the level 1 trigger is limited in how much analysis can be applied to the data and works with data where groups of individual detector cells have been summed together (coarser granularity) to reduce the number of channels analyzed.

For the calorimeter part of the level 1 trigger, the increased luminosity will cause the rate of events that look like electrons to become too large (80 kHz electron signal and only 100 kHz maximum acceptance) [5]. Increasing the transverse momentum threshold (23 GeV to 40-45 GeV) of this trigger could be used to decrease the trigger rate, but the increase required would eliminate most of the signal from W and Z bosons and potentially make the detector insensitive to other undiscovered processes expected in the same energy range. The Higgs mass is 125 GeV, so the increase would eliminate much of its signal. Requiring isolation of electrons from other events could decrease the rate, but not enough to avoid a significant increase to the transverse momentum threshold.

Luckily, most of the excess signal is caused by low transverse momentum[2] (p_T) jets that the level 1 trigger is identifying as electrons. Improving the ability for the level 1 trigger to discriminate against this type of event could allow the electron trigger rate to be decreased to an acceptable level without increasing the transverse momentum threshold. The high level triggers employ shower shape algorithms to make this distinction. These algorithms require finer granularity information from the detector, particularly in depth (radially away from the interaction point). This requires less summation of signals, increasing the number of signals that need to be processed, and requires more inline processing. More signals would require more electronics on the detector, where space cannot be increased, and more processing in the level 1 trigger (off detector). However, the detector was designed in the 1990's, and faster inline processing and higher density electronics have since been developed. The increased speed allows for more sophisticated data processing in the level 1 trigger, while higher density electronics allows for more channels of the detector to be analyzed individually rather than being summed together. The purpose of the Liquid Argon Phase-1 Upgrade is to upgrade the electronics of the level 1 trigger during the second long shutdown (2018) and employ more advanced event selection in order to cope with the increased luminosity.

[2]The momentum in the plane transverse to the beam direction.

Higher density electronics can lead to other issues. Increasing the number of signals sent through the same space can increase the distortion of the signals and increase the amount of crosstalk between neighbouring signal lines. The old and new triggering systems measure the amplitude of the signal received. The amplitude is proportional to the amount of energy deposited in that part of the detector, so accurate energy measurements require high fidelity electronics. On top of this, the entire legacy system must be run alongside the new one so that the new system results can be validated against the old system. This further increases the amount of electronics that must be installed.

This thesis concerns itself with a new printed circuit board baseplane (in the front end electronics crates) through which all the signals from the Hadronic Endcap Calorimeter (a subset of the detector) are routed [3]. For this section of the detector, the new trigger system receives the same number of signals as the current trigger system. However, the signals must still be routed to both the new system and the old system and therefore need to be split in the new baseplane, doubling the number of signal lines in the baseplane. The second set of signal lines are sent to a new circuit board, the LAr Trigger Digitizer Board (LTDB), part of the new trigger system. For the old trigger system there are two Trigger Digitizer Boards (TDB) to receive signals from the baseplane, but for the new trigger system there is only one LTDB to receive the same number of signals. As such, higher density connectors must be used for the LTDB, adding more opportunities for crosstalk or other distortion.

In this work an electronic model is developed for a subset of interconnects of a prototype of Hadronic Endcap Calorimeter baseplane. The model characterizes the amount of reflection, transmission and crosstalk as a function of frequency and is accurate up to 100 MHz, above which the frequency components of the signals sent through the baseplane are negligible.

Many of the techniques used to model and measure the prototype HEC baseplane were developed and tested on a simple printed circuit board referred to as the "test board." A model of this test board will be shown before the model for the prototype HEC baseplane.

The remainder of this thesis is structured as follows:

Chapter 2 provides background on the LHC, the ATLAS detector and the Phase-1 Calorimeter upgrade. Details of the prototype HEC baseplane are given in this chapter.

Chapter 3 is a short review of transmission line theory (including the skin effect, dielectric loss and crosstalk), S-parameters and time domain reflectometry. Several examples are given of S-parameters and time domain reflectometry traces of different devices to make understanding future figures easier.

Chapter 4 examines using time domain reflectometry and Tektronix' IConnect software to extract the S-parameters of printed circuit boards. A method is developed for measuring the prototype HEC baseplane and other printed circuit boards. This method requires measurement be made of the both the printed circuit board and the patch cables (part of the measurement system used to connect the printed circuit board to the time domain reflectometer) combined, forcing models to include the patch in order to be compared to measurements. This chapter also introduces the test board.

Chapter 5 introduces the software used to model the test board and prototype HEC baseplane: Keysight Technologies' Electromagnetic Professional (EMPro) and Advanced Design System (ADS). The former is used to simulate stripline transmission lines used the Finite Element Method (FEM) of 3D electromagnetic simulation. The latter is used to model the patch cables and connectors, calculate time domain reflectometer traces and calculate S-parameters.

Chapter 6 develops a model of the test board and compares measured S-parameters with the S-parameters of the model.

Chapter 7 develops a model for pairs of interconnects of the prototype HEC baseplane. The S-parameters of the model are compared to measured S-parameters for two pairs of interconnects of the baseplane.

Chapter 8 summarizes the findings and presents the S-parameters of the model of one of the pairs of interconnects on the prototype HEC baseplane without the patch cables in the model.

Chapter 2

The ATLAS Detector and the Phase-1 Liquid Argon Upgrade

This chapter provides background on the Large Hadron Collider (LHC) [6], the ATLAS detector [4] and the Phase-1 Calorimeter Upgrade [5, 3]. The detector components are discussed briefly to provide an overview of the systems comprising the detector. The triggering system, however, is discussed in more depth to provide an understanding of the current trigger and the current front end electronics for the Hadronic Endcap Calorimeter. The Phase-1 Upgrade is then discussed, giving motivation for the upgrade, the requirements and the implementation of the upgrade. The upgrades required for the HEC front end electronics are discussed and details about the prototype HEC baseplane are given.

2.1 The Large Hadron Collider

The Large Hadron Collider (LHC) is a synchrotron accelerator located at CERN near Geneva, Switzerland. The accelerator produces both the highest energy and highest instantaneous luminosity proton beams in the world. The LHC allows for more precise measurements of the Standard Model and the possibility of seeing new physics beyond the Standard Model. In 2012 two of the detectors at the LHC (ATLAS and CMS) discovered a new particle consistent with the Higgs boson [1, 7].

The LHC was designed to accelerate counter rotating bunches of protons or lead ions, colliding bunches together every 25 ns (currently every 50 ns) at interaction points. The initial proton collisions were conducted at a centre of mass energy of 7

TeV and instantaneous luminosity of $L \approx 10^{30}\ cm^{-2}s^{-1}$. During subsequent runs, the energy and luminosity of the beam has been increased. In the current run (2015 to 2017) the LHC will reach its nominal designed energy of 14 TeV centre of mass energy and instantaneous luminosity of $L = 10^{34}\ cm^{-2}s^{-1}$. Starting in 2019 the instantaneous luminosity will be pushed beyond the nominal value, expected to reach $L = 2 \times 10^{34}\ cm^{-2}s^{-1}$ [3, p. 3].

There are four locations where the beams cross (interaction points) and collisions occur. At each of these locations there is a large detector experiment as depicted in figure 2.1. The ATLAS (A Toroidal LHC ApparatuS) [4] and CMS (Compact Muon Solenoid) [8] detectors are two multipurpose detectors; LHCb [9] is a specialized detector for studying bottom quark physics; and the ALICE (A Large Ion Collider Experiment) detector [10] is designed for studying heavy ion collisions. In addition to these detectors there are 3 other current and planned detectors–TOTEM [11], LHCf [12] and MoEDAL [13]– two of which share interaction points with other detectors and one which is not located at an interaction point.

2.2 The ATLAS Detector

The ATLAS detector is a general purpose detector designed to be flexible enough to make measurements that will test many different types of theories. It tracks particles, measures the momentum of charged particles by observing their deflection in magnetic fields and measures the energy of most Standard Model particles that are created (neutrinos pass through). Excellent energy measurements make it a good tool in the search for non-Standard Model particles that could pass through the detector and result in missing transverse energy[1].

In order to detect and measure the various types of particles, many different detector subsystems are used. These subsystems are layered (much like an onion), with each system optimized for certain particles. Most detector subsystems have a barrel (layers of concentric cylindrical shells with no ends) to cover particles with low pseudorapidity[2] and endcap (consisting of layers of disk-shaped detectors at the ends of the barrels) regions to cover particles with higher pseudorapidity. The variety of

[1]Missing transverse energy is calculated using the energy and position of calorimeter cells to create vectors that can be added together to determine if there is an imbalance in the energy flow in the plane transvers to the proton beams [14]

[2]Pseudorapidity is a spatial coordinate used to describe an angle, θ, relative to the beam axis. It is related to θ by: $\eta = -\ln\left[\tan\left(\frac{\theta}{2}\right)\right]$.

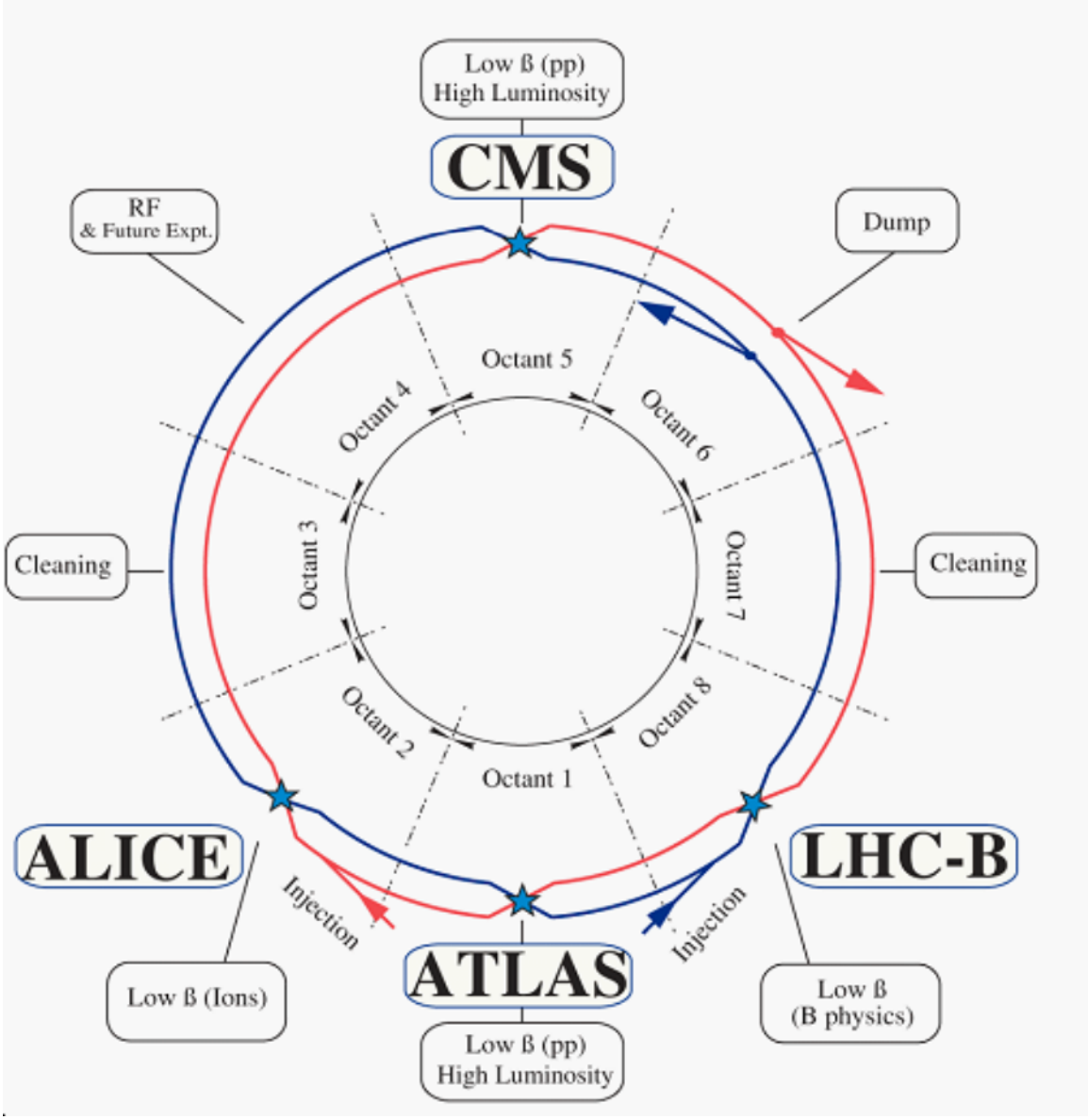

Figure 2.1: A schematic of the LHC showing both beams, their interaction points and the detectors at the interaction points [6, p. 8].

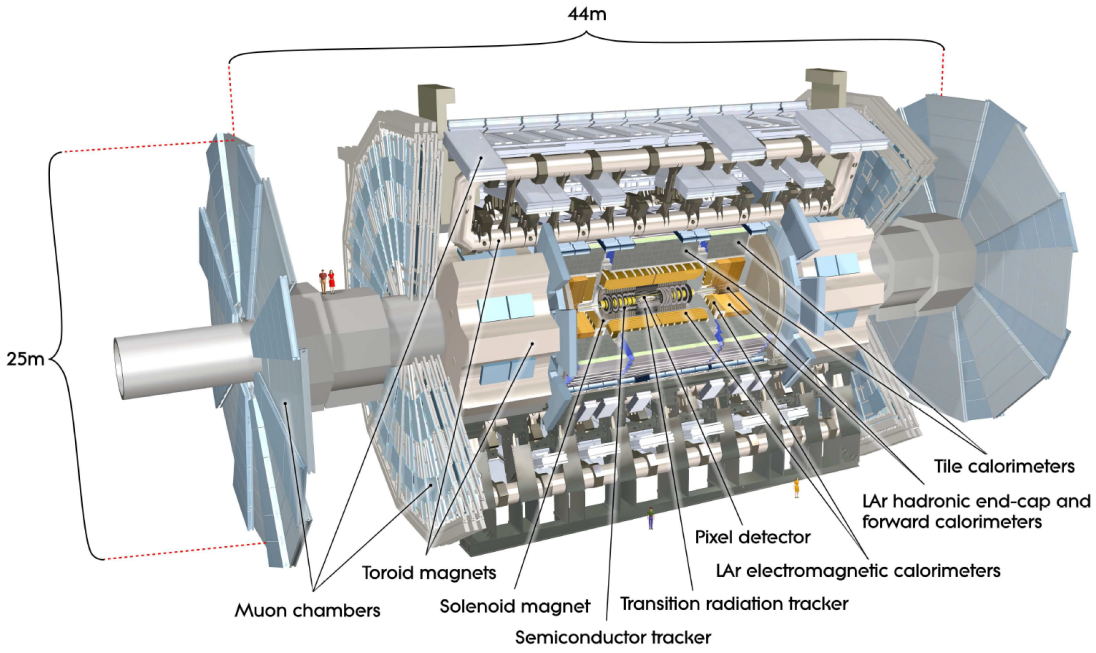

Figure 2.2: A schematic of the ATLAS detector [4, p. 4].

detectors and their size requirements create a 44m long by 25m in diameter device. The following will briefly discuss the major detector components starting from the middle of the detector, closest to the interaction point (see figure 2.2). The coordinate system used in this thesis is pseudorapidity (defined above), η; the angle (azimuthal) from the vertical, ϕ; and the distance from the interaction point. The latter is not used directly, but moving farther from the interaction point moves through 'layers' of the detector.

The Inner Detector

The Inner Detector [4, p. 53–109] is the subsystem closest to the interaction point. It is 6.2 m long, 2.1 m in diameter and covers pseudorapidity, $|\eta| < 2.5$. The Inner Detector has three subsystems: the Pixel Detector, Silicon Microstrip Detector and the Transition Radiation Tracker (see figure 2.3). This detector reconstructs the trajectory of charged particles leaving the interaction point, and those created from secondary decays. The density of pixels and strip detectors allow for high accuracy position measurements. The Inner Detector is surrounded by a solenoid, immersing the entire detector in a 2 T magnetic field (parallel to the beam pipe), allowing for momentum measurements of charged particles by observing their deflection.

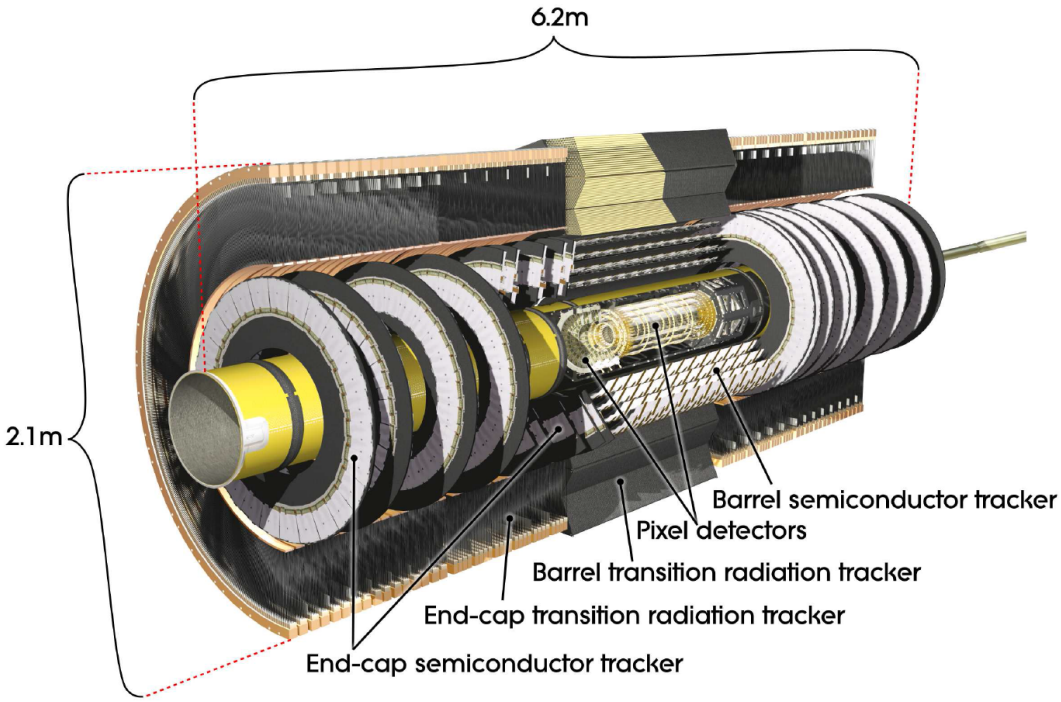

Figure 2.3: A schematic of the Inner Detector [4, p. 6].

Calorimetry

Most of the particles generated by the proton-proton collisions are absorbed in the calorimeter [4, p. 110–163], where the deposited energy is measured. Pseudorapidity coverage up to $|\eta| < 4.9$ results in few particles escaping close to the beam pipe, and the overall thickness (11 interaction lengths at $\eta = 0$) prevents most Standard Model particles from passing through the calorimeter (neutrinos and muons do). This makes the calorimeter excellent for missing energy measurements. The thickness of the calorimeter also blocks electromagnetic and hadronic showers from entering the muon spectrometer.

The calorimeter system is comprised of several sampling calorimeters (see figure 2.4): the Liquid Argon (LAr) Electromagnetic Barrel [15] and Endcap [16] calorimeters for electromagnetic calorimetry (EM calorimeters); the Tile Barrel Calorimeter[17], LAr Hadronic Endcap Calorimeter (HEC) [18] and the LAr Forward Calorimeter for hadronic calorimetry [19]. The fine granularity of the Electromagnetic calorimeters is suited to accurate measurements of electrons and photons; the rest of the calorimeter is less granular and sufficient for jet reconstruction. The Tile Barrel and Extended Barrels consist of steel absorbers with scintillators and the LAr calorimeters [20] consist of layers of absorbers (lead, copper or tungsten depending on the component) with liquid argon gaps. The various components overlap in pseudorapidity at the edges and an accordion type shape is used in the electromagnetic calorimeter to prevent any azimuthal cracks. All of the LAr calorimeters are in cryostats with one cryostat for the barrel and two cryostats on each end for the endcaps.

The Hadronic Endcap Calorimeter (HEC) is the focus of this thesis and deserves further description [4, p. 126–127]. The HEC consists of two wheels (two in each endcap) of 32 wedge shaped modules covering the range $1.5 < |\eta| < 3.2$. Each wheel has two signal layers resulting in 4 layers per endcap. The detector cells (elementary cells) are segmented such that $\Delta\eta \times \Delta\phi = 0.1 \times 0.1$ for $|\eta| < 2.5$ and $\Delta\eta \times \Delta\phi = 0.2 \times 0.2$ for larger η, resulting in 5632 total read-out channels. This detector is less granular compared to the Electromagnetic calorimeter with far fewer read-out channels.

Muon Spectrometer

A system of detectors for muons is situated in toroidal magnetic fields which surround the calorimeter [4, p. 164–205]. The signals from the muon system are not used in

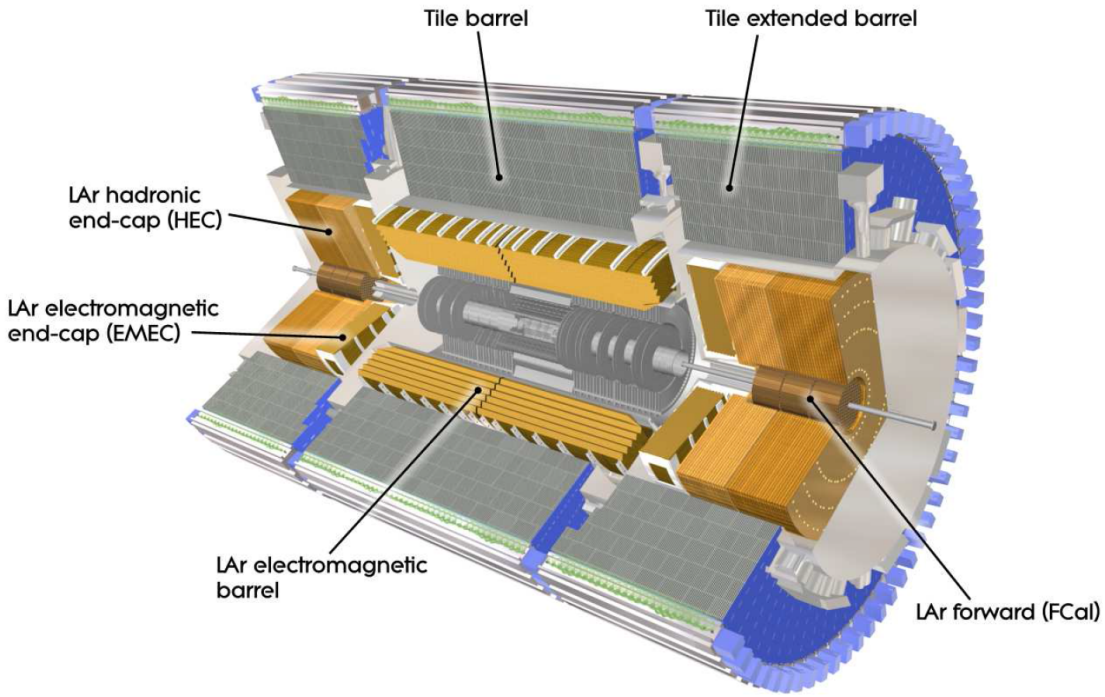

Figure 2.4: A schematic of the calorimetry system [4, p. 8].

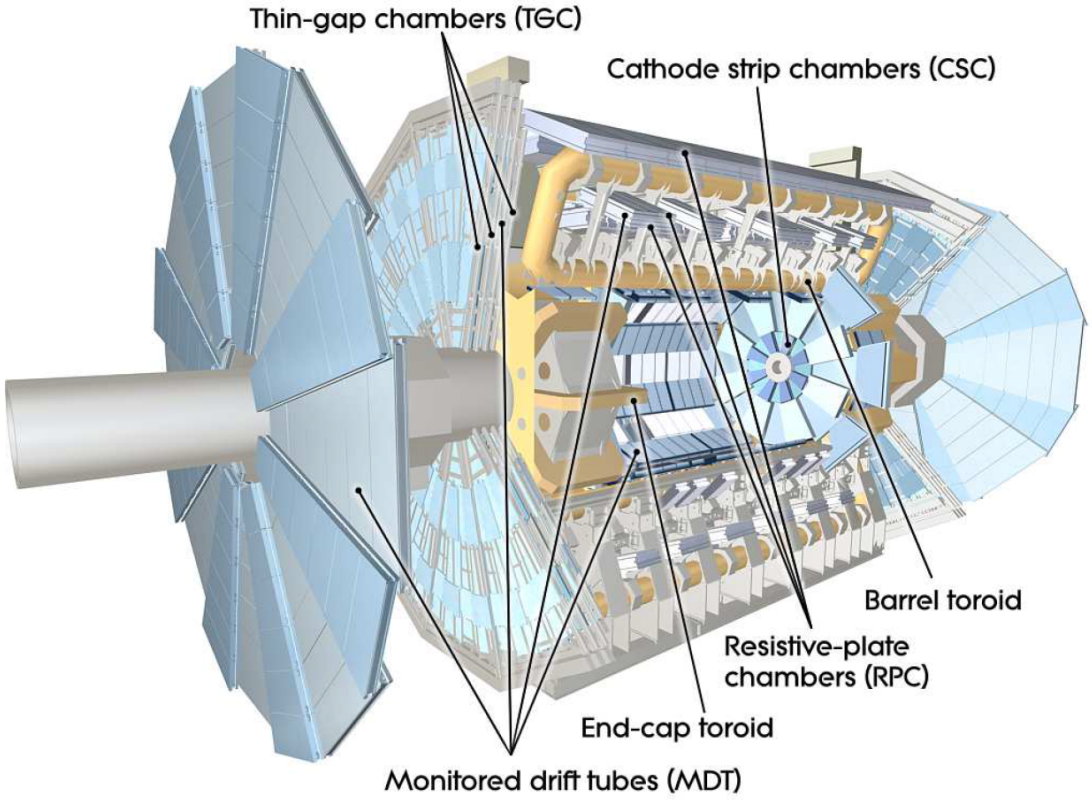

Figure 2.5: A schematic of the Muon Spectrometer [4, p. 11].

this thesis.

2.3 ATLAS Trigger System

In a given bunch crossing, the probability of processes occurring that are interesting is small compared to the total interaction cross section. In order to get sufficient (for statistically significant results) numbers of interesting events in a reasonable period of time, bunch crossings must happen at a very high rate (25 ns between crossings = 40 MHz for LHC). Recording all of these events would be impossible. To reduce the number of events to a sufficiently small rate for data recording, a trigger system [4, p. 218–256] is used that analyzes the collision data and decides what is and is not worth recording.

The ATLAS detector employs a three level trigger system wherein each level of the system analyzes the events (bunch crossings) accepted by the last trigger and decides whether to accept it, decreasing the acceptance rate at each level. Each level of the

trigger performs a more in-depth analysis than the previous, but has more time to analyze the signal. The trigger system consists of the level 1 trigger [4, p. 220–241], the level 2 trigger and the event filter [4, p. 242–251]. The level 1 trigger is often referred to as the low level trigger and must make decisions very quickly in order to keep up with the bunch crossing rate. As such, the level 1 trigger is implemented on custom made electronics. The level 2 trigger and event filter are referred to as the high level trigger and run on commercial computer and network hardware.

The level 1 trigger looks for high transverse momentum (p_T) muons, electrons/photons, jets and tau leptons decaying into hadrons. It also looks for events with large amounts of missing transverse energy and large total transverse energy[3]. The level 1 trigger has a maximum latency of 2.5 μs (including time for signal to be transmitted out of and back into the front end electronics crates) and a maximum acceptance rate of 100 kHz (75 kHz during run 1). Due to the short time required for decisions and the necessary compactness of the electronics, the level 1 trigger uses a subset of the calorimeter data with cells summed together in η, ϕ and depth (layers).

The level 2 trigger looks at regions of interest that the level 1 trigger has identified. Using the full granularity of the detector in these regions, it analyzes the event and reduces the trigger rate to 3.5 kHz in an average processing time of 40ms. It passes accepted events to the Event Filter, which uses an analysis similar to the offline analysis to reconstruct events and make final decisions as to what is recorded. The Event Filter reduces the acceptance rate to 400 Hz (Run 1) using multiple processors with each event taking an average processing time of 4 seconds.

2.3.1 Level 1 Calorimeter Trigger

Signals from the LAr calorimeters initially enter electronics crates that are located on the detector and known as Front End Electronics Crates (FEC). In these crates, the signals are amplified, shaped and stored on analogue switched-capacitor arrays, on which signals from many different bunch crossings may be stored simultaneously. The signals are split and summed together (using analog summation) in blocks of depth (layers), η and ϕ, known as trigger towers, that are sent off the detector to the Calorimeter Trigger. The region that is summed differs depending on the component of the calorimeter and with η, but for most components they are summed completely

[3]Total transverse energy is the scalar sum of the energy in the plane transverse to the proton beam of all calorimeter elements, called cells, that are associated with an object [14]

Section	Layer (Depth)	Elementary cell $\Delta\eta \times \Delta\phi$	Trigger Tower $\Delta\eta \times \Delta\phi$
EM Barrel	Presampler	0.025×0.1	0.1×0.1
$0 < \eta < 1.4$	Front	0.003125×0.1	
	Middle	0.025×0.025	
	Back	0.05×0.025	
EM Barrel	Presampler	0.025×0.1	0.1×0.1
$1.4 < \eta < 1.5$	Front	0.025×0.025	
	Middle	0.075×0.025	
HEC	1	0.1×0.1	0.1×0.1
$1.5 < \eta < 2.5$	2	0.1×0.1	
	3	0.1×0.1	
	4	0.1×0.1	
HEC	1	0.2×0.2	0.2×0.2
$2.5 < \eta < 3.2$	2	0.2×0.2	
	3	0.2×0.2	
	4	0.2×0.2	

Table 2.1: Trigger Towers versus elementary cells for sections of the Electromagnetic Barrel Calorimeter and Hadronic Endcap [3]

in depth and into blocks of $\Delta\eta \times \Delta\phi = 0.1 \times 0.1$ (the sections of the HEC where elementary cells are larger than this are an exception). Table 2.1 shows the summation region for the Electromagnetic Barrel and Hadronic Endcap.

The Calorimeter Trigger identifies certain types of objects and conditions. For example, the Calorimeter Trigger identifies whether a transverse p_T is past a certain threshold or how many jets were present in the event. This information, as well as anything identified by the Muon Trigger, is passed (as Boolean flags) to the Central Trigger Processor (see figure 2.6) that compares the characteristics of the event to a programmed list of criteria known as trigger items. Each trigger item is a set of criteria (e.g. two leptons are present and p_T is above a threshold), where, if met, the event can be accepted. The trigger items can also be weighted so that there could be a random component as to whether they are satisfied.

If a trigger is satisfied then a signal is sent to the front end crates to digitize the signals stored for that bunch crossing (from all the detector components) and send them to the Read Out Crates. At the same time, Region of Interest information is determined by the level 1 trigger and sent to the level 2 trigger for that bunch crossing. If the bunch crossing does not meet any trigger conditions then the data

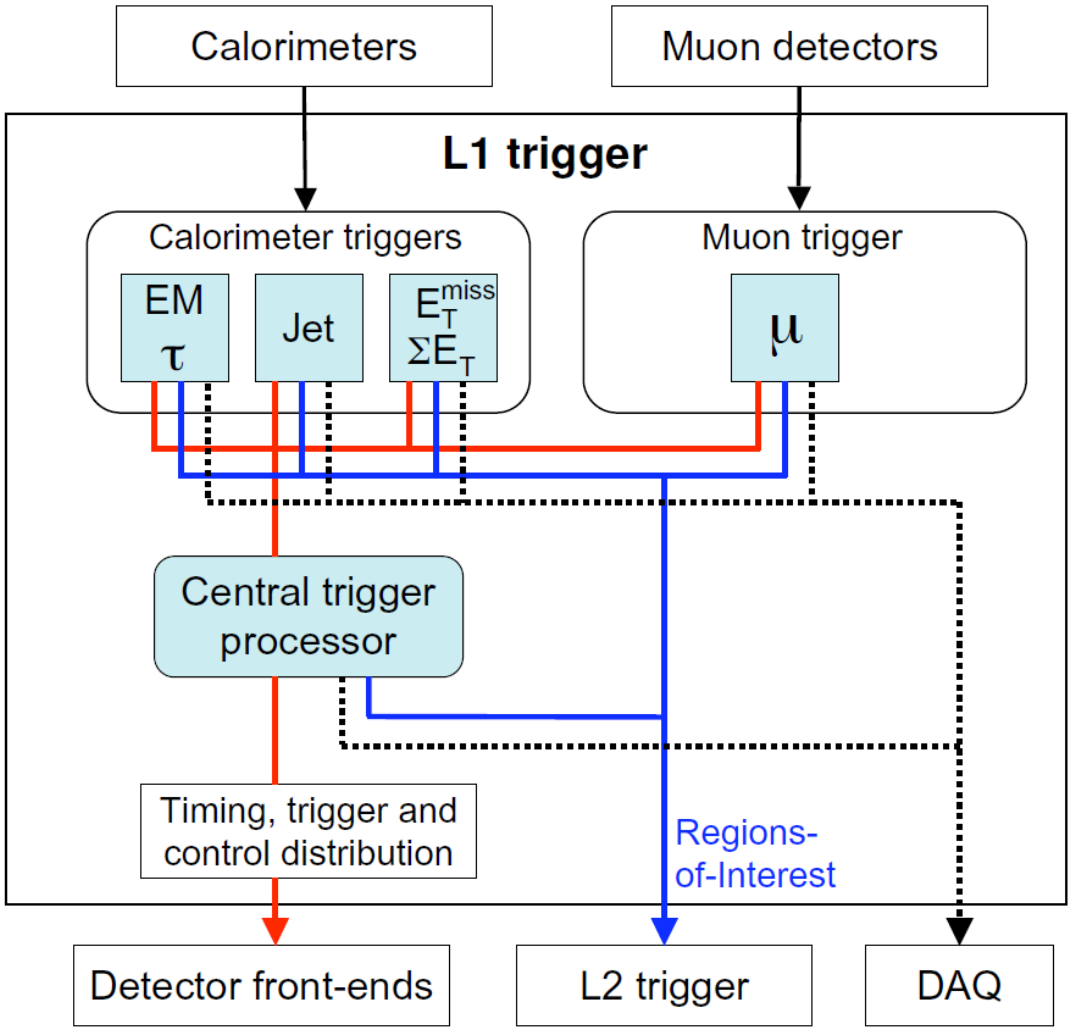

Figure 2.6: A diagram of the level 1 trigger [4].

for the bunch crossing is erased.

2.3.2 The Hadronic Endcap Calorimeter Front End Electronics Crates

Charged Particles traversing the liquid argon gaps create triangular current pulses with amplitude proportional to the amount of energy deposited. In the Hadronic Endcaps, the signals are amplified on the detector and transferred out of the cryostat to the Front End Crates [21]. The HEC front end crates are located on the detector (see figure 2.7).

There are 8 Front End Crates with HEC electronics. These crates are shared with some of the Electromagnetic Endcap Calorimeter front end electronics. In the HEC portion of these crates there are 6 Front End Boards (FEBs) [22] and 2 Tower-Driver Boards (TDBs) which will be discussed below. There is also a Controller Board, a Calibration Board [23], a Monitoring Board and an extra space. All of these are plugged into a baseplane that routes signals between them and provides power. Figure 2.8 provides a diagram of the components of a front and crate and figure 2.9 a circuit diagram for a EM Calorimeter front end crate. This differs from the electronics of the Hadronic Endcap front end crates by the addition of an amplifier on the Front End Board and the replacement of the Tower-Driver Board by a Tower-Builder Board, the latter of which has summation while the former does not.

The amplified calorimeter pulses first enter (through the baseplane) a Front End Board (FEB). There the pulses are shaped and then split and sent to two places. The signals are sent through either 1, 10 or 100 times amplification (decided on board which to use) and then stored on Switched-Capacitor Arrays (SCA). The SCA stores the signals until an acceptance signal is received from the level 1 trigger, in which case they are digitised and transmitted off detector on optical links to the Read Out Crates (ROC), or a rejection signal is received and the section of the SCA storing that bunch crossing is wiped. The signals are also sent to the Layer Sum Board, a daughter board on the Front-end board which uses analogue summation to sum the 4 layers on the Hadronic Endcap Calorimeter. The summed signals from the 6 FEB's are routed back through the baseplane to the 2 Tower-Driver Boards (TDBs), where the signals are sent on twisted pairs to the level 1 trigger.

Bipolar $CR-(RC)^2$ (TimeConstant $= RC = 15\ ns$) shaping is applied in the FEB to the triangular current pulses produced by the calorimeter to optimise the

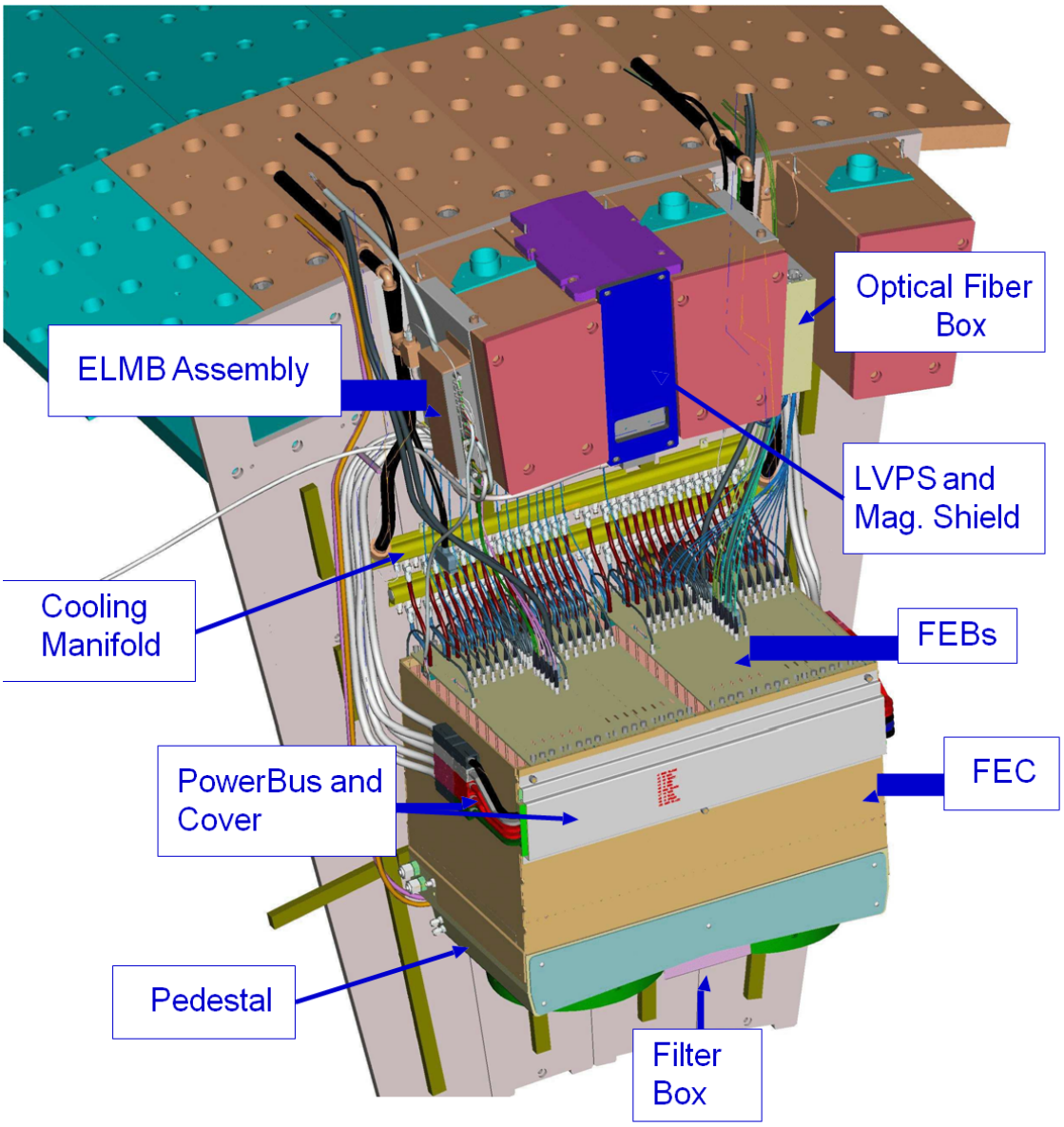

Figure 2.7: A diagram showing a LAr front end crate and surrounding components.

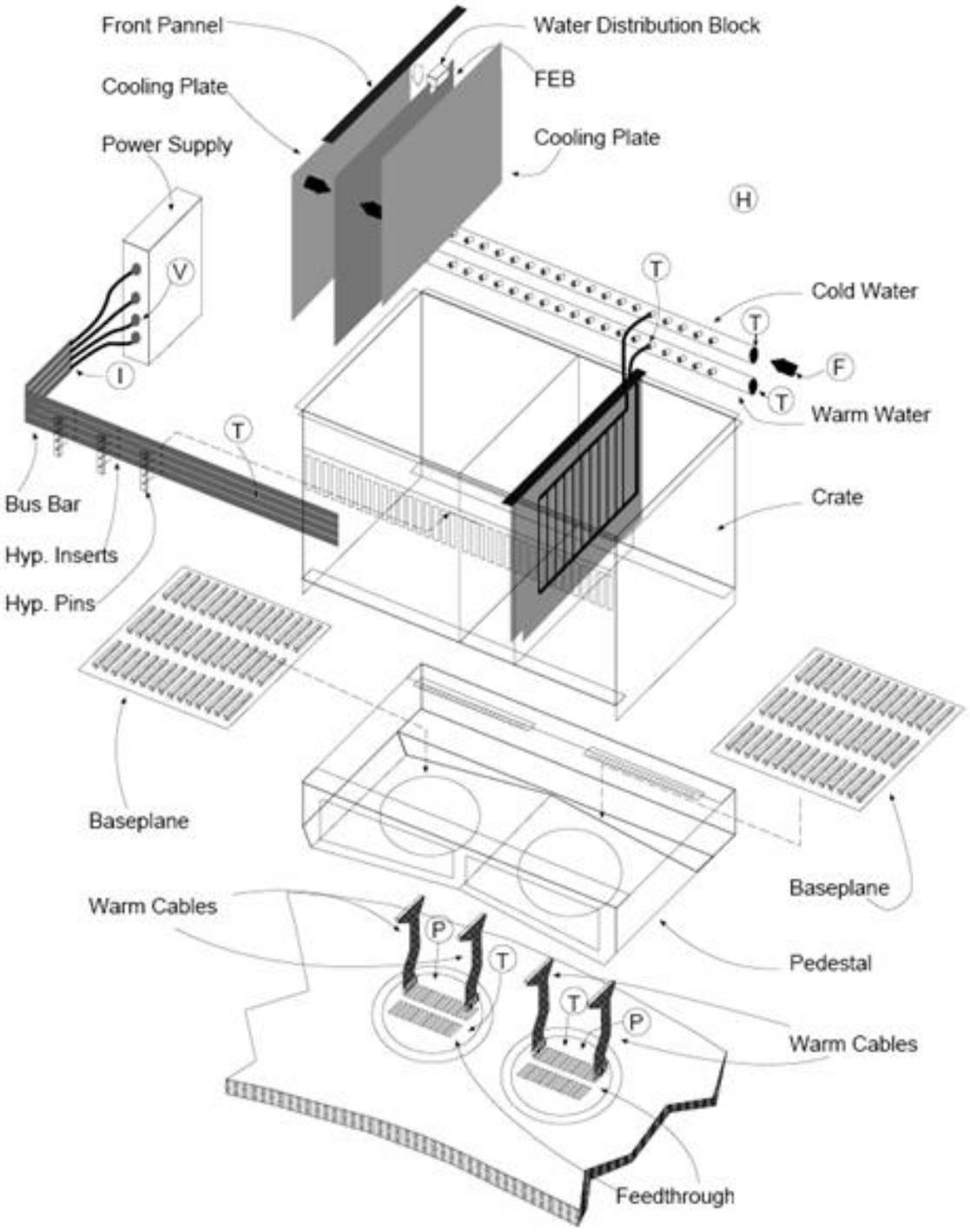

Figure 2.8: A drawing showing the components of the FEC.

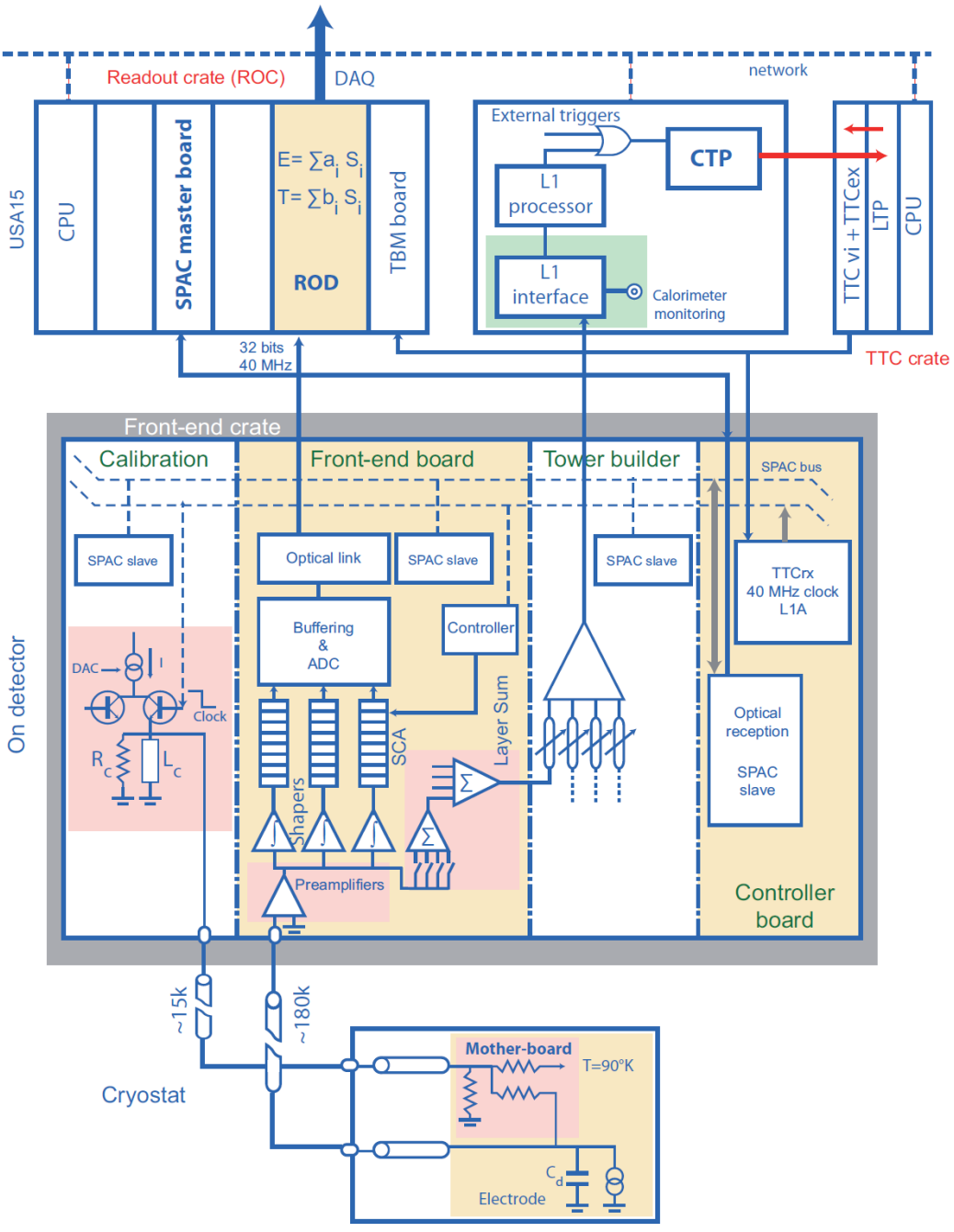

Figure 2.9: A diagram of the LAr readout electronics [4].

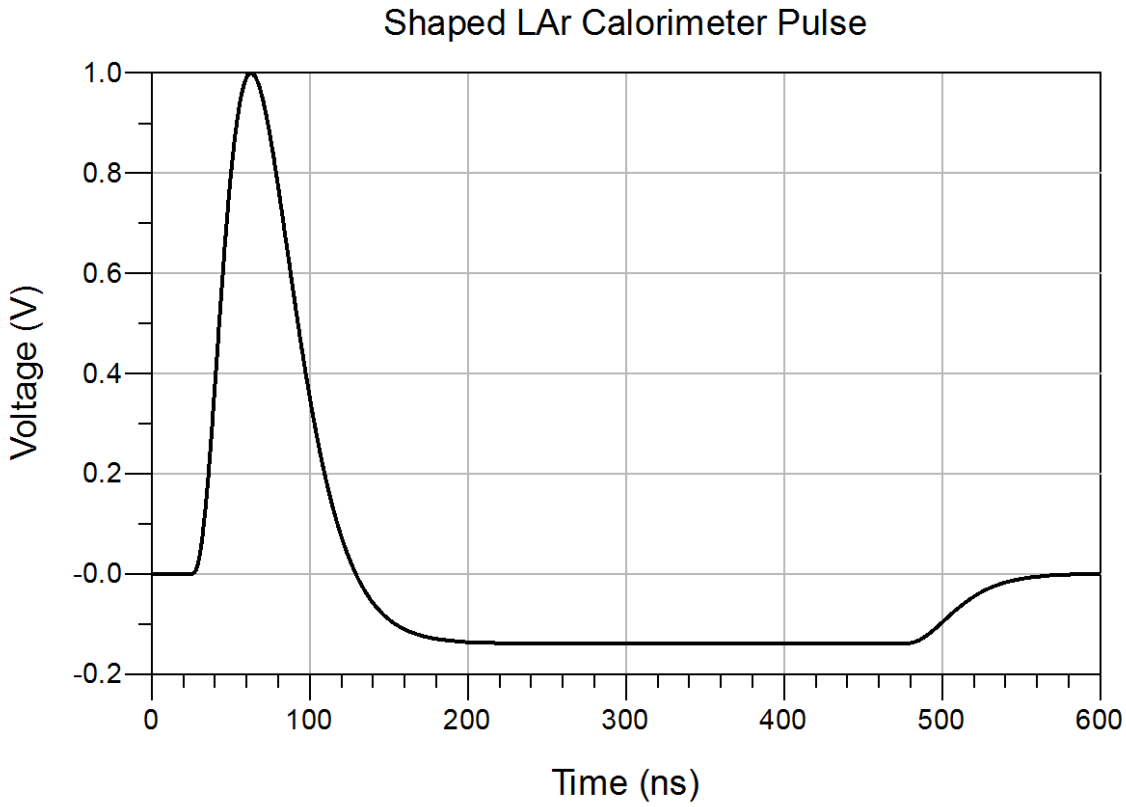

Figure 2.10: A typical shaped LAr calorimeter pulse with peak voltage scaled to 1 V.

signal to noise ratio and make the pulse peak earlier. This is the shape of the pulse (shown in figure 2.10) sent through the baseplane. The frequency components of a typical pulse are shown in figure 2.11. The amplitude of the frequency components peaks around 1.45 MHz. At 50 MHz the amplitude has dropped to 0.3% and at 100 MHz to 0.02% of the peak value.

2.4 Phase-1 Calorimeter Upgrade

Heading into run 3 (2019 to 2021), the luminosity of the LHC will go beyond the nominal design value. As discussed in the introduction, this will increase the number of interactions per bunch crossing which will make the level 1 Calorimeter Trigger less able to select the events of interest [5, 3]. Monte Carlo simulations have found that the rate of electrons at the current transverse energy (E_T) threshold (23 GeV) would take up most of the maximum trigger rate available (80 kHz of a maximum 100

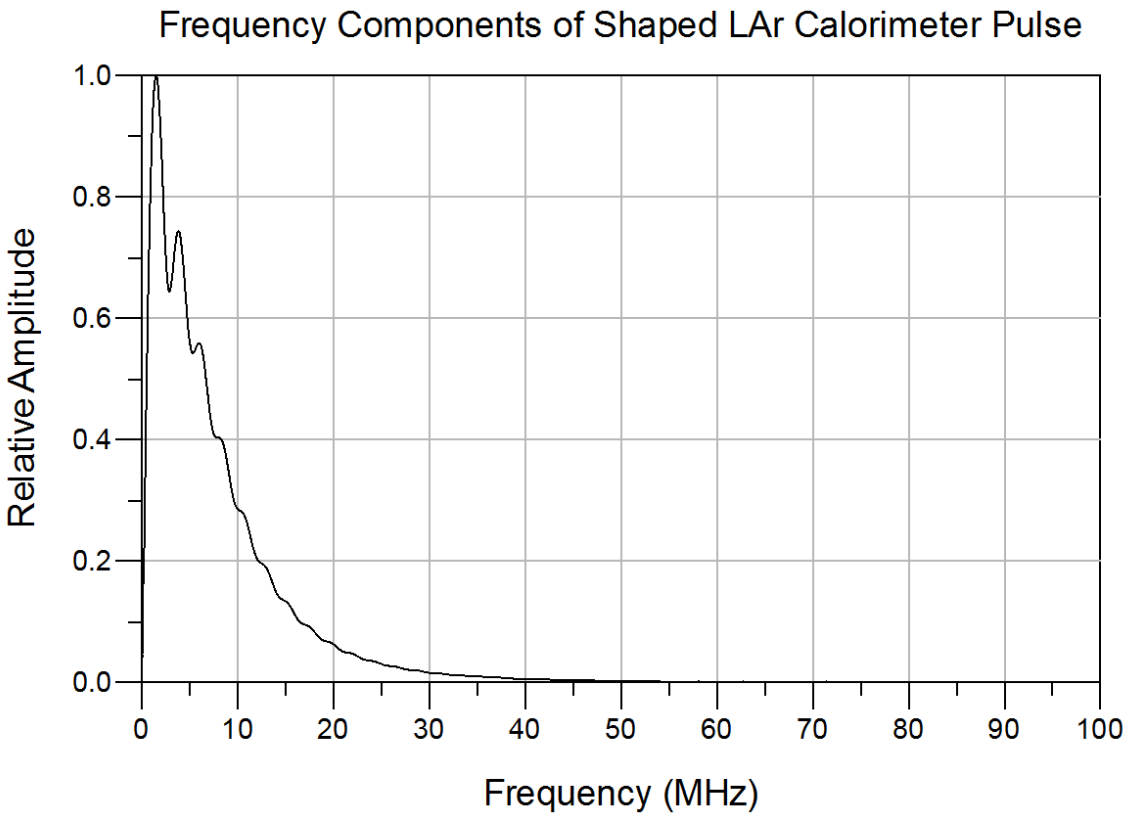

Figure 2.11: The frequency components of a LAr calorimeter pulse. The values have been scaled so that the amplitude of the largest peak is 1.

kHz). Increasing the transverse energy (E_T) threshold for electrons could lower this to the desired maximum rate for single electrons of 20 kHz, but this would require a threshold of 40 to 45 GeV (full efficiency around 50 to 55 GeV) which would cut much of signals from W and Z bosons, some important Higgs boson decay paths, signals from multiple theoretically predicted supersymmetric particles and other phenomena. Requiring electrons be isolated from other events can decrease this trigger rate, but not enough to avoid large increases in the E_T threshold.

Many of the signals that the level 1 trigger interprets as electrons events are not. Low p_T jets dominate the level 1 electron trigger rate at low E_T. In the level 2 trigger, shower shape algorithms are deployed to discriminate jets from electrons. These algorithms examine the distribution of energy around the cell in which the most energy was deposited in the shower. The ratio of energy in the second (middle) layer deposited in a 3×3 and a 7×7 cluster of calorimeter cells in η and *phi* around the cell in which the most energy was deposited is calculated. Events with a ratio above a certain value are kept while those below are excluded. Electrons deposit their energy in a smaller space than jets, so this removes more jets than electrons. This algorithm is efficient, but requires more calorimeter segmentation than is available to the level 1 trigger.

Studies have shown [5] that if a similar algorithm is implemented using "Supercells" (coarser than elementary cells in the EM calorimeter, but finer than trigger towers) in the second layer of the EM calorimeter then similar results can be achieved. The ratio $R_\eta = \frac{E_{3\times2}}{E_{7\times2}}$ is calculated, where $E_{3\times2}$ and $E_{7\times2}$ are the energy deposited in a 3×2 and a 7×2 (in η and ϕ) cluster of Supercells around the Supercell in which the most energy was deposited. Again, as seen in figure 2.12, electrons deposit their energy in a smaller space than jets. Monte-Carlo simulations and enhanced bias data[4] (from the 2011 run) analyzed accepting only events with $R_\eta > 0.94$ maintained a true electron efficiency above 99.3% (calculated using $Z \rightarrow e^+e^-$) with jet rejection efficiencies of 56.7% and 51.2% respectively (for the Monte-Carlo and enhanced bias data).

The inclusion of layer information from the Hadronic calorimeters has no impact on jet and electron discrimination in the level 1 trigger. However, increased energy resolution in the hadronic trigger towers can further improve jet rejection. Rejecting events Hadronic core energy, E_{core}^{had} (the energy deposited in the 2×2 region of trigger

[4]Data taken with a low level 1 trigger thresholds and no high level trigger selection. This data can be used to approximate some of the effects of higher luminosity on the level 1 trigger.

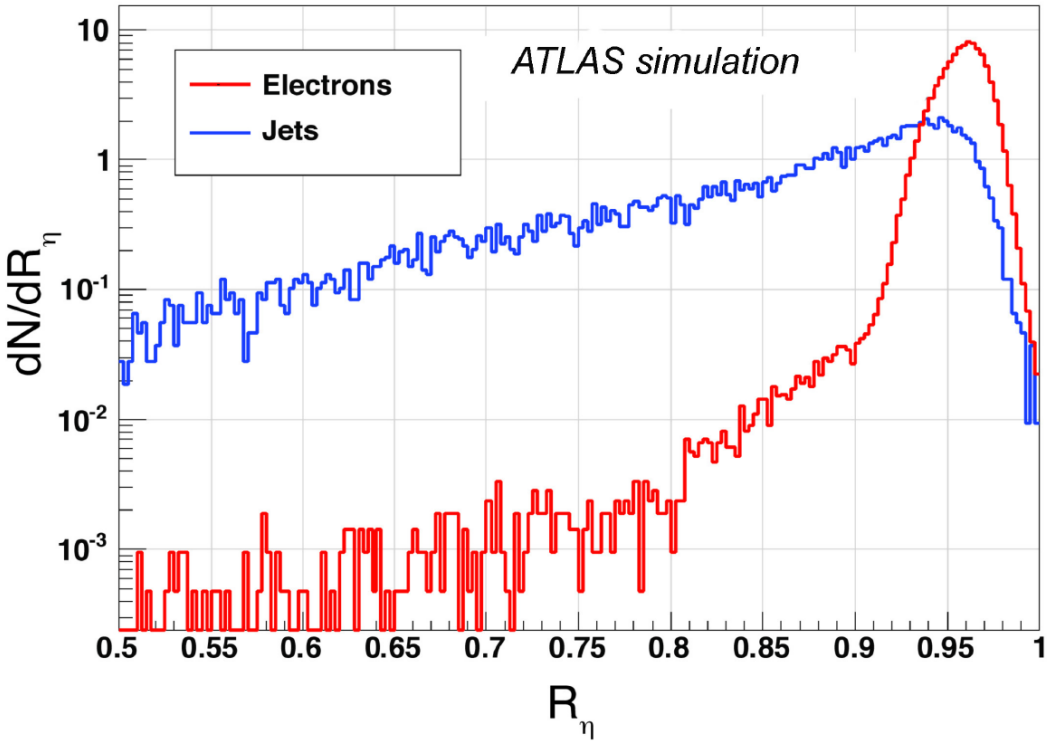

Figure 2.12: Distribution of electrons and jets versus R_η [5].

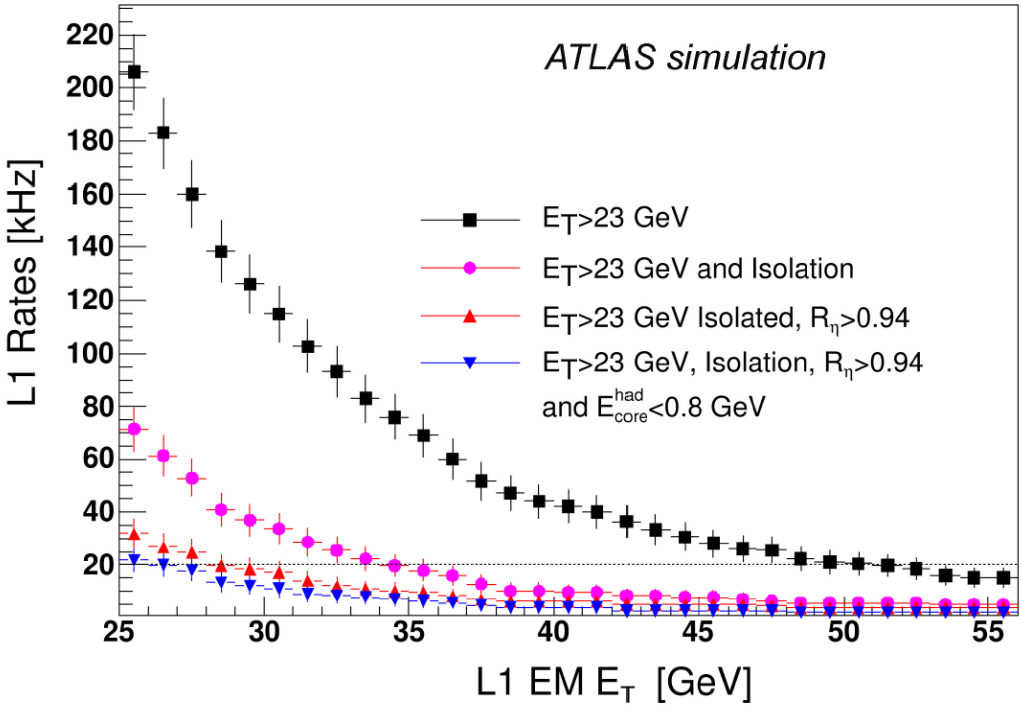

Figure 2.13: Expected level 1 trigger rates for electrons from Monte Carlo simulations with various cuts applied [5].

towers in the Hadronic calorimeter behind an EM calorimeter cluster), $\geq$ 800 MeV, with a least significant bit of 250 MeV, improved jet rejection. In the current system energy resolution is limited to 1 GeV in the trigger towers making this impossible.

Figure 2.13 shows the trigger rates for various selection criteria. When R_η and E^{had}_{core} requirements are applied, the E_T threshold required for a 20 kHz acceptance rate is lowered to just above 25 GeV. With this threshold, the ATLAS detector can maintain sensitivity to W, Z and other processes that would be lost with higher E_T thresholds. Beyond this, improved calorimeter segmentation and energy resolution will improve total transverse energy calculations and thus improve the sensitivity of the missing transverse energy trigger. The implementation of Supercells will allow the ATLAS detector to maintain the required trigger rates and improve trigger efficiency.

During the second long shutdown the Calorimeter Trigger and the Front End Electronics will be upgraded to implement supercells. This upgrade is referred to as the Phase-1 Liquid Argon upgrade [3]. These cells will have increased granularity and layer information in the EM calorimeter, but not in the hadronic calorimeters (see table 2.2 for EM barrel and HEC supercell sizes). The resolution of signal digitization

Section	Layer (Depth)	Elementary cell $\Delta\eta \times \Delta\phi$	Trigger Tower $\Delta\eta \times \Delta\phi$	Supercell $\Delta\eta \times \Delta\phi$
EM Barrel	Presampler	0.025×0.1	0.1×0.1	0.1×0.1
$0 < \eta < 1.4$	Front	0.003125×0.1		0.025×0.1
	Middle	0.025×0.025		0.025×0.1
	Back	0.05×0.025		0.1×0.1
HEC	1	0.1×0.1	0.1×0.1	0.1×0.1
$1.5 < \eta < 2.5$	2	0.1×0.1		
	3	0.1×0.1		
	4	0.1×0.1		
HEC	1	0.2×0.2	0.2×0.2	0.2×0.2
$2.5 < \eta < 3.2$	2	0.2×0.2		
	3	0.2×0.2		
	4	0.2×0.2		

Table 2.2: Supercells versus Trigger Towers versus elementary cells for part of the Electromagnetic Barrel Calorimeter and Hadronic Endcap Calorimeter [3]

for the level 1 trigger will be increased across the entire calorimeter. New calorimeter trigger processors will be installed to use the increased information and implement shower shape algorithms to improve trigger performance.

A schematic of the new electronics for EM calorimeter can be seen in figure 2.14. Designs for the hadronic systems are similar, but with summation implemented on the FEB rather than the LTDB. The trigger system requires new trigger processors and digital signal processing. LAr Trigger Digitizer Boards (LTDB) will be installed in the front end crates to digitize signals (from supercells) and send them to the new Calorimeter Trigger. The entire current trigger system will be preserved for validation purposes, so Tower Builder and Tower Driver Boards will remain in the front end crates. This requires signals be sent to both the LTDB and the TBB/TDB's. In the EM calorimeter fewer cells will be summed in η and no layer summation will be implemented. The new designs requires new Layer Sum Boards on the EM FEB's and a substantial increase in the number of interconnects in the EM front end crate baseplanes (11× increase). In the Hadronic system there is no reduced summation so the number of the number of interconnects in the baseplanes is doubled.

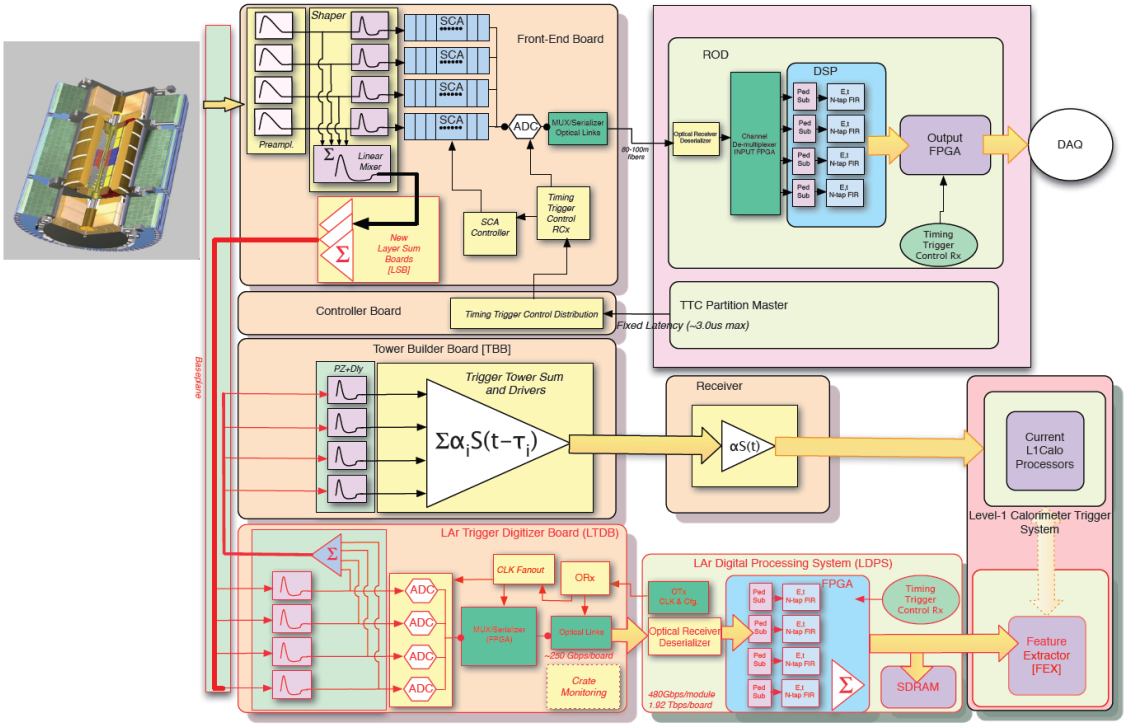

Figure 2.14: A diagram of the planned LAr Phase-1 readout electronics for the Electromagnetic Barrel calorimeter [3].

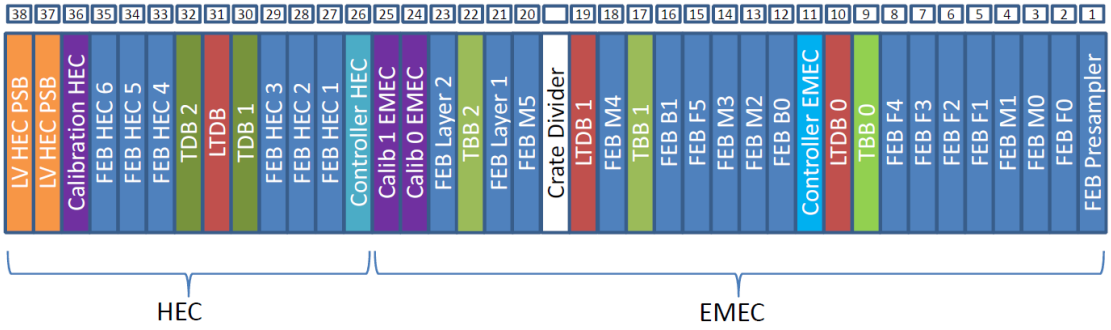

Figure 2.15: Slot assignment for the Front End Crates with HEC electronics [5, p. 71]. The crates are shared with EMEC electronics.

2.4.1 Prototype Hadronic Endcap Baseplane

The front end electronics for the Hadronic endcap calorimeter are being changed. On top of the addition of a new LTDB board in the HEC front end electronics, two slots (for circuit boards) in each crate are being given up to the Electromagnetic Endcap Calorimeter (EMEC) electronics (see figure 2.15 for slot assignment in Front End Crates with HEC electronics). This is being made up for by using a previously empty slot and dropping one controller board slot and one monitoring board slot. These changes require new baseplanes for the Hadronic Endcap front end electronics crates, which are being designed and tested at TRIUMF and the University of Victoria. Several designs have been made, and the 'worst case' design (the one where crosstalk and fidelity was expected to be the worst of the designs) was built for testing.

This prototype baseplane (shown in figure 2.16) is a multilayer printed circuit board with 5 signal layers. The interconnects for calorimeter signals–connecting the FEB to the TDB and LTDB–will transmit the signals in the board on stripline transmission lines with a nominal characteristic impedance of 50 Ω. Because the signals sent to the LTDB and TDB are identical, the interconnects split in the baseplane (either at the FEB or the TDB connector) and the signal is sent to both the TDB and the LTDB simultaneously. While the FEB and TDB have an impedance of 50 Ω, the LTDB has an impedance of 1 kΩ. A high impedance is needed for the LTDB because, with 50 Ω termination, the baseplane (after the split) would look like a 25 Ω transmission line, resulting in significant reflection back towards the FEB. The FEB's and TDB's will use the same press-fit connectors as the current baseplane (manufactured by FCI Electronics (formerly BERG electronics), part no. 50006). The LTDB uses high density press-fit connectors manufactured by ERNI Electronics (part no.

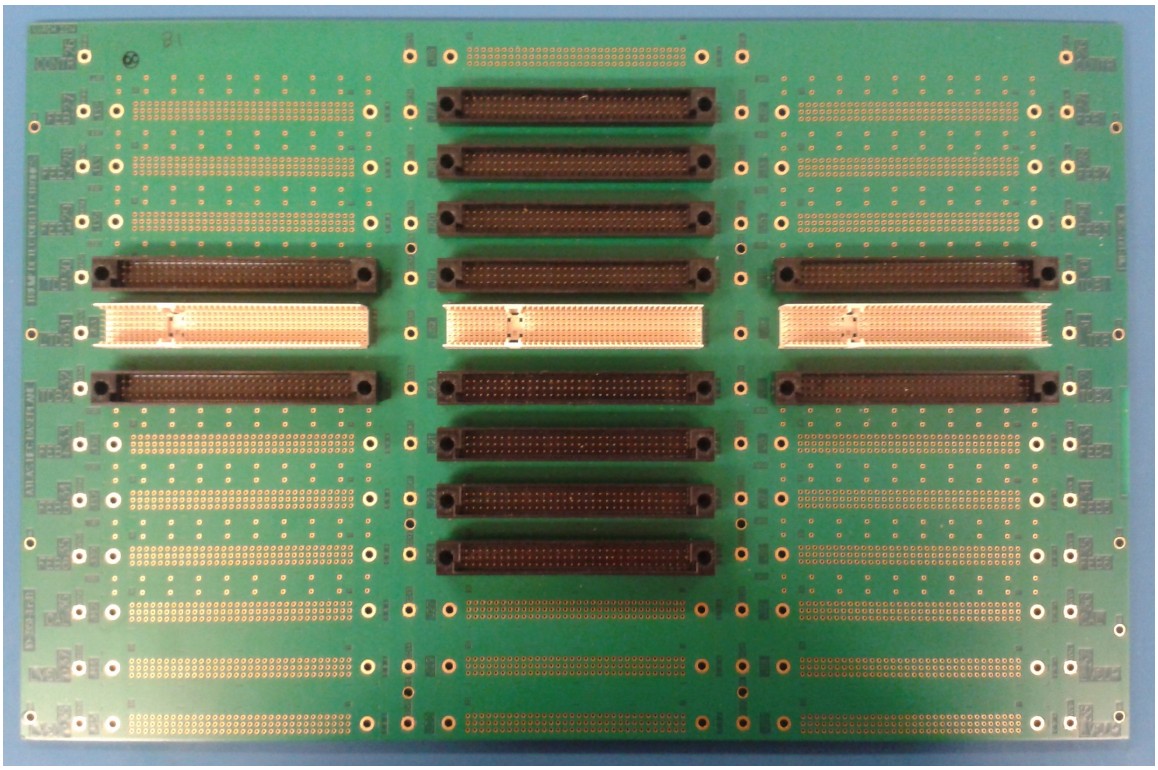

Figure 2.16: A picture of the prototype baseplane. The light coloured connectors are the ERNI connectors for the LTDB, the rows of three black connectors above and below the ERNI connectors are for the TDB's and the other 6 connectors are for the FEB's.

104735). We will refer to these as the FCI and ERNI connectors respectively.

The FCI connectors have 3 rows of 32 pins that are $1/10^{th}$ of an inch (2.54 mm) apart. For all FCI connectors on the prototype board the central row of pins are ground and the top and bottom rows alternate between signal and ground pins. The top and bottom rows alternate oppositely (signal, ground, signal, ground versus ground, signal, ground, signal) so that each column has only one signal pin (see figure 2.17).

The ERNI connectors has 7 rows of 47 pins that are 2 mm apart. The top, bottom and middle rows are ground. The top and bottom rows do not connect to individual pins in the female connector of the LTDB, they connect to ground shields on the LTDB. Signal pins are grouped into collections of 8 pins, 4 on each row with a one pin offset between rows (see figure 2.18 for a diagram). The 4 signal pins grouped on one row are usually routed together. Groups of pins are separated by at least one ground pin. Unlike the FCI connectors in which each has the same signal and ground

Figure 2.17: Signal and ground pin assignment on the FCI connector (used for FEB and TDB). Circles represent pins and x's indicate ground pins. The rows are labeled ABC and the columns 1 through 32.

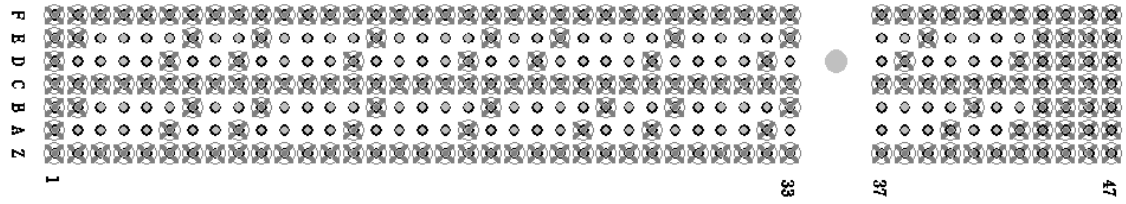

Figure 2.18: Signal and ground pin assignment for one of the ERNI connectors (used for LTDB). Circles represent pins and x's indicate ground pins. The central 5 rows are labeled ABCDE and the outer rows F and Z. The columns are labeled 1 through 47.

pin layout, each of the three ERNI connectors have a different arrangement.

Calorimeter signals sent through the baseplane see several differences from the existing system. The higher density of signals lines could increase the amount of crosstalk and contribute to distortion. This is especially true of the ERNI press-fit connectors due to the proximity of their signal pins and relative lack of shielding from neighbouring pins. The interconnects splitting in the board and the presence of an additional connector could cause more distortion to the signal. The prototype board also has more signal layers than the previous (5 versus 4 signal layers), while maintaining the same overall thickness. This requires thinner traces, increasing the effect of manufacturing tolerances.

Signal fidelity is important on the baseplanes because the amplitudes of the signals sent through the baseplane are used to determine the energy deposited in each supercell. Too much crosstalk or distortion of the signals could compromise the performance of the level 1 trigger. As such, the distortion and crosstalk must be well understood and minimized. In the existing analog electronics chain for the Level 1 trigger, the maximum permissible crosstalk was set at 1% [21]. The purpose of this thesis is to create an electronic model of the prototype baseplane. In this way the crosstalk and distortion of the baseplane can be characterized and understood. Because the frequency components of the LAr shaped calorimeter pulse are negligible at 100 MHz and above, this model does not need to extend beyond 100 MHz.

There are several features missing from the prototype board that will be included on the final board. Connectors and striplines have only been added for the TDB, LTDB and the output (into the board) of the FEB. Connectors and striplines for all other boards and signal inputs for the FEB (fed through the board) have not been included in the prototype. The addition of these should have a negligible effect on

the shaped calorimeter pulses because they carry different signals. The final board will also have shields and springs which interface with the daughter boards providing better ground connections. This could only decrease crosstalk and signal distortion from what is present in the prototype.

Chapter 3

Theory

This chapter outlines the basic theory needed to understand the simulations and analyses in later chapters. Transmission line theory is discussed. S-parameters and time domain reflectometry are introduced and some basic examples given and explained in order to make future figures easier to understand.

3.1 Transmission Line Theory

Transmission lines [24, 25, 26] are used to transmit electrical signals. They are usually comprised of a metal conductor and a dielectric (possibly air). If the conductor dimensions are small compared to the wavelengths involved, then the electric and magnetic fields can be assumed to be perpendicular to the direction of propagation (Transverse Electromagnetic Mode). Under these circumstances the transmission line can be described by the Telegrapher's equation:

$$\begin{aligned} \frac{\partial}{\partial x}V(x,t) &= -L\frac{\partial}{\partial t}i(x,t) - Ri(x,t) \\ \frac{\partial}{\partial x}i(x,t) &= -C\frac{\partial}{\partial t}V(x,t) - GV(x,t) \end{aligned} \tag{3.1}$$

Where x in the position along the transmission line, $V(x,t)$ is the voltage, $i(x,t)$ is the current and R, L, G and C are the resistance, inductance, conductance and capacitance per unit length. R, L, G and C are known as the RLGC parameters and can be understood by envisioning the transmission line as being made up on infinitesimal segments as depicted in figure 3.1.

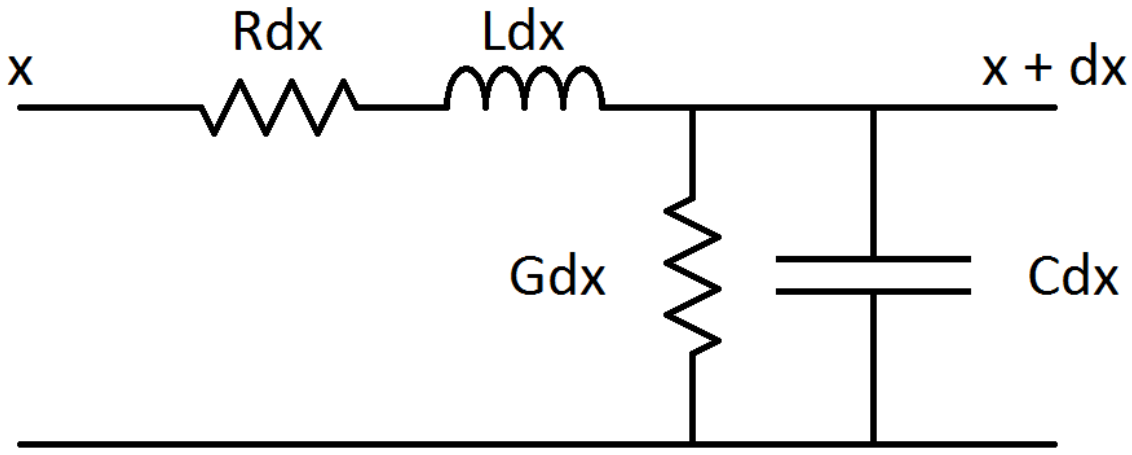

Figure 3.1: Infinitesimal segment of transmission line.

Traveling sine waves are a solution to the Telegrapher's equation. Transmission lines are linear, meaning that if a sine wave of angular frequency ω is input then the output is a sine wave of frequency ω. The characteristic impedance (ratio of voltage to current), Z_o, of the transmission line (for a sine wave) is given by:

$$Z_o = \sqrt{\frac{j\omega L + R}{j\omega C + G}} \tag{3.2}$$

Where j is the imaginary unit number. The velocity of a sine wave (phase velocity), v_p, is dependent on the speed of light, c, and the relative permittivity of the dielectric, ϵ_r:

$$v_p = \frac{c}{\sqrt{\epsilon_r}} \tag{3.3}$$

Changes in impedance cause partial reflection of the wave. The reflection coefficient, Γ, when the transmission line of characteristic impedance Z_o is terminated into an impedance of Z or another transmission line of characteristic impedance Z, is given by [24, 25]:

$$\Gamma = \frac{Z - Z_o}{Z + Z_o} \tag{3.4}$$

From this equation we can see that if the transmission line is terminated in with impedance equal to its own then there is no reflection and all of the wave is transmitted. If the terminating impedance is higher then there is some upright reflection and if it is lower then there is some inverted reflection.

The geometry of the transmission line, the permeability, μ, and the permittivity, ϵ, of the dielectric material determine L and C. In this thesis R and G is small compared to ωL and ωC, so the impedance is approximately:

$$Z_o \approx \sqrt{\frac{L}{C}} \tag{3.5}$$

3.1.1 Stripline Transmission Line and Coaxial Transmission Lines

There are two standard types of transmission lines used in this work: the stripline transmission line and the coaxial transmission line [25]. The former is the type of transmission line in printed circuit boards and the latter is the geometry of the

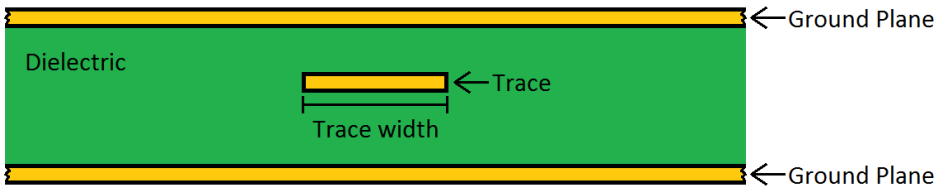

Figure 3.2: The cross section of a stripline transmission line.

patch cables (coaxial cable) that will be used when measuring the test board and the prototype HEC baseplane.

The stripline consists of two metal ground planes with a small rectangular metal strip placed in the middle (a constant separation from the ground planes) as the signal line. In this thesis the metal strip will be referred as a trace (not to be confused with TDR traces discussed later). Figure 3.2 shows a cross section of this geometry. The space between the ground planes is filled with a dielectric, with the exception of the signal line.

The coaxial transmission line consists of a cylinder of conductor surrounded by a shell of conductor with a gap between the two filled with dielectric. The inner conductor is the signal line and the outer conductor is the ground line, providing good shielding from external interference. Figure 3.3 shows a cross section of this geometry.

3.1.2 Skin Depth

At higher frequencies, electromagnetic induction results in the current being confined to a smaller layer on the surface of the conductor [24, 25]. The current density, J, drops off approximately exponentially as a function of depth into the conductor:

$$J = J_{surface} e^{-\frac{d}{\delta}} \tag{3.6}$$

The variable δ is known as the skin depth [24, 25]. It is well approximated by the equation:

$$\delta = \sqrt{\frac{1}{\pi f \mu \sigma}} \tag{3.7}$$

Where f is the frequency of a sine wave, σ is the conductivity of the conductor and μ is the permeability of the conductor.

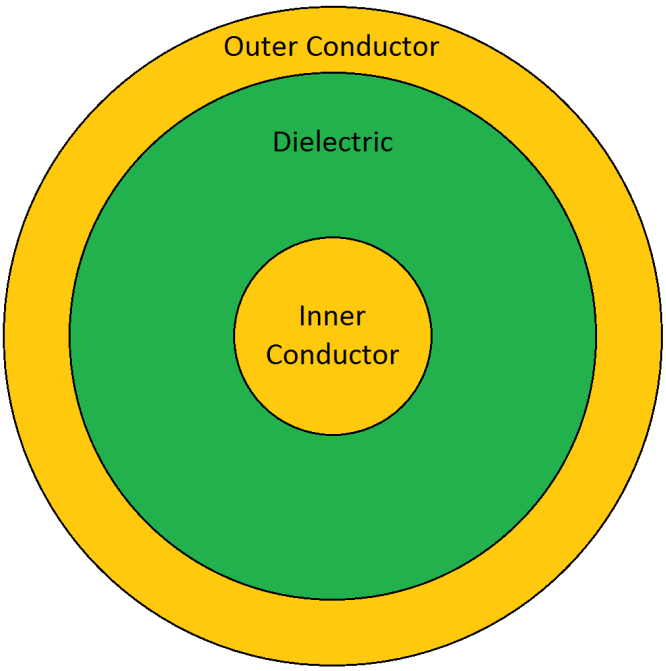

Figure 3.3: The cross section of a coaxial transmission line.

Confining the current to smaller portion of the conductor increases the resistance of the conductor. A good approximation is to treat the current as uniform within the skin depth and zero beyond. In this case, the resistance is proportional to the inverse of the skin depth and therefore the resistance is proportional to the square root of the frequency:

$$R \propto \frac{1}{\delta} \propto \sqrt{f} \tag{3.8}$$

The skin effect causes the resistance of a conductor to increase with increasing frequency.

3.1.3 Loss Tangent

The skin depth is not the only frequency dependent loss mechanism. Electromagnetic energy is also dissipated in the dielectric. This can be mathematically described by giving the permittivity, ϵ, a real, ϵ', and an imaginary, ϵ'', component [25, 27]:

$$\epsilon = \epsilon' - j\epsilon'' \tag{3.9}$$

With this complex permittivity Maxwell's curl equation becomes (for a single frequency sine wave: $\mathbf{E} = \mathbf{E}_o e^{j\omega t}$):

$$\begin{aligned} \nabla \times \mathbf{H} &= (\omega\epsilon'' + \sigma)\,\mathbf{E} + j\omega\epsilon'\mathbf{E} \\ &= (\omega\epsilon'' + \sigma)\,\mathbf{E} + \epsilon'\frac{\partial}{\partial t}\mathbf{E} \end{aligned} \tag{3.10}$$

The additional term effectively increases the conductivity of the dielectric ($\sigma_{eff} = \omega\epsilon'' + \sigma$), increasing the losses of the transmission line. This extra loss component is often described by the loss tangent, $\tan\delta$.

$$\tan\delta = \frac{\omega\epsilon'' + \sigma}{\omega\epsilon'} \tag{3.11}$$

Although the loss tangent varies with frequency, over small frequency bands it is approximately constant, resulting in an effective conductivity that scales almost linearly with frequency within that range.

$$\sigma_{eff} = \omega\epsilon'\tan\delta \tag{3.12}$$

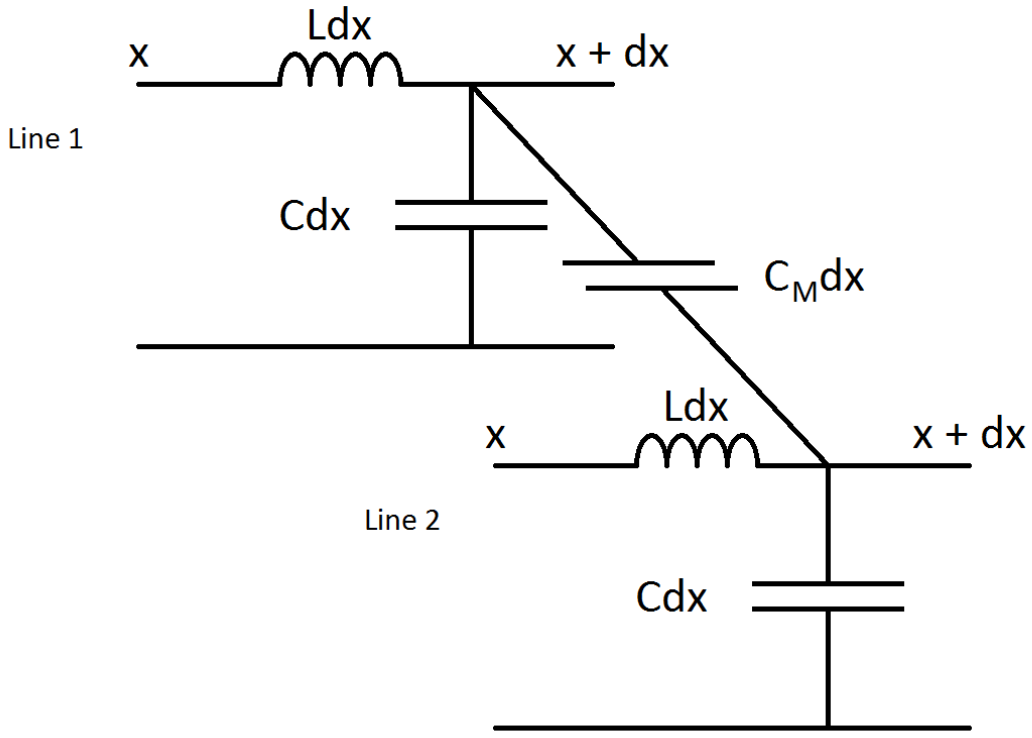

Figure 3.4: A depiction of two coupled lossless transmission lines modeled as infinitesimal inductors and capacitors similar to the RLGC model of a single transmission line. As well as the capacitance between the lines, the two inductors are coupled.

3.1.4 Coupled Transmission Lines and Crosstalk

When two transmission lines are near each other without shielding, the capacitance and mutual inductance between the two lines couple the lines. This can cause crosstalk between the transmission lines wherein a signal on one line (the aggressor) generates a waveform on another non-connected line (the victim). In most cases this effect is undesirable, causing interference and distorting signals.

For transverse electromagnetic waves, two parallel lossless (for simplicity) transmission lines with C_M capacitance per unit length between them and L_M mutual inductance per unit length can be modeled as in figure 3.4. When a signal is applied to one line, a forward traveling and a backward traveling (with respect to the applied signal) signal are generated on the other line. The voltage at the far end of the victim line is called the forward crosstalk, V_F, and the voltage at the near end is called the backward crosstalk, V_B.

We will assume that: the transmission lines are identical, they are of length l, the

speed of propagation is v, the lines are terminated into their characteristic impedance, line 1 has a signal, $V(t)$, applied at one end (the near end) while line 2 has no applied signal and the coupling between the lines is weak enough so that the crosstalk from line 2 to line 1 is negligible. Under these conditions the forward and backward crosstalks are given by [28][1]:

$$V_F = V_{victim}(x = l, t) = \frac{1}{2}\left(\frac{C_M}{C} - \frac{L_M}{L}\right)\frac{l}{v}\frac{dV\left(t - \frac{l}{v}\right)}{dt} \tag{3.13}$$

$$V_B = V_{victim}(x = 0, t) = \frac{1}{4}\left(\frac{C_M}{C} + \frac{L_M}{L}\right)\left[V(t) - V\left(t - \frac{2l}{v}\right)\right] \tag{3.14}$$

The forward crosstalk is a scaling of the derivative of the signal on the aggressor line, delayed by the length of time it takes the signal to propagate to that end. The longer the transmission line is, the larger the crosstalk signal is because the crosstalk signal builds up, propagating at the same rate as the signal on the aggressor line, much like a sonic boom. It is also interesting to note that the capacitive (caused by mutual capacitance) and inductive (caused by mutual inductance) crosstalks are of a different sign, causing the capacitive and inductive crosstalk to partially cancel.

The backwards crosstalk is the superposition of two scaled signals, one upright and one inverted, separated by twice the time it takes for a signal to propagate along the transmission line. From the equation, it looks like an upright signal is generated at the near-end while the signal is entering line 1 and an inverted signal is being generated at the far end while the signal is exiting line 1.

In the HEC baseplane, the time it takes a signal to go from the input to the output is a few nanoseconds, in comparison to the LAr pulses, which are hundreds of nanoseconds long, this is a very short period of time. Under these conditions the backward crosstalk is approximately:

$$V_B \approx \frac{1}{2}\left(\frac{C_M}{C} + \frac{L_M}{L}\right)\frac{l}{v}\frac{dV(t)}{dt} \tag{3.15}$$

This has the same form as the forward crosstalk, but now the capacitive and inductive coupling sum, resulting in more backward crosstalk than forward crosstalk.

[1] In this source the solution is given in Laplace space instead of the time domain.

3.2 S-Parameters

Scattering parameters [24, 25], also known as S-parameters, characterize the electrical response of linear multi-port networks. Linear networks attenuate and phase shift sine waves. Moreover, when a single frequency sine wave is input into one port, the output at all other ports are sine waves of the same frequency (eigenfunction). As mentioned previous, transmission lines share this characteristic and are a 2 port linear network.

S-parameters are a type of frequency dependent response function. By numerating the ports of a network (1 to n), the i, jth S-parameter can be defined by:

$$S_{ij} = \left.\frac{b_i}{a_j}\right|_{a_{l\neq j}=0} \tag{3.16}$$

Where the equation is evaluated with $a_l = 0$ for all $l \neq j$. The a_i and b_i are defined in terms of the impedance at port i, $Z_{p,i}$, the voltage at the port i, V_i, and the current at port i, I_i:

$$\begin{aligned} a_i &= \frac{1}{2\sqrt{Z_{p,i}}}\left[V_i(x,t) + Z_{p,i}I_i(x,t)\right] = \frac{V_{in,i}(t)}{\sqrt{Z_{p,i}}} \\ b_i &= \frac{1}{2\sqrt{Z_{p,i}}}\left[V_i(x,t) - Z_{p,i}I_i(x,t)\right] = \frac{V_{out,i}(t)}{\sqrt{Z_{p,i}}} \end{aligned} \tag{3.17}$$

The last term shows a_i and b_i in terms of the voltage of a wave entering, $V_{in,i}(t)$, and leaving, $V_{out,i}(t)$, port i. The square of this gives the power, so a_i and b_i are related to the power entering and leaving port i.

The S-parameters give a relationship between the a_i and the b_i in the form of a matrix relation:

$$\begin{pmatrix} b_1 \\ b_2 \\ \vdots \\ b_n \end{pmatrix} = \begin{pmatrix} S_{1,1} & S_{1,2} & \cdots & S_{1,n} \\ S_{2,1} & S_{2,2} & \cdots & S_{2,n} \\ \vdots & \vdots & \ddots & \vdots \\ S_{n,1} & S_{n,2} & \cdots & S_{n,n} \end{pmatrix} \begin{pmatrix} a_1 \\ a_2 \\ \vdots \\ a_n \end{pmatrix} \tag{3.18}$$

The S-parameters have intuitive interpretations for voltage waves. The magnitude of the S-parameter represents the amount of transmission or reflection, while the phase of the S-parameter represents the phase shift in traveling from one port to another. Conveniently the S_{ii} are precisely the reflection coefficient for the ith port, Γ_i, and

the S_{ij} are the transmission coefficients from jth port to the ith port, $T_{j\to i}$.

S-Parameters of Transmission Lines

S-parameters of transmission lines often have a pattern of ripples when displayed versus frequency (if displayed to a sufficiently high frequency) as in figure 3.5. At certain frequencies the reflections in the device can cancel each other, resulting in lower reflection and higher transmission at those frequencies. Similarly, there are frequencies that result in higher reflection and lower transmission. The ripples in the transmission and reflection occur at the same frequency, but 180° out of phase. If there is a large amount of reflection then there is less transmission, and vice versa.

In the case of a simple non-50 Ω transmission line the ripple pattern (as shown in figure 3.5) can easily be calculated by:

$$f_n = n\frac{v}{4L} \tag{3.19}$$

Where f_n is the n^{th} reflection or transmission local extremum (reflection minima if n is even, maxima if odd), L is the length of the transmission line and v is the speed of propagation.

The addition of the skin depth effect (or other frequency dependent losses) adds a downward slope to the S-parameters (figure 3.6). When multiple sources of reflection are added (multiple connectors or multiple transmission lines) the ripple pattern becomes significantly more complicated as in figure 3.7.

For two coupled transmission lines the ports are assigned as in figure 3.8. S_{31} is the backward crosstalk from line 1 to line 2, and S_{41} is the forward crosstalk from line 1 to line 2.

3.3 Time Domain reflectometry

Time Domain Reflectometry (TDR) [29, 30, 31] is a method of using the reflection of electrical signals to measure aspects of a transmission line in a method similar to radar. A long square wave (500 mV amplitude) is fed into a transmission line by a function generator with 50 Ω impedance. Changes in impedance cause partial reflections of the wave according to equation 3.4. The further along transmission line a change in impedance takes place, the later the reflection effected by it will reach the

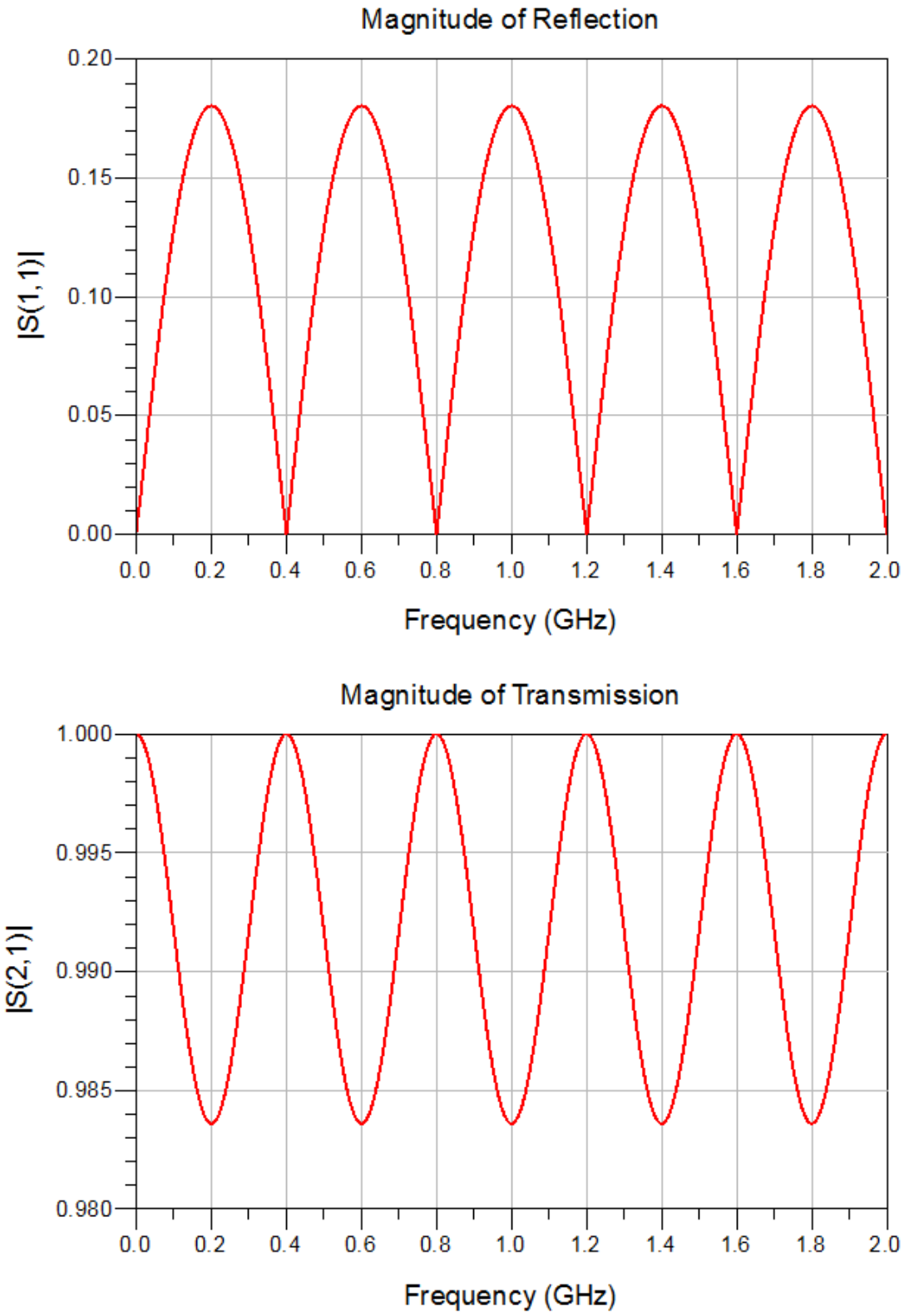

Figure 3.5: S-parameters (magnitude of S_{11} and S_{21}, equivalent to the reflection and transmission coefficient respectively) of a non-50 Ω ideal transmission line. Notice the reflection minima occur at the same frequencies as transmission maxima, and vice versa.

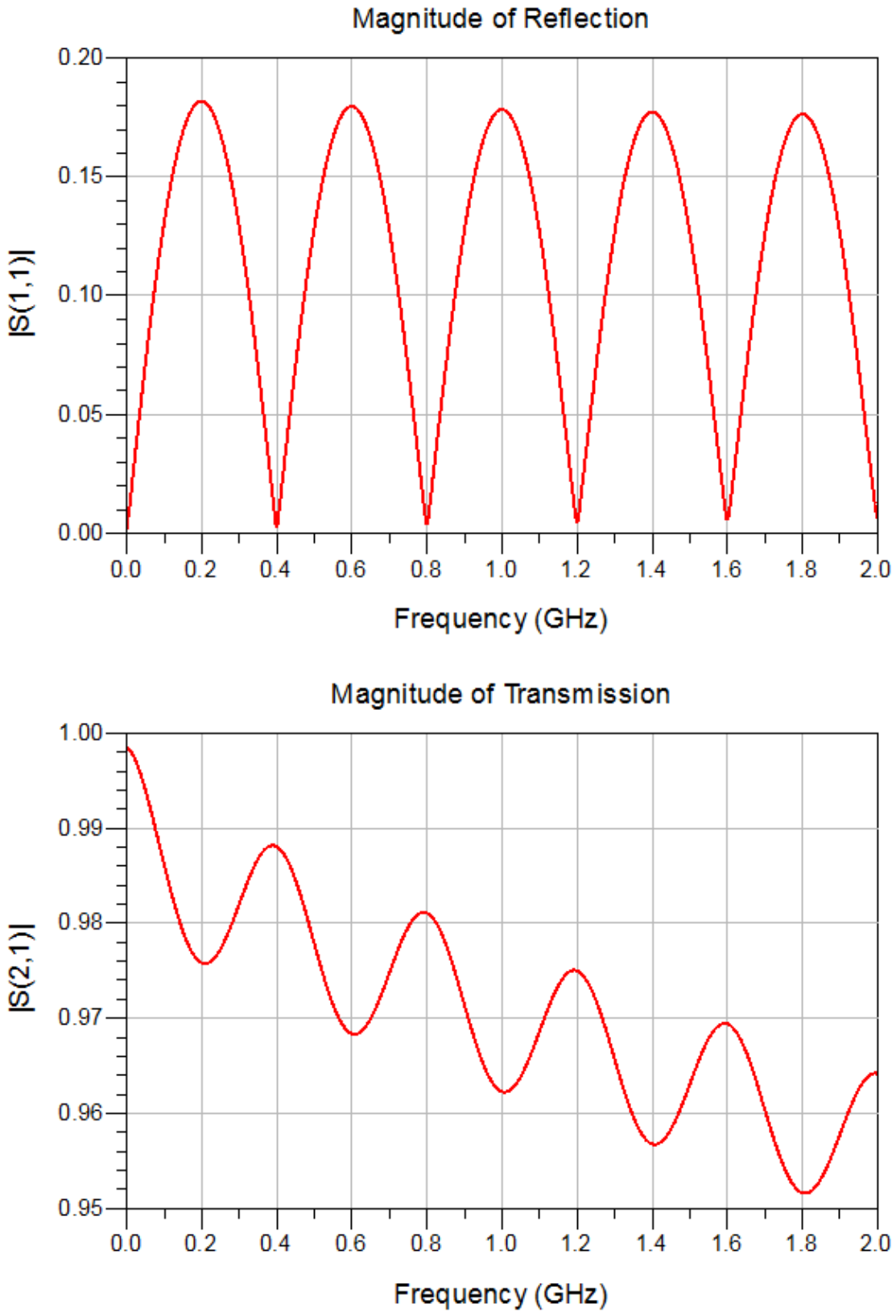

Figure 3.6: S-parameters (S_{11} and S_{21}, equivalent to the reflection and transmission coefficient respectively) of a non-50 Ω lossy transmission line. NB: since the skin effect is frequency dependent, then the transmission decreases with frequency.

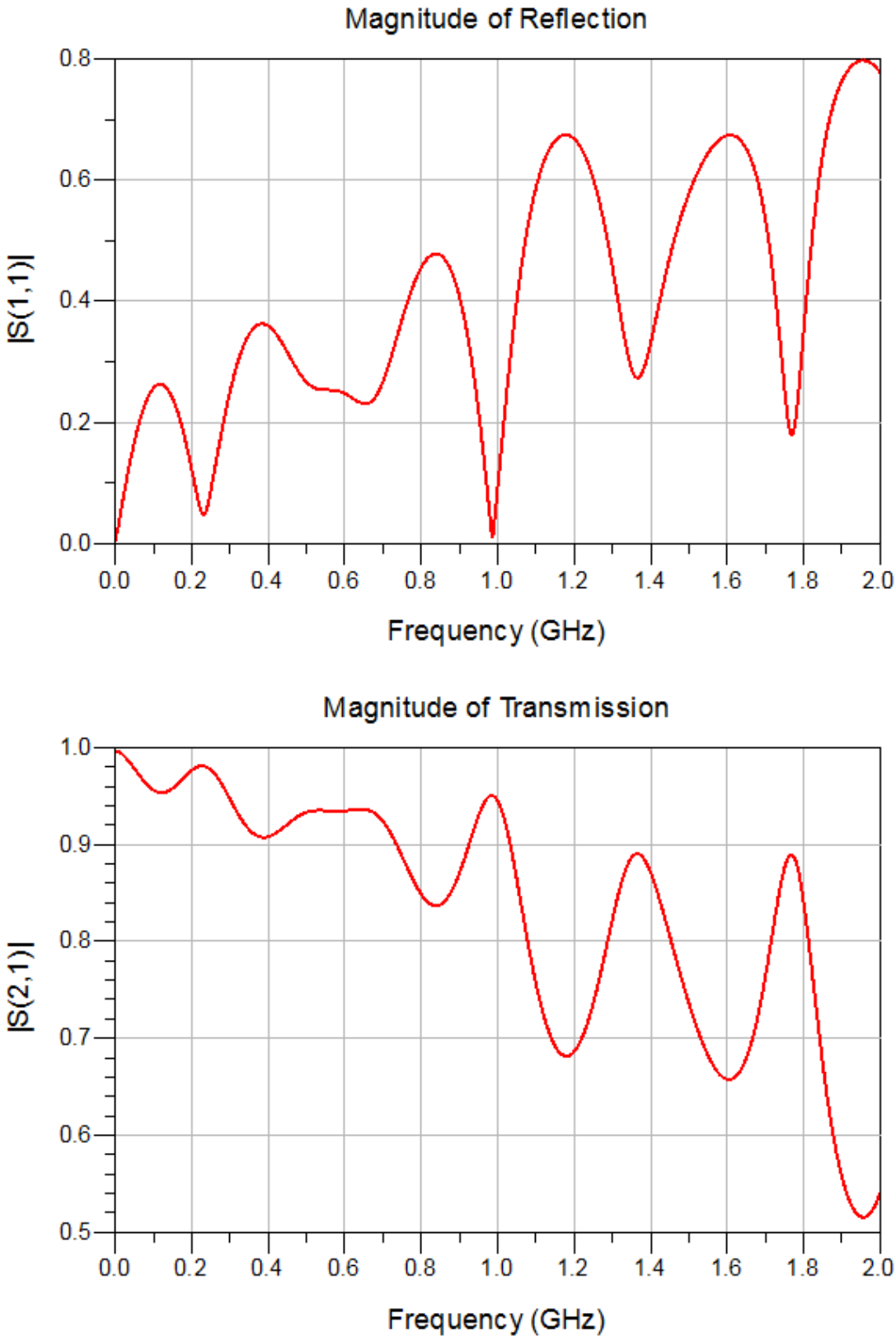

Figure 3.7: S-parameters (S_{11} and S_{21}, equivalent to the reflection and transmission coefficient respectively) of a device with multiple connectors and transmission lines providing many sources of reflection and creating a complex pattern of ripples in the S-parameters.

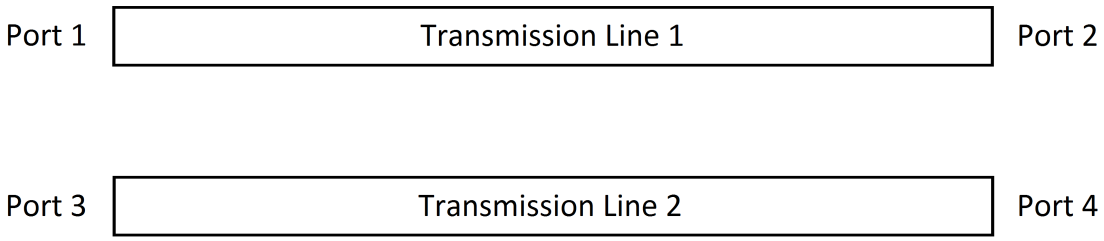

Figure 3.8: Port assignment for two coupled transmission lines.

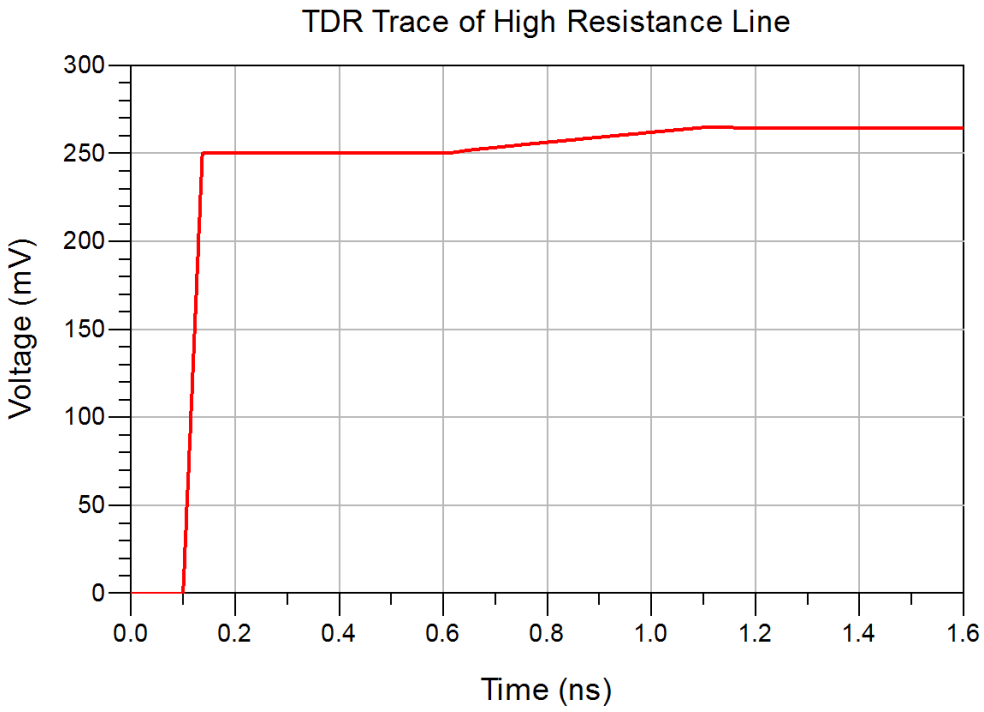

Figure 3.9: A Time Domain Reflectometry trace highlighting a 50 Ω transmission line with high resistance per unit length in between two ideal 50 Ω transmission lines.

transmitting end of the cable, allowing for areas of different impedance to be mapped out. A device that does this is called a Time Domain Reflectometer (TDR).

Time Domain Reflectometry can measure the impedance of transmission lines, examine the impact of connectors and see the presence of resistance or conductance. From the measured voltage, the impedance of the lines can be calculated. High resistance or conductance can also be observed by a permanent raising or lower of the reflected voltage (often a sloped increase or decrease for lossy transmission line components) as seen for resistance in figure 3.9. Changes in inductance and capacitance can be identified from their reflections. Increased inductance increases the impedance and causes upright reflection. Similarly, increased capacitance lowers the impedance and causes inverted reflection.

Figure 3.10 shows the simulation of the leading edge of a long square-wave (0 to 500 mV, 50 ps rise time) being fed into a transmission line by a function generator with a 50 Ω impedance. The pulse first enters an ideal 50 Ω transmission line resulting in 250 mV at the insertion end. At 0.75 ns the leading edge of the square wave reaches a connector and part of the wave is reflected. This reflection reaches the

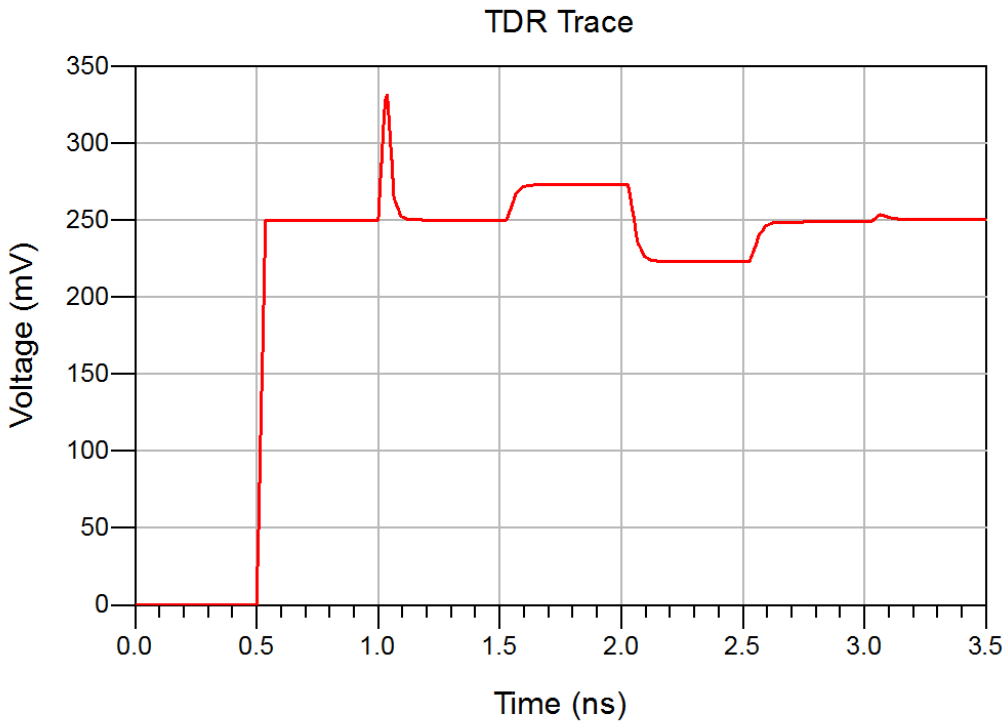

Figure 3.10: A Time Domain Reflectometry trace of a 50 Ω transmission line connected to a connector (high inductance) then to a 50 Ω, a 60 Ω and a 40 Ω transmission line before being terminated in a 50 Ω resistor.

time domain reflectometer at 1 ns, resulting in a large amplitude (but short) rise in voltage. Further along the transmission line there is a 60 Ω transmission line segment followed by a 40 Ω transmission line segment, creating higher and lower voltage at the insertion end. Finally the transmission line is terminated into a 50 Ω terminator resulting in a final voltage of 250 mV.

The example is figure 3.10 is a simplistic demonstration. When there are multiple large sources of reflection in the device under test, the waves are reflected multiple times which obscures the reflections from elements further down the line. A high impedance connector can obscure elements after itself by partially reflecting waves, so that frequency components are already missing once the wave has reached the second element. Connectors with high and low impedance components can continuously reflect signals between each other, slowly releasing some of the energy at each reflection. This can make it hard to properly gauge the impedance of transmission lines that follow connectors.

Transmission of the square waveform can also be examined and is called Time Domain Transmission. When observing the waveform transmitted through a transmission line it is more difficult to use the shape to determine the impedance of components, but it can be used to gauge the amount of loss. This can also be used to examine crosstalk. The forward crosstalk signal builds up as it propagates, making it difficult to isolate the source of the crosstalk, but for backwards crosstalk the sources are separated in time just like time domain reflectometry, allowing the location of the crosstalk source to be determined. Because the forward crosstalk looks like the derivative of the signal, the forward crosstalk in time domain reflectometry will look like a short spike in the voltage (possibly negative). For backward crosstalk the rise time is likely short enough that the backwards crosstalk looks like another square wave instead of a spike.

In this thesis the oscilloscope trace created on the TDR will be referred to as a Time Domain Reflection trace (TDR trace) for reflection and Time Domain Transmission trace (TDT trace) for transmission and crosstalk.

3.4 Calculating the Response of Linear Circuits

The response of a linear circuit to an input (voltage or current sine wave, step function, etc.) can be calculated as a function of time and frequency by using Laplace transform techniques. Programs exist that can make these calculations under the generic name SPICE[2] [32]. These programs allow the user to input a circuit with standard circuit elements like resistors, capacitors, transmission lines etc. It is also possible to input S-parameters to represent a circuit element or to input the Laplace transform of the element.

We will make use of this software to calculate the response of our devices to a step voltage. The S-parameters we derive from measurements will be used as a circuit element. This will give us the expected TDR/T trace of derived S-parameters as a function of time. We will also make use of this software to combine modeled components together, calculated the S-parameters of the combined system and calculate the TDR/T traces of models.

We are using of Keysight Technologies' Advanced Design System (ADS). This contains SPICE and other calculation techniques. More details of the exact use will

[2]SPICE can do more than linear circuits

be given in section 5.2.

Chapter 4

S-Parameter Measurement

This chapter examines making S-parameter measurements of printed circuit boards using a Time Domain Reflectometer (Tektronix DSA 8300 Digital Serial Analyzer with 2 80E04 20 GHz sampling modules and 17.5 ps rise time) and Tektronix' IConnect software. IConnect is introduced and some of the issues with extracting S-parameter data from TDR measurements are examined. A procedure for making accurate S-parameter measurements is established. Many of the measurements are made using a test board, which is introduced in this chapter.

4.1 Test Board

The Hadronic Endcap Calorimeter baseplane is a complicated circuit board. To make initial modeling easier a simple circuit board was designed at TRIUMF and manufactured by Sunstone Circuits (quickturn process [33]). This board, referred to as the "test board," will be used for several preliminary experiments in this chapter and in chapter 6.

The test board consists of 2 signal layers (layers 2 and 5) and 4 shield layers (layers 1, 3, 4 and 6) separated by layers of FR4 laminate core and bonding ply (relative dielectric constant 4.5 ± 0.1) with thickness and tolerances shown in table 4.1 [34]. The layout of the signal layers is depicted in figure 4.1. There are three widths of striplines on the board: 6 mil[1], 7 mil and 8 mil in nominal lengths of 3", 5" and 7". For each width and length there are 5 parallel striplines. Viae[2] are used to connect

[1] 1 mil = $1/1000^{\text{th}}$ of an inch or 25.4 μm.

[2] The connection between layers of a printed circuit board is known as a via or (plural) viae.

Layer	Thickness (mil)	Tolerance (mil) (±)
Layer 1	1.7	0.4
Bonding ply	6.4	0.7
Layer 2	1.4	0.4
Laminate Core	14	2
Layer 3	1.4	0.4
Bonding ply	8.4	0.8
Layer 4	1.4	0.4
Laminate Core	14	2
Layer 5	1.4	0.4
Bonding ply	6.4	0.7
Layer 6	1.7	0.4

Table 4.1: The layer stackup of the test board showing the nominal size and tolerances for each layer (layers 1 - 6 are copper, bonding ply and laminate core are FR4) [34].

the striplines to solder pads on the top layer. One pin of a two-pin connector is soldered to this pad and the other pin is soldered to the ground sheet (see figure 4.2).

Patch cables were made to connect this board to the TDR. They were made from 50 Ω RG 316 coaxial cable which is rated to 12.4 GHz (CINCH Connectivity Solutions, Part Number: 415-0029-024 [35]). SMA connectors are used to connect to the TDR and another connector was made to connect to the two-pin connectors of the test board. Figure 4.3 shows the test board connected to the time domain reflectometer for measurements.

4.2 Tektronix' IConnect Software

Tektronix' IConnect Software is Time Domain Reflectometry software designed for high speed interconnect characterization [36]. The software is intended for measurement, testing, modeling and validation of signal lines in cables, connectors, printed circuit boards, etc. Among other capabilities, IConnect can extract S-parameters from TDR/T measurements (including crosstalk), de-embed[3] measurement systems and has procedures to make calibration and de-embedding measurement systems easier. S-parameter extraction can be done either by loading in appropriate TDR/T traces (with calibration measurements (discussed below)) or by using the S-Parameter

[3]Removing the effects of patch cables and other electrical and mechanical systems used in the measurement process put not part of the device under test.

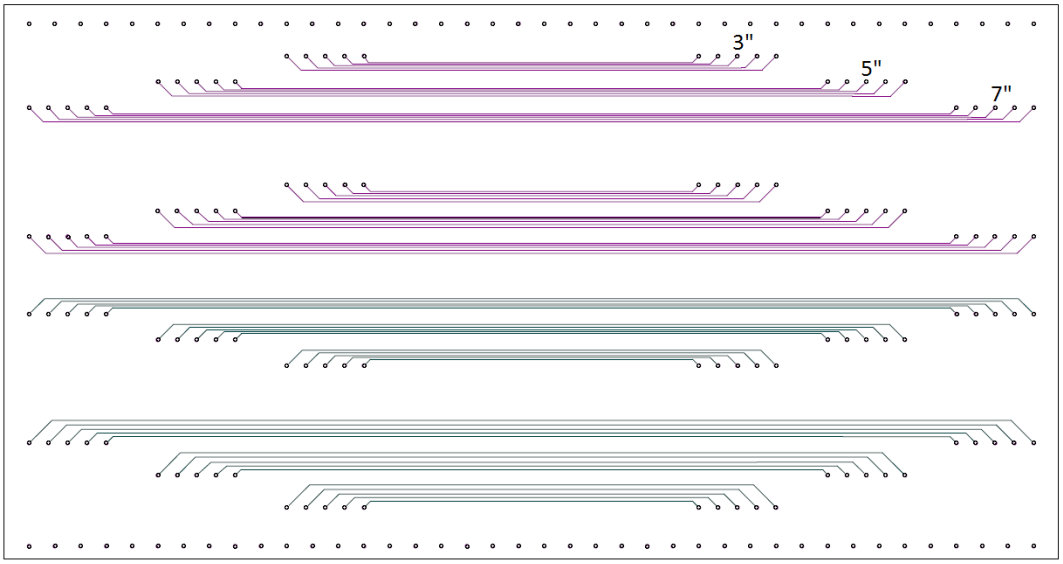

Figure 4.1: The layout of the test board showing the signal layers (layer 2 and 5) in purple (top) and blue (bottom) respectively.

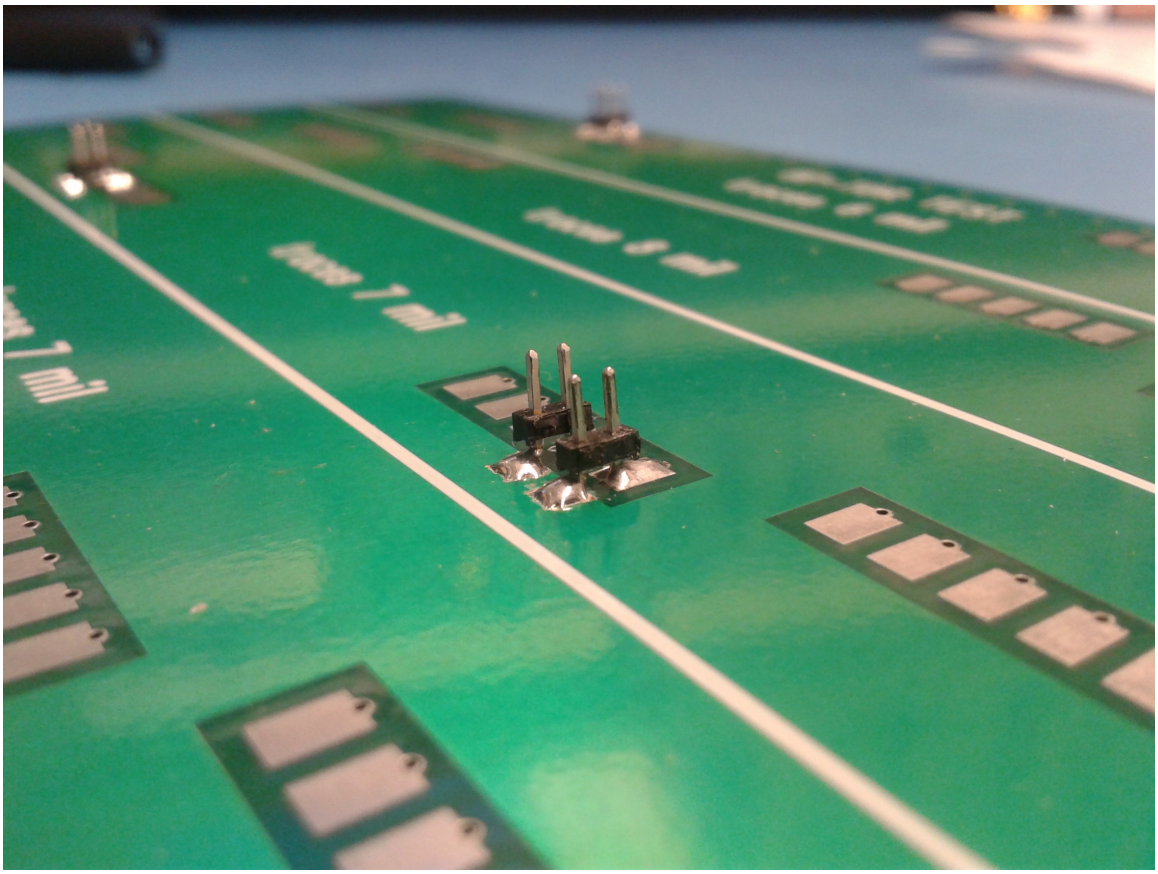

Figure 4.2: A picture of the two-pin connectors soldered to the test board.

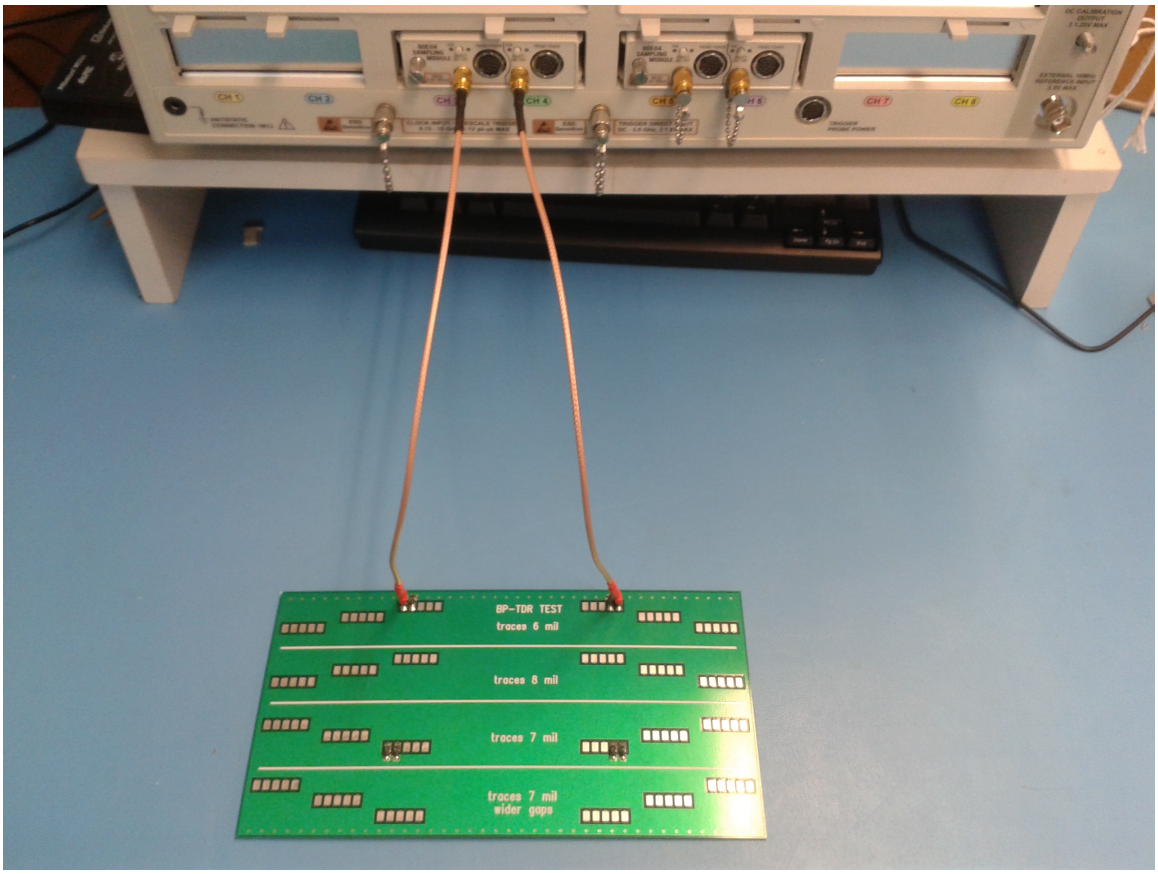

Figure 4.3: A picture the test board connected to the TDR for measurements.

Extraction Wizard, which controls the TDR and guides the user through setting up the TDR for the needed measurements. In this work, IConnect is used solely for S-parameter extraction, so this section discusses the various options that IConnect has for this. This will be discussed in the context of the S-Parameter Extraction Wizard, but if all the necessary measurements are made without the wizard then IConnect can still estimate the S-parameters.

The S-Parameter Extraction Wizard first requests (optional) that the TDR channels be aligned in time (deskewed). This is done using a cable to connect each of the TDR channels in succession to the TDR Clock Output using the same cable for each channel. Afterwards, TDR/T measurements are made for all ports (default average of 100 measurements). In order to remove the effects of the measurement system, an additional measurement is needed. This can either be TDR measurements of the patch cables with nothing connected (open), TDR measurement of the patch cables shorted at the end (short) or TDT measurements of the patch cables connected end-to-end (through). In addition to this measurement, a TDR measurement of the patch cables with a 50 Ω load connected to the end (instead of the device under test) can be used. This additional waveform can be used by IConnect to improve S-parameter accuracy by helping to remove some of the effects of the connector to the Device Under Test (DUT) that could remain when using only open, short or through measurements. These open, short, through and load measurements are referred to as calibration measurements. With these measurements IConnect can estimate the S-parameters of the DUT, attempting to remove the measurement system.

It should be noted that IConnect cannot measure 3-port S-parameters. It can only measure 2-port transmission lines, or sets of 2-port transmission lines (crosstalk). If IConnect does not detect transmission from the excited port to the port it supposed to be connected to (between ports 1 and 2; and 3 and 4 in figure 3.8 on page 46), then measurements cannot proceed.

4.3 Isolating Device Under Test

Several tests were carried out using IConnect to extract S-parameters from the test board. As seen in figure 4.4, using only the open, short and through measurements yield almost identical results for the test board, within the variation of repeated measurements in figure 4.5. Adding the 50 Ω measurement, however, heavily changes the extract S-parameters. In the case of a 50 Ω coaxial cable with SMA connectors, the

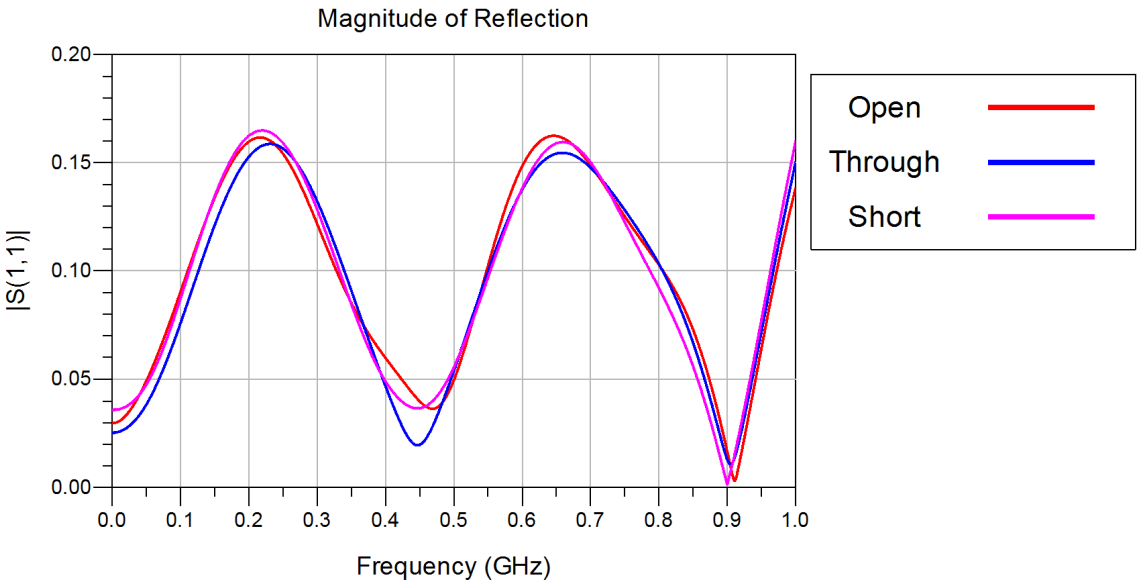

Figure 4.4: Extracted $|S_{11}|$ for the test board using open, short and through calibration. Note that the variation is less than that of the repeated measurements in figure 4.5.

magnitude of S_{11} extracted using only the open calibration yielded $\sim 30\%$ reflection while the magnitude of S_{11} extracted using both the open and load measurements yielded $\sim 3\%$ reflection (see figure 4.6). Strong reflection from an impedance matched cable with low reflection connectors is unexpected. Furthermore, when the extracted S-parameters are used to calculate a TDR trace (using ADS), S-parameters extracted using open and load measurements had an appropriate impedance (near 50 Ω) while the S-parameters extracted using open measurements had far too much reflection (see figure 4.7). Therefore for low reflection connectors (to device under test), open and load calibration should be used.

For the test board, IConnect is not capable of isolating the device under test. When the extracted S-parameters are used to calculate a TDR trace, the open and open and load tests get significantly different results for the near-end connector (figure 4.8). It is difficult to determine which–if either–is a good approximation of the actual test board near the front end connector. Of more worry, the far end connectors are identical in both of the TDR traces calculated from S-parameters and the measured TDR trace. This shows that the effects of connectors are not being removed at the far end. As also seen in figure 4.8, the connectors have high impedance and causes a significant amount of reflection. This discontinuity may make it difficult for IConnect

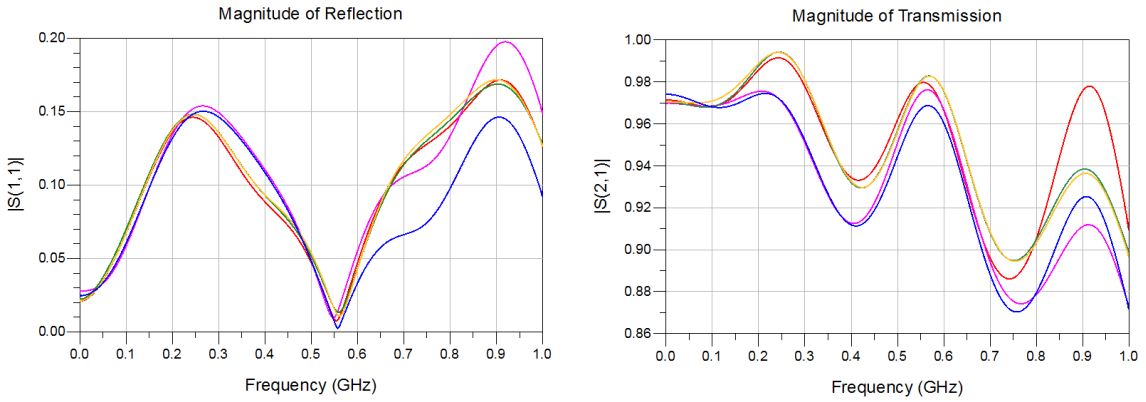

Figure 4.5: Plot of repeated individual measurements of $|S_{11}|$ and $|S_{21}|$ of the same stripline on the test board. Open calibration was used in all of the measurements shown. Each single measurement was setup from scratch.

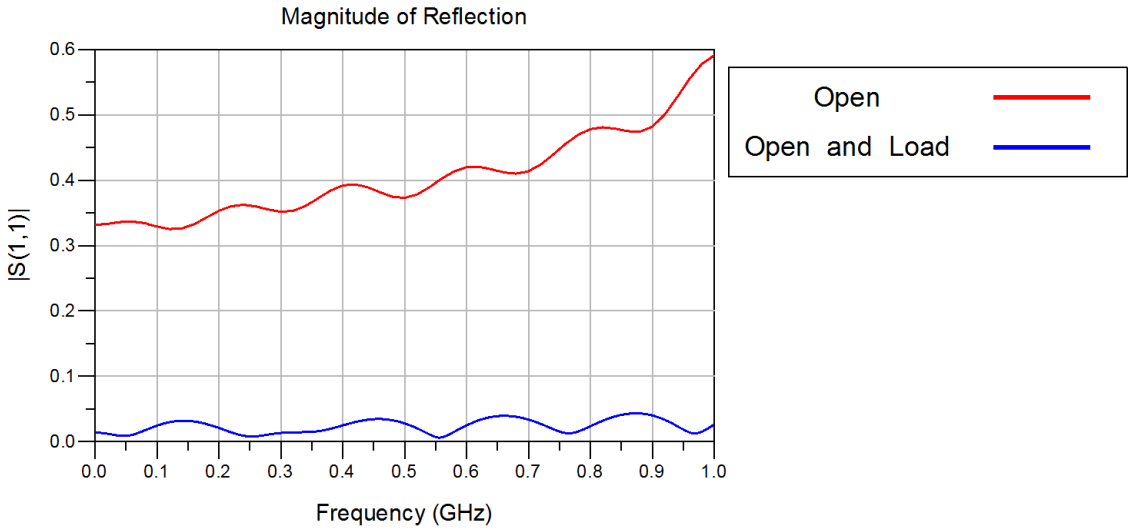

Figure 4.6: Extracted $|S_{11}|$ of a 50 Ω coaxial cable using open; and open and load calibration.

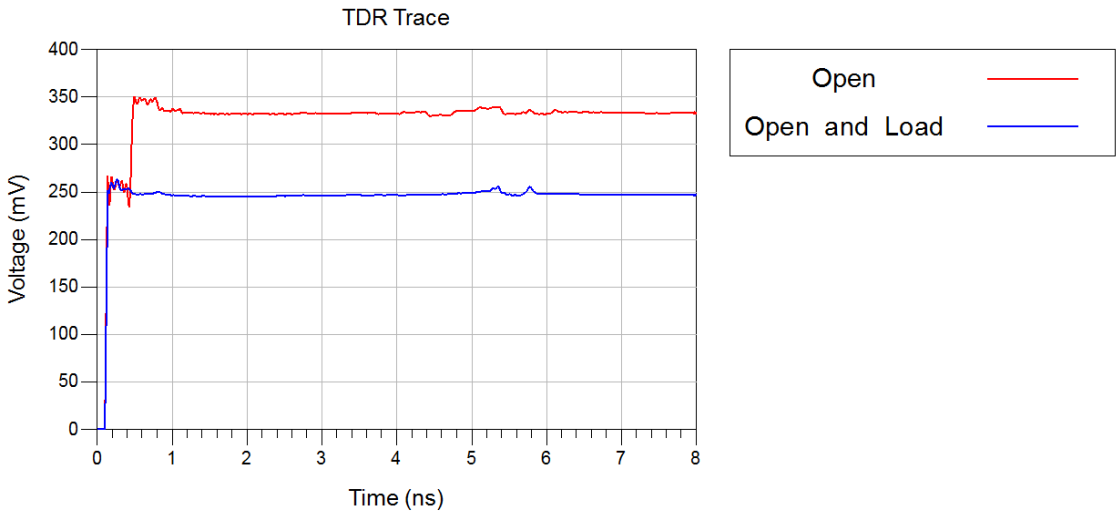

Figure 4.7: The TDR trace of a coaxial cable and the TDR traces calculated from extracted S-parameters using open; and open and load calibrations.

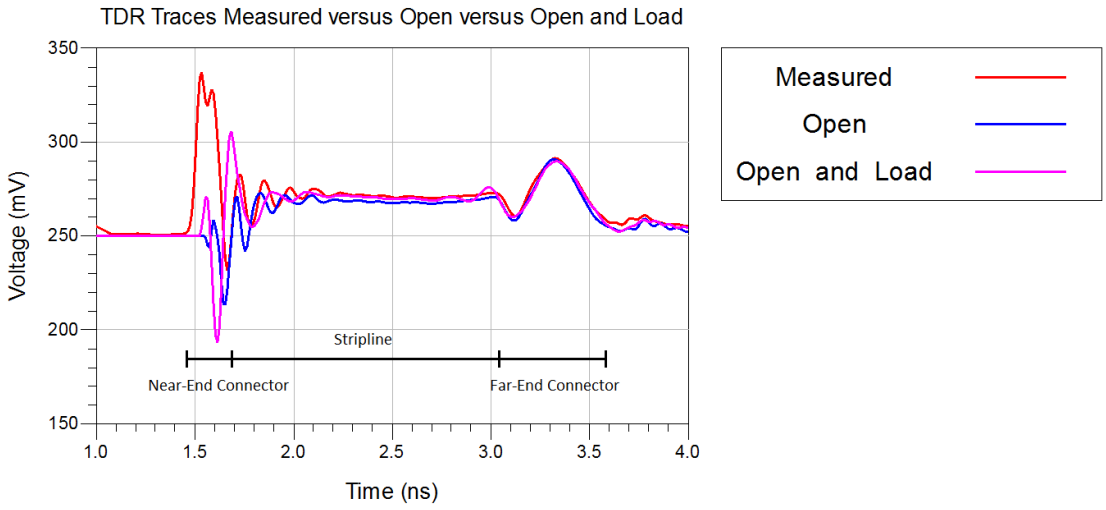

Figure 4.8: The TDR trace of a test board interconnect and the TDR traces of the test board interconnect calculated from the extracted S-parameters using open, and open and load calibrations.

to remove the connector of the patch cables.

The effects of patch cables are only partially removed by IConnect. The cables contribute a significant amount of attenuation at higher frequencies. The loss of higher frequencies increases the rise/fall time and lowers the amplitude of reflections. If the patch cables were completely removed from the S-parameters then, in TDR traces calculated from the extracted S-parameters, connector peaks should be higher and rise faster than the measured TDR traces. This is not the case, showing that the patch cables are not entirely removed. The attenuation permanently destroys the high frequency information. Furthermore, there are ripples in the S-parameters that would correspond to transmission lines with an electrical length[4] similar to the combined patch cables and test board. When the test board was measured using patch cables that have more reflection at the TDR connectors, ripple amplitude was increased (see figure 4.9). This suggests that reflections elsewhere on these cables are contributing to the measured S-parameters.

[4]

$$f_n = n\frac{1}{2T} \tag{4.1}$$

Where f_n is the n^{th} reflection extremum and T is the propagation time, similar to equation 3.19 in section 3.2

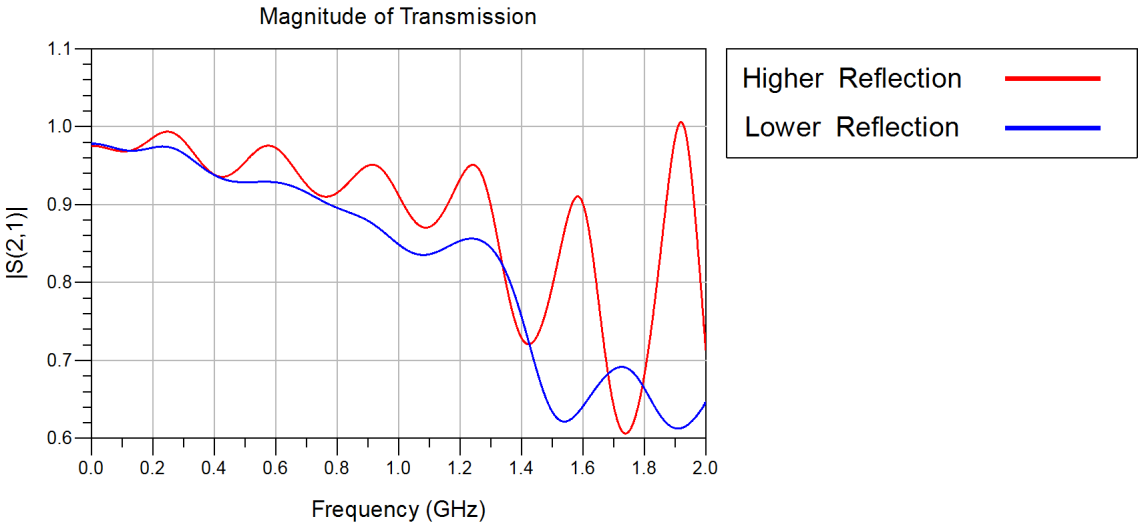

Figure 4.9: Overlaid plots of S_{21} for patch cables with high and low amounts of reflection at the TDR connector. Note the large reduction in the ripples for the low reflection patch cable.

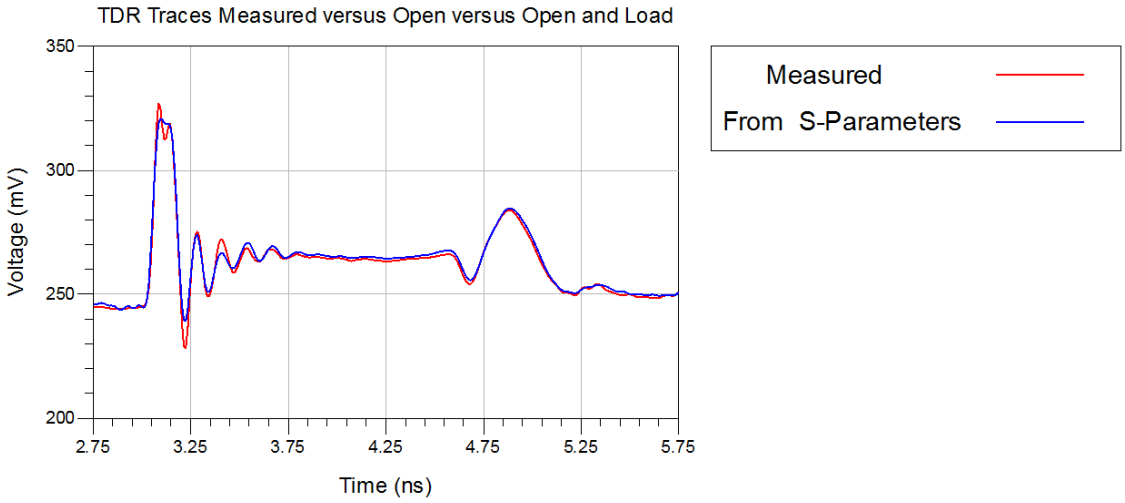

Figure 4.10: Plot of measured TDR traces of a test board trace and a TDR traces calculated from measured S-parameters of the combined test board and patch cable system.

4.3.1 Method for S-Parameter Measurements

TDR traces calculated from extracted S-parameters better match measured TDR traces when low reflection SMA connectors are used. Our measurement system uses patch cables that connect to the TDR using SMA connectors but then connect to printed circuit boards using high reflection connectors (ERNI and FCI connectors on prototype board, two-pin connectors on test boards). Treating the printed circuit board and patch cables as the device under test, extracting S-parameters of the combined patch cables and circuit board system, provides a low reflection connection to this system. Figure 4.10 shows a section (focused on the printed circuit board) of the measured TDR traces versus the TDR traces calculated from the extracted S-parameters of the test board and patch cables. They are in very close agreement, with only slight differences at the near end connector. These differences could be caused by high frequency cut-off because the S-parameters were only measured to 15 GHz, while the TDR has 20 GHz sampling modules.

Chapter 5

Simulation Software

This chapter introduces the software used to model the prototype HEC baseplane: Keysight Technologies' Electromagnetic Professional (EMPro) for 3D electromagnetic simulation and Keysight Technologies' Advanced Design System (ADS) for combining EMPro simulations, modeling some components, calculating S-parameters of the model and calculating TDR traces.

5.1 Electromagnetic Professional (EMPro)

Keysight Technologies' Electromagnetic Professional (EMPro) [37, 38, 39] is a 3D electromagnetic simulation software with implementations of both the Finite Element Method (frequency domain) and Finite Difference Time Domain method. This thesis uses only the Finite Element Method (FEM).

EMPro allows for the creation of 3D models using a built in design interface. Once the geometry is specified, the type of material must be assigned to each component and electrical ports must be assigned. An appropriate 'mesh' must be made and then the simulation engine can run, producing S-parameters or other information. The next sections describe the various options, settings and parameters of EMPro that are used in this thesis. Information on the mathematics of FEM simulation can be found in appendix A.

5.1.1 Material Definitions

Each object in an EMPro simulation must have a material assigned and the properties must be defined in EMPro. Many options are available for defining the electrical

properties of the material, though, in this work, only non-dispersive material models are used because more advanced models require knowledge of parameters that were not available for our materials. As such, the dielectric constant and loss tangents remain constant in simulations.

For dielectrics, one available method makes use of the loss tangent. This option is always used in this thesis because the loss tangent is available for all of the dielectrics we used. The loss tangent will correct the conductivity of the material at every frequency that is solved for.

For conductors, a "surface conductivity correction" may be enabled. Counter intuitively, if this option is disabled then the inside of conductors is not meshed and a conductivity correction is applied on the surface. If this option is enabled then no correction is applied and the inside of the conductor has to be meshed. If enabled, very small mesh sizes are required to obtain appropriate frequency dependent resistance. For the lengths of transmission lines used in this thesis, at 100 MHz the size of mesh cells required for skin depth simulation would require more than the 128 Gb of RAM that were available. Therefore the surface conductivity correction option is never used.

5.1.2 Padding and Boundary Conditions

EMPro simulations require a boundary where the simulation terminates. EMPro allows for many different boundary conditions such as absorbing, perfect electric conductor and perfectly matched layers. For many types of simulations it is desirable to have a gap between the 3D model and the boundary. For this reason EMPro allows for a layer of padding to be specified around the model (gap can be specified for the positive and negative x, y and z axes). The discussion of this is limited because, as is shown in section 6.5, the boundary conditions and padding have little effect on our stripline simulations.

5.1.3 Ports and Circuit Components

Ports are where the electromagnetic pulse is injected into the model and where the voltage across the port is measured to determine transmission. The most simplistic port consists of a line connection between two conductors with some standard impedance (always 50 Ω in this thesis). To prevent the magnetic field near this line from being unbounded and due to computational constraints, EMPro approximates

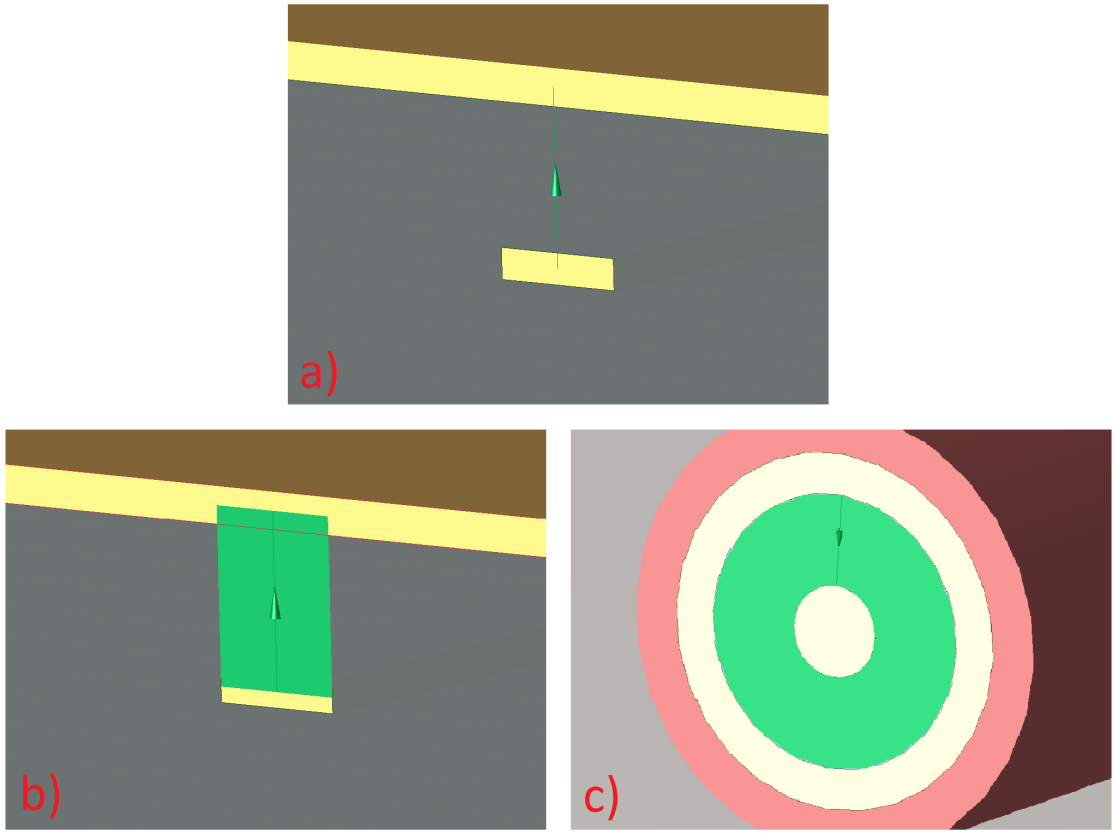

Figure 5.1: Images of a) a line feed port (green line) b) a sheet feed port (green sheet) and c) a coaxial sheet feed port (green annulus).

this line as having a small width on the order of a picometer, but the small size still results in additional and parasitic (unwanted) inductance. In addition to this, forcing the current on a wide conductor through a single point can produce inappropriate current flow near the port on that conductor. To mitigate both of these issues, EM-Pro can also define a 'sheet feed' or a 'coaxial sheet feed' for the port. The sheet feed gives the port a width in one direction, allowing current to flow across the entire sheet, rather than through a line (see figure 5.1). The coaxial sheet feed is a specialized port allowing two rings to be connected to better simulate coaxial models.

5.1.4 FEM Mesh

A critical component of FEM simulations is generating the mesh. Creating it can be computationally intensive and, if done inappropriately, can generate incorrect results. In general, finer meshes create more realistic results, but decreasing mesh

size can significantly increase the computation time (both of the meshing process and of the electromagnetic solver). EMPro has a built in iterative mesher meant to create an appropriate mesh and give estimates of the error in the simulation. EMPro's mesher takes user defined mesh requirements (maximum mesh sizes defined for the surfaces, edges and corners of individual objects and universal maximum mesh size) to create an initial mesh satisfying those requirements, solves for the S-parameters at a specific frequency (usually the highest frequency simulated because this is typically the frequency that requires the smallest mesh for accurate simulation) then refines the mesh and solves for the S-parameters again. If the differences between S-parameters is less than some specified amount (less than 1% difference in all simulation in this work), then the mesh is kept, if not, the mesh is refined and the process repeats until the difference is small enough or the maximum number of refinements is reached.

Once a mesh has been generated, the electromagnetic field solver determines the S-parameters. An adaptive sweep is used in this thesis to determine the S-parameters in the frequency range of 0 to 15 GHz. The adaptive sweep uses an algorithm to approximate the frequency dependent S-parameters from all the directly solved frequencies. This can dramatically reduce computation time. The algorithm solves for S-parameters at specific frequencies (determined by the algorithm) until it deems it's approximation suitable.

The adaptive meshing can create very chaotic meshes (see figure 5.2) and fine meshing in areas where there is little interesting activity (e.g. far from the signal line or outside of the ground plates of a stripline, where there is almost no electromagnetic fields) if the initial mesh requirements are chosen poorly. This results in the mesh requiring large amounts of RAM, which increases the computation time or prevents simulations from running by exceeding the 128 GB of RAM that were available. Carefully and thoughtfully assigning initial mesh is important to minimize time and RAM requirement. This involves requiring fine initial meshing on important objects, such as signal lines and ground planes near the signal line, and coarse initial meshing on the ground planes and dielectric far from the signal line.

5.2 Advanced Design System (ADS)

Keysight Technologies' Advanced Design System [40] is electronic design software with a large number of automation features. It allows schematic design and simulation using various technologies including SPICE. In addtion, ADS has number features for

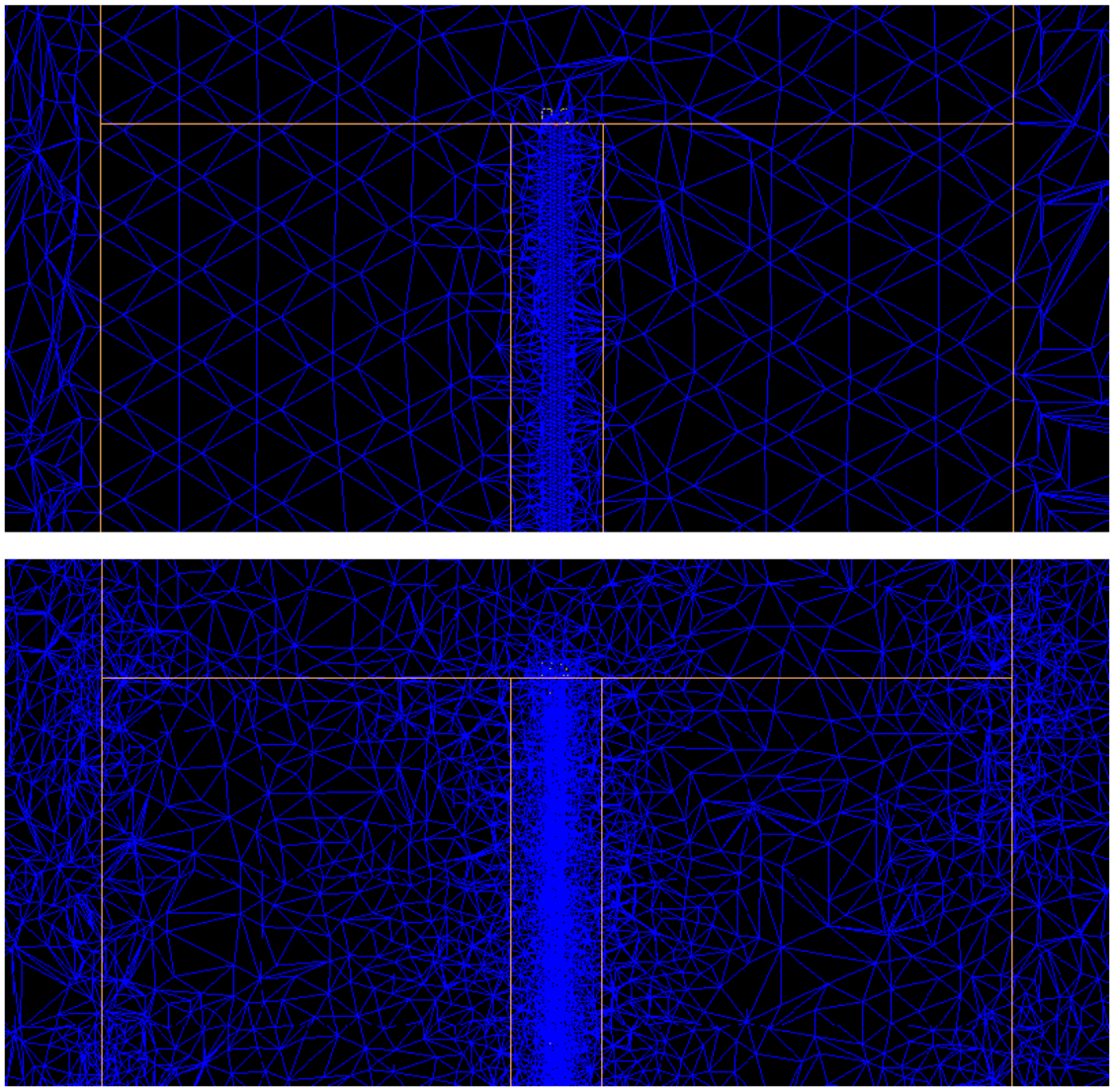

Figure 5.2: An example of the mesh after numerous refinements by the iterative meshing process (bottom) and a mesh where the initial meshing requirements were chosen so that little refinement was necessary (top), both with less than 1% difference between mesh refinements.

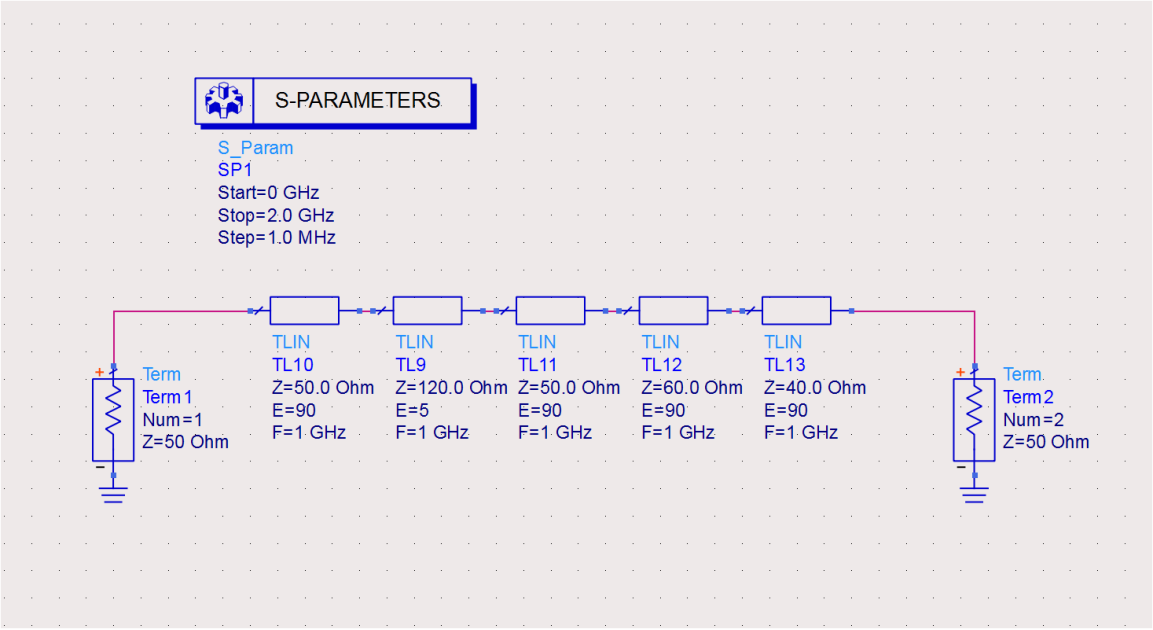

Figure 5.3: An Advanced Design System schematic for calculating 2-port S-parameters of multiple transmission lines.

designing and simulating various components, including coaxial cables and multilayer transmission lines.

The features used most in this thesis are S-parameter calculations (figure 5.3) and calculating TDR/T traces from S-parameter and other models (figure 5.4). ADS provides a suitable environment for combining together various models made using EMPro and ADS, allowing more complex models to be made from many less computationally intensive models.

ADS's coaxial cable model will be used in chapter 6 and 7 for modeling patch cables and the multilayer transmission line model in chapter 7 to model connectors. The coaxial cable model allows the geometry of a coaxial cable to be specified and then the response is calculated based on this geometry. The multilayer transmission line model allows for multiple layers of conductors separated by dielectric. Each conductor has a rectangular cross section. The characteristics of the component are solved for using techniques based on the method of moments and Green's function method. Both the coaxial and multilayer transmission line models calculate skin effect and conductor loss (loss tangent).

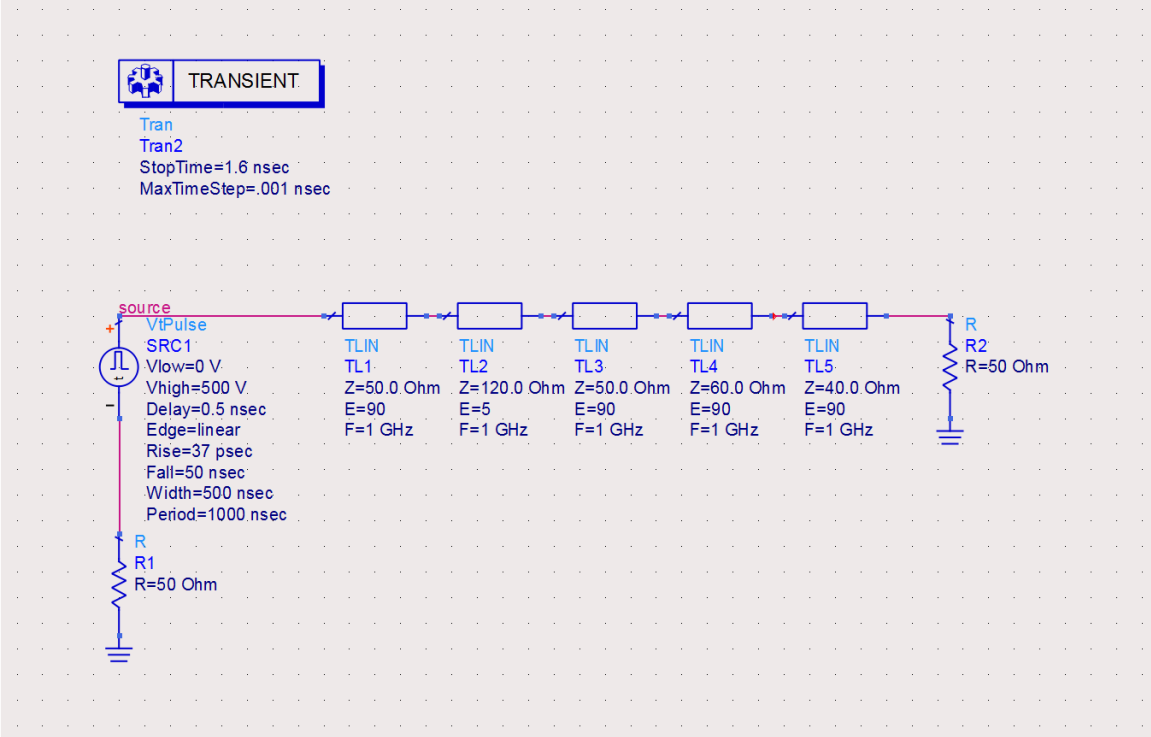

Figure 5.4: An Advanced Design System schematic for calculating the TDR trace of multiple transmission lines. A square wave is generated at the left end and the voltage measured at the point "source."

Chapter 6

Test Board Model and Measurements

Before attempting to model the prototype HEC baseplane, a model was made of the test board (introduced in section 4.1). The test board provides a simple problem that is used to refine and prove modeling and measurement techniques. This chapter will introduce a model of one of the test board transmission lines, compare the model with measurements and discuss the systematic uncertainties involved.

The work reported in chapter 4 demonstrated that our measurement system is only capable of measuring S-parameters of the combined patch cable and test board system, not the test board by itself. Because of this, all our measurements contain the patch cables. Therefore, the models must contain the patch cables in order to be compared with S-parameter measurements. Patch cable models are also needed to compare measured TDR traces with calculated TDR traces of the model.

The model will be created using striplines simulated in EMPro, connectors created in ADS using ideal transmission lines and patch cables created using coaxial cable models in ADS. Each component will be discussed and then combined as in figure 6.1. Measured TDR traces and TDR traces calculated from the model will be compared to identify problems with model components (e.g. impedance mismatch) and the model will be adjusted to correct these errors. The S-parameters of the model will then be compared to the measured S-parameters.

The measurements and models shown here are for a 6 mil wide stripline in the test board. The length of the stripline is $\approx 100\ mm$ (labeled as 3" on the test board, but this is not the actual full length of the stripline).

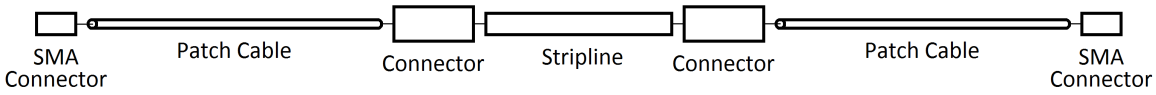

Figure 6.1: A schematic of the components of the test board model.

6.1 Patch Cables

The connectors of the patch cables and test board are mated together. This makes it difficult to treat them separately. Therefore, the model of the patch cables will concern itself with the coaxial cable and the SMA connector to the TDR.

Instead of creating a 3D model of a coaxial cable in EMPro, a built-in ADS model was used. This model allowed for all parameters (radius of inner conductor, relative permittivity, etc.) of the cable to be specified. The only parameter that was not entered based on data values was the length of the cable. Due to the connectors, it is difficult to know where the patch cable starts and stops behaving as a coaxial cable, so assigning a length is difficult. Instead, the simulated length was adjusted until the TDR trace calculated from the model and calculated from the measured S-parameters matched. For the patch cable in figure 6.2, the measured length from the tip of one connector to the tip of the other was 304 mm versus a simulated length of 295 mm. Given that the connectors were around 10 mm each, this is a reasonable length. Another difference between the model and the cable was the inner conductor. The inner conductor of the cable consisted of 7 individual wires with a radius of 6.7 mil each, but the model did not allow for this. Instead the inner conductor was approximated by a single wire.

As seen in figure 6.2, there is also some reflection at the near-end of the cable due to the SMA connector. A small amount of reflection was added in ADS by using short ideal transmission line models. These were matched to the measured results. This addition may not be physical, but it will be eventually removed when the patch cable models are removed from the model.

The TDR trace of the model, shown in figure 6.2, is compared to a TDR trace calculated from extracted S-parameters. Both the TDR trace from the model and the measured S-parameters have a short 50 Ω transmission line in front of them creating a short, flat spot after the rise. Because the inner conductor of the cable is 7 wires, there was not a clear radius for the inner conductor for the model. The radius was adjusted until the impedance of the model matched the measurement. This required a radius of 20.55 mil.

Having the appropriate attenuation from the patch cables is important for the model. To test this, two ideal transmission lines were added to the far end of the patch cable to simulate the beginning of the test board connector. This was needed because if the cable is connected to a different impedance then the rise time will be

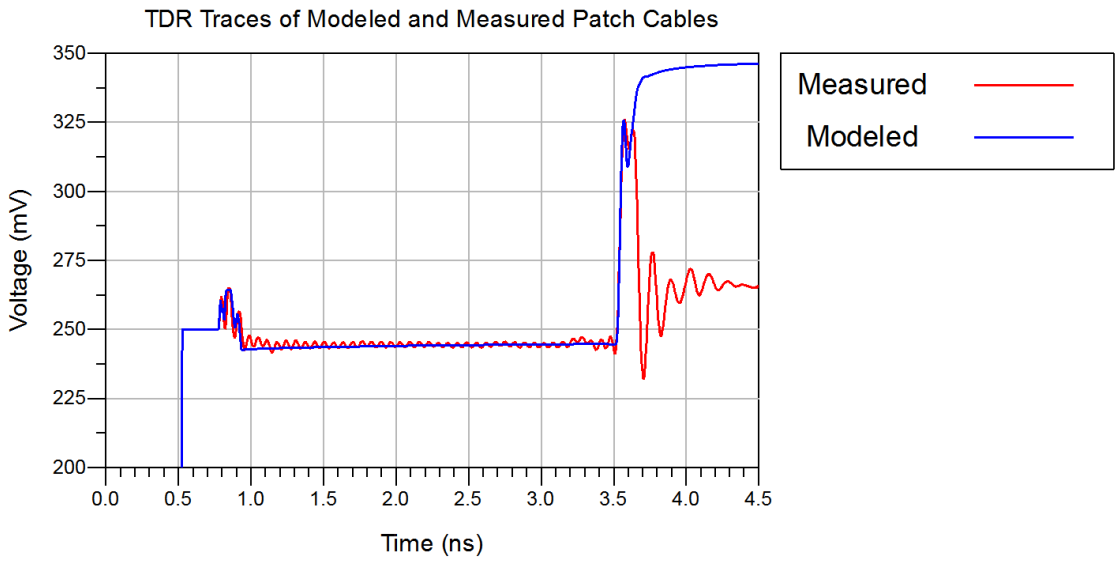

Figure 6.2: The TDR trace of the patch cable model with ideal transmission lines attached and the TDR trace of the test board and patch cables (calculated from measured S-parameters). The model and the calculation from the measurement have a short 50 Ω ideal transmission line added in front of them creating a short plateau.

Parameter	Nominal	Final Simulation
Inner Conductor Radius	7×6.7 *mil*	20.55 *mil*
Dielectric Outer Radius	60 *mil*	60 *mil*
Relative Permittivity (PTFE)	1.79	1.79
Loss Tangent (PTFE)	0.0002	0.005
Conductivity (Silver plated, copper clad steel)	$5.8 \times 10^7 S/m$ (Annealed copper)	$6.99 \times 10^6 S/m$

Table 6.1: Parameters of the coaxial cable model and the nominal values of the cable (1 mil = $1/1000^{\text{th}}$ of an inch or 25.4 μm).

different regardless of the attenuation of the cable. The impedance of these were adjusted to match the shape of the TDR trace. With nominal values the model had too fast a rise time at the connector. To compensate for this, the conductivity of the metal (copper) was reduced from $5.8 \times 10^7 S/m$ to $6.99 \times 10^6 S/m$ and the loss tangent was increased from 0.0002 to 0.005 (both needed to be increased to prevent the TDR trace of the cable from having a slope). After adjusting the impedance of the connector (again) to match the measurement, this produced a TDR trace with a similar rise time. See table 6.1 for the nominal and final parameters of the model.

6.2 Stripline Model

The stripline model consists two copper plates separated by FR4 with a copper trace placed asymmetrically between them as in figure 6.3. The thicknesses and widths of every component can be varied to simulate various geometries.

In a stripline, the top and bottom plates are both grounds, however, in EMPro the ports are only capable of connecting the signal line to one of the plates. In order to ground the other plates it must somehow be connected to the negative terminal of the port. Conveniently, this is similar to the test board geometry because the ground pin is soldered to the top plate of the printed circuit board. The connections from this ground plane to the others are handled by viae near the edge of the board. These viae can be approximated on the model by adding shorts (0 Ω connections) between the two plates.

Representing the actual locations of these viae would be difficult because they are

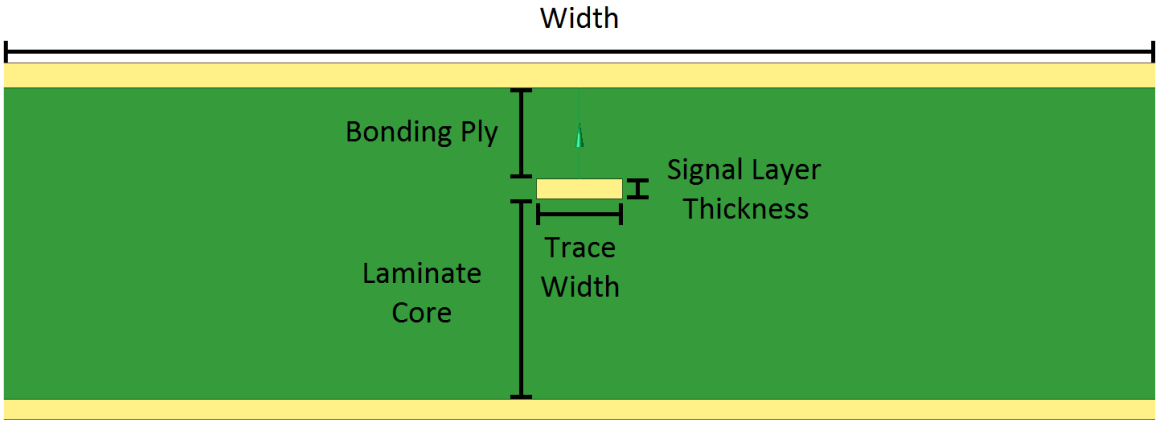

Figure 6.3: The cross section of the stripline model. The width of the model has been decreased in order to emphasize the dimensions of the trace of dielectric.

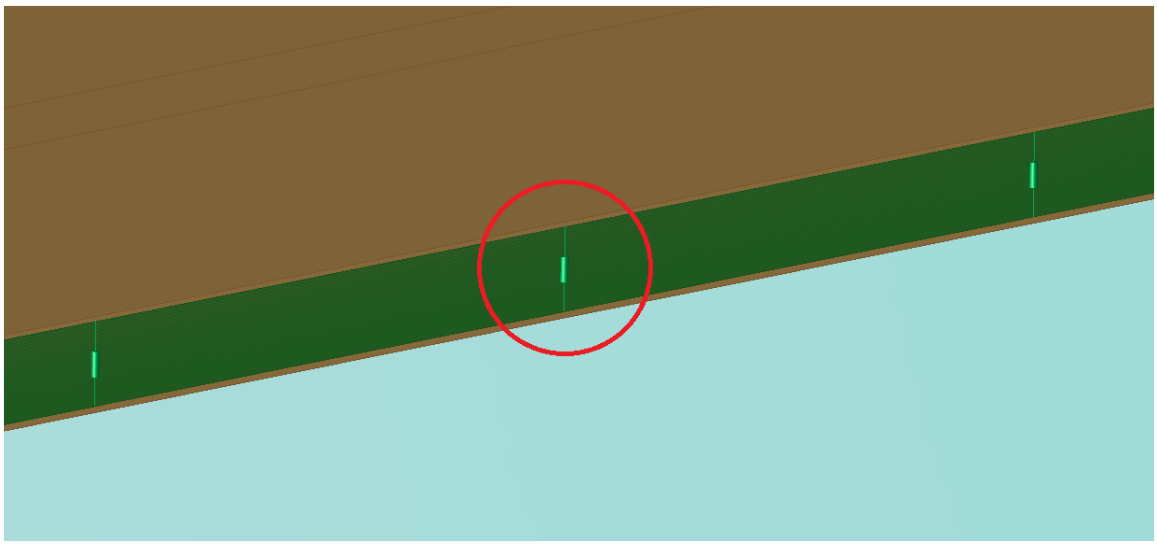

Figure 6.4: An image of the 3D model showing the shorts (as green lines) along the edge of the model.

a large distance from the signal line and would therefore require a large model that would take significant resources. Instead they were placed 5 mm apart along the edge of the model (see figure 6.4). The width of the model was kept at 10 mm for the simulations.

In order to allow the mesh on the ground plate to be coarse or fine depending on distance from the trace, the plate needed to be segmented into two areas, one near the trace and one far from the traces. By choosing initial maximum mesh sizes of 0.06 mm on the trace and ground plates near the trace and initial maximum mesh sizes of 1 mm on other components, simulations with a length of 100 mm (the length of the test board trace) can fit in the available computer memory.

The nominal values for the 6 mil trace are shown in table 6.2 and material values were: $\epsilon_r = 4.5$, $\tan\delta = 0.01$ and $\sigma_{copper} = 5.8 \times 10^7 S/m$.

With nominal values, the simulated impedance was found to be $\approx 50.4\ \Omega$, significantly below the measured impedance 56.8 Ω. For the test board, there are manufacturing tolerances listed for all dimensions except the trace width. By adjusting the dimensions of the stripline, the impedance was matched to the measured value while remaining within the tolerances for all but the trace width (see table 6.2 for dimensions). The trace width was reduced to 5.4 mil from 6 mil. A 0.6 mil tolerance (10%) for the trace width would be similar to that of other dimensions, such as the thickness of the trace.

Layer	Nominal Layer Thickness (mil)	Simulation Layer Thickness (mil)
Ground Layer	1.7 ± 0.4	1.7
Bonding ply	6.4 ± 0.7	7.1
Signal Layer	1.4 ± 0.4	1
Laminate Core	14 ± 2	16
Ground layer	1.4 ± 0.4	1.4

Table 6.2: The nominal layer thickness of the test board striplines and the thickness used for simulations that matched the measured impedance (Ground and signal layers are copper, bonding ply and laminate core are FR4) [34].

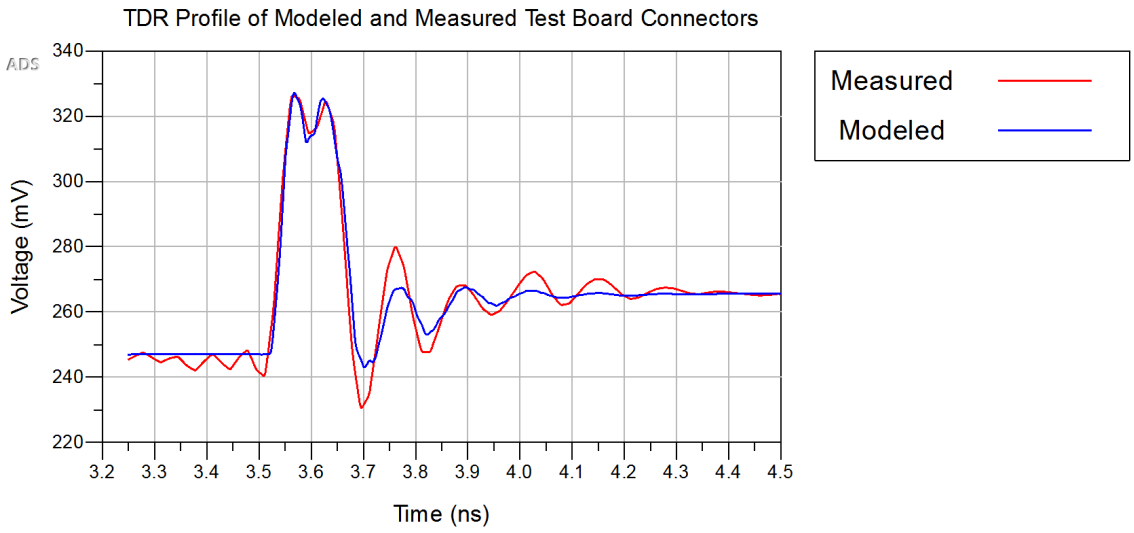

Figure 6.5: The TDR trace of the modeled and measured near end connector.

6.3 Connectors

Connectors on the test board and patch cables are sufficiently complicated (pads, pins, coaxial cable, splitting of the coaxial cable, etc.) that creating accurate 3D models for EMPro would be beyond the scope of this thesis. Instead, ADS was used to create models of the connectors using short lengths of ideal transmission line. This can allow for appropriate impedance but not resistance or conductance.

To make the model, transmission line components were added to the patch cable models and the S-parameter model of the stripline was added to that. The impedance, length and number of ideal transmission line components were varied so that the measured TDR trace and TDR trace of the model matched. The measured and model TDR traces were in good agreement when using 5 ideal transmission lines of 135, 70, 125, 50 and 25 Ω impedance. The result is shown in figure 6.5. This is used for the test board model.

The TDR trace of the model connector matches well with the measurement, but the ripples after the connector are supressed in the model. There is likely details of the connector that are difficult to image with our TDR that could enhance these ripples. The ripples, however, are at a much higher frequency ($\approx$ 7.35 GHz) than we are interested in (100 MHz max), so this can be ignored.

The connectors at the far end are the exact same, but with the order of the connectors inverted.

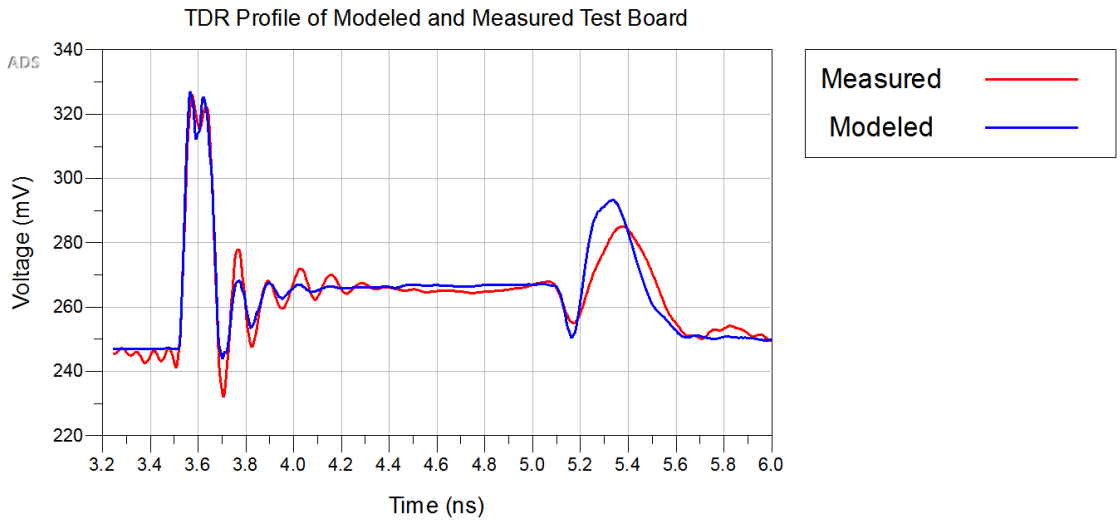

Figure 6.6: The TDR trace of the modeled and measured test board.

6.4 Results and Comparison with Measurements

Every component of the test board model can now be combined and compared with the measurements. The model TDR trace in figure 6.6 shows too much reflection at the far end connector, suggesting that there is too little attenuation present in the model. The model TDT trace in figure 6.7 has a similar shape to the measured trace, but the measured trace is smoother. Again this suggests that there is too little attenuation in the model.

There could be several sources for this. There may not be enough resistance and conductance on the patch cables, test board stripline and/or connectors. The patch cables were matched using the rise time of the connector, but the rise time is still slightly too fast. This cannot be the entire source of the attenuation because near end and far end connectors receive the same amount of attenuation from the patch cable. If more attenuation was added to the cables, then the impedance of the connectors would have to be increased so that the front end connector had sufficient reflection, which would add too much reflection to the far end connector. The most likely source is the connectors because they were modeled using ideal transmission lines, preventing them from attenuating the signal. For the prototype HEC baseplane connectors, more sophisticated models will be used.

The modeled and measured S-parameters are in good agreement. Figure 6.8 shows the magnitude and phase of reflection and transmission up to 2 GHz. The higher

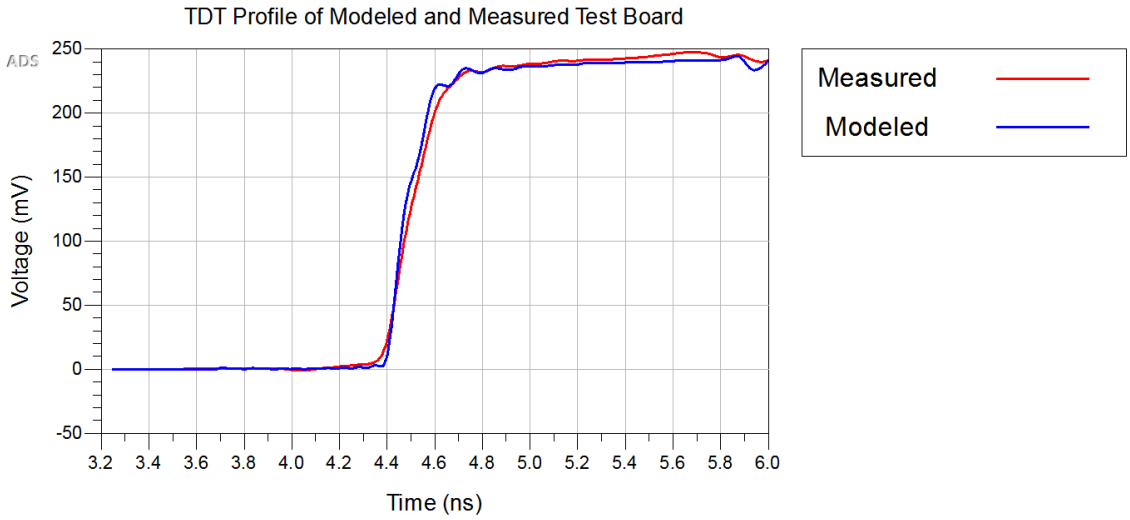

Figure 6.7: The TDT trace of the modeled and measured test board.

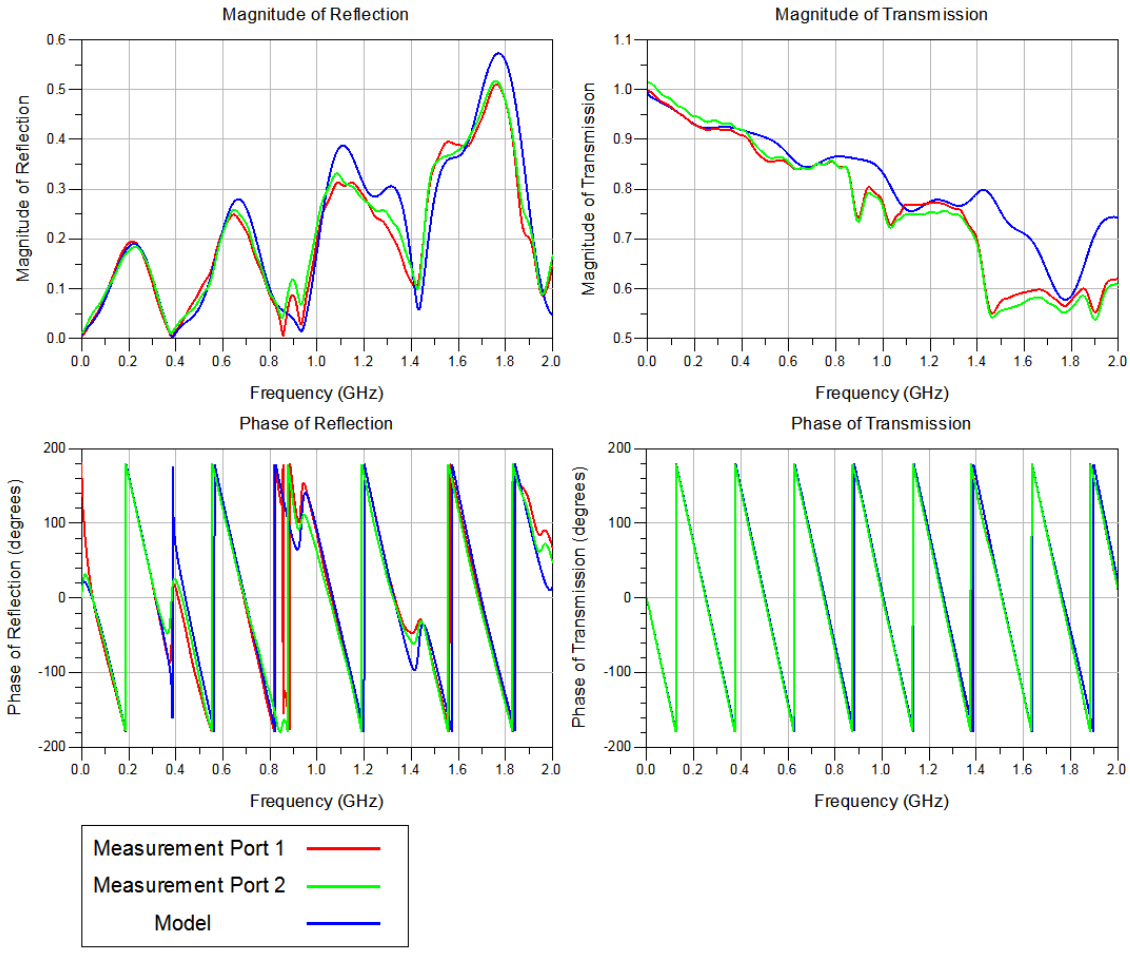

Figure 6.8: Modeled and measured S-parameters of the test board. Port 1 and 2 measurements are of the same test board stripline, but with either port 1 or 2 as the active port.

the frequency the more the model and measurement disagree, but at all frequencies the pattern of ripples is similar. This demonstrates some capacity of the model to represent the test board. There is too much transmission in the model at higher frequencies, again showing that more attenuation is needed in the model. This same lack of attenuation may also account for the excess of reflection seen in the model because this too could be attenuated.

Despite the symmetry in the test board there is a difference in measurements between the two ports of the board. Slight defects cause differences between the S-parameters for the two ports. To highlight this, the S-parameters have been shown for both port 1 and port 2 as the active port. Some error in the measurement is

still visible in the S-parameter. The transmission goes above 100% at 0 GHz for port 2 and the phase of the reflection goes to 180^o for port 1 and 0^o for port 2 as the frequency goes to zero. The latter can be a particularly difficult measurement for IConnect because the reflection goes to zero, where small errors cause large difference in the calculated phase.

Below 100 MHz there is very good agreement between measured and modeled S-parameters. In figure 6.9, the magnitude of reflection and transmission are only slightly below the measured values with less than 0.01 difference in transmission and reflection between the model and port 1 measurement (see figure 6.10). This is less than a one percent difference for transmission. For reflection the percent difference is significantly higher, reaching 90% near 5 MHz, however, the reflection is much smaller which exaggerates the percent difference.

There is one feature present in the measurements that is not present in the model. There are small ripples 50 MHz apart in the magnitude of measured reflection and transmission that are not there in the model. This is particularly visible at low frequencies in the magnitude of transmission for port 2 (see figure 6.11). This is not caused by reflection off connectors like in section 4.3 because the measurement system is not long enough for this frequency. However, the TDR measurements used by IConnect to calculate the S-parameters are only 20 ns long. A 10 ns long transmission line would take 20 ns for a transmission to transmit from the active end, reflect and return to the near end and, if it were not impedance matched, would create ripples in the S-parameters that are 50 MHz apart. These ripples are likely a side effect of a slight voltage offset that is making it appear as though there is a non-50 Ω transmission line for the entire measurement length. Indeed, if the measurement window length is changed, then the frequency between these ripples changes accordingly. These ripples are a non-physical effect from the measurement system.

Overall the test board model and measurements were in good agreement, validating these techniques for use on the prototype HEC baseplane.

6.5 Systematics

Several parameters of the stripline were varied. Placing viae closer together affected the derived S-parameters at frequencies above 2 GHz, but caused no change in the 0 to 100 MHz range. Similarly, increasing the simulated width beyond 10mm, changing boundary condition and increasing the amount of padding only affected the S-

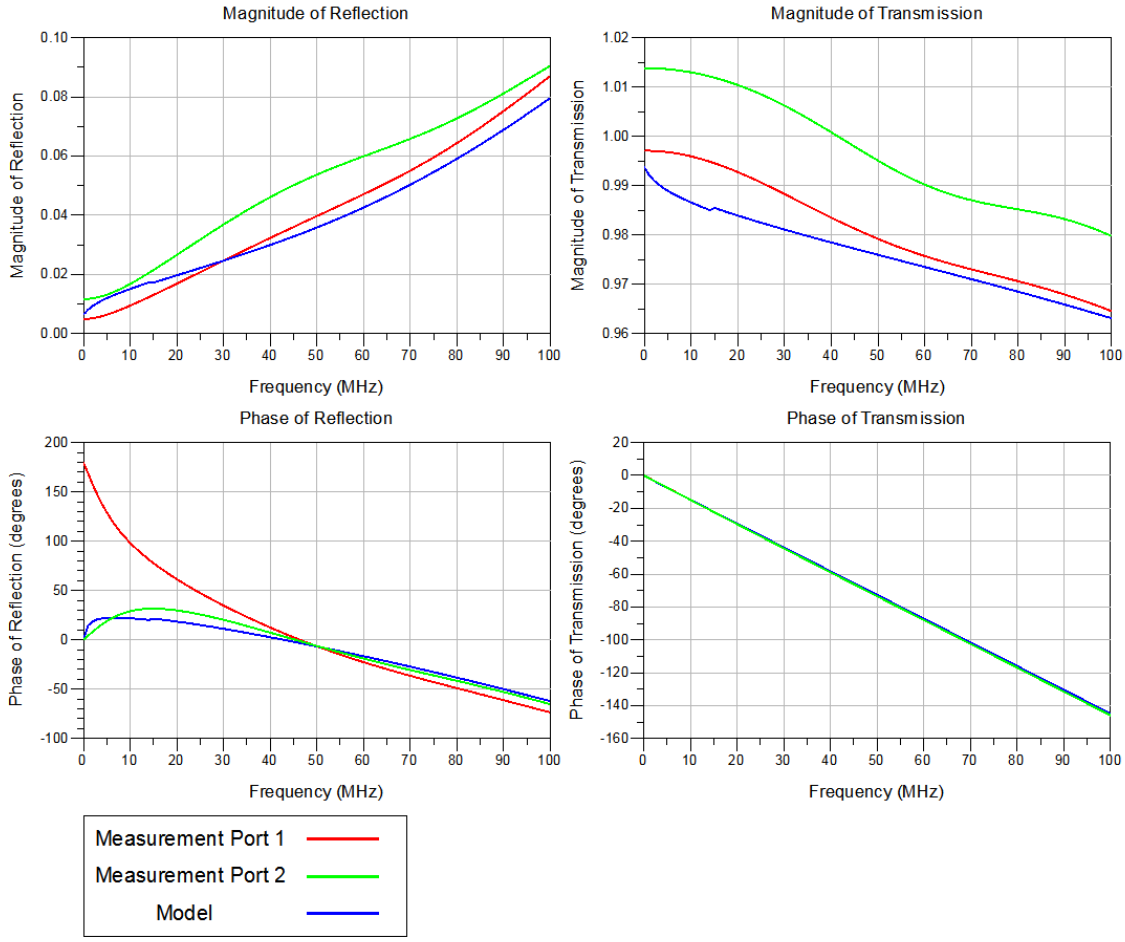

Figure 6.9: Modeled and measured S-parameters of the test board. Port 1 and 2 measurements are of the same test board stripline, but with either port 1 or 2 as the active port.

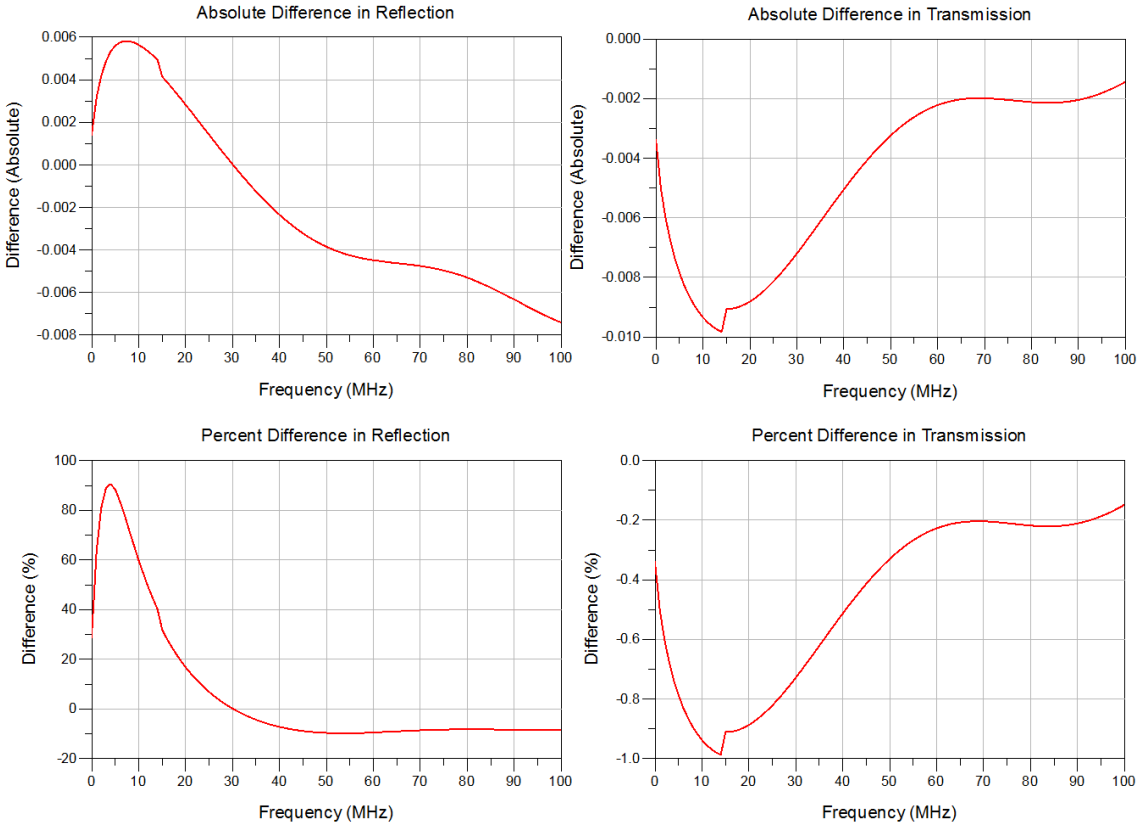

Figure 6.10: Difference between modeled and port 1 measurement of reflection and transmission

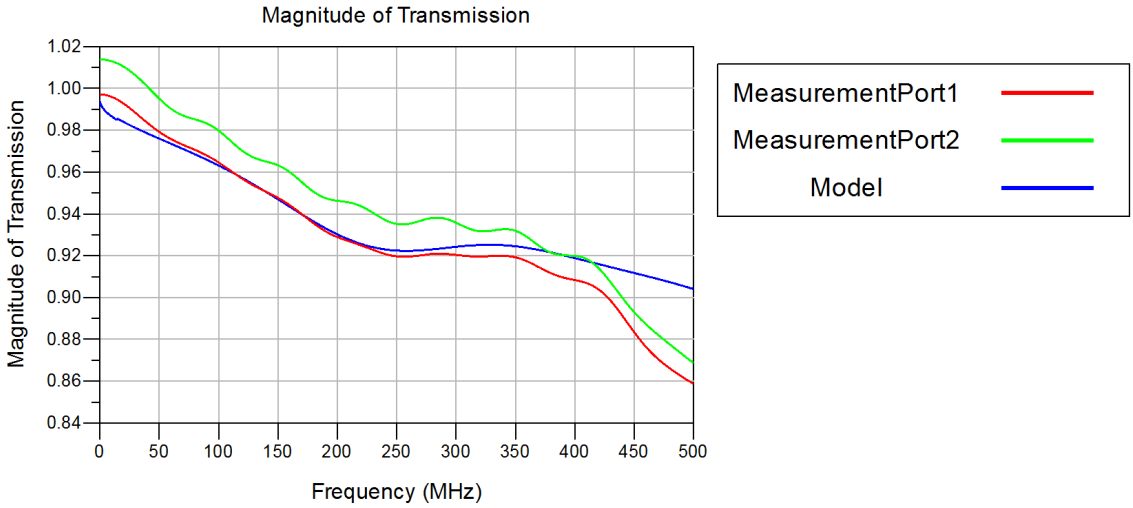

Figure 6.11: Modeled and measured transmission of the test board. Port 1 and 2 measurements are of the same test board stripline, but with either port 1 or 2 as the active port. There are ripples 50 MHz apart in the measurements that are not visible in the model S-parameters.

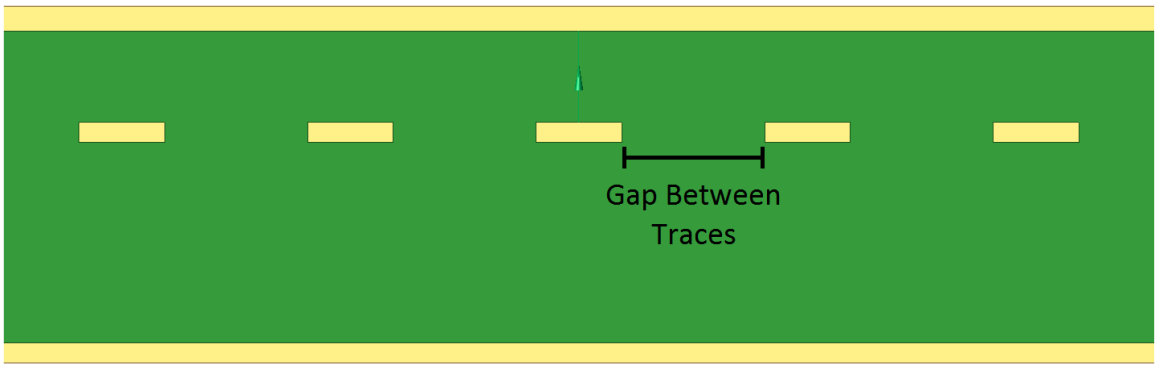

Figure 6.12: The cross section of the stripline model with five parallel traces.

parameters at high frequencies (above 2 GHz) and not in 0 to 100MHz range.

Trapezoidal traces were also investigated. The etching process for creating printed circuit boards does not produce perfectly square trace cross sections. Instead, during the etching process, once the sides of the trace are exposed, the etchant will begin to dissolve the sides of the trace leaving a trace that is approximately trapezoidal rather than rectangular [41, 42]. Making traces trapezoidal in simulations did increase impedance, but this can be accomplished through adjusting other stripline parameters (such as trace width). Trapezoidal traces can impact crosstalk, but crosstalk was not investigated for the test board traces. For these reasons trapezoidal traces were not used in the model.

In the test board there are nearby traces, however, we were only interested in one traces. To make simulations more simplistic it is convenient to ignore traces that are not being measured, but these traces could affect the characteristics of the traces being measured. In order to test the sensitivity of traces to nearby lines, a model was created of five parallel stripline traces (see figure 6.12). Traces were then switched between copper and dielectric to test the impact of ignoring traces. For the 6 mil test board traces (nominal geometry) with 6 mil gaps between traces the presence of a neighbouring traces increased the characteristic impedance from 53.73 Ω to 53.91 Ω. This is a small affect and was ignored.

Chapter 7

Prototype Hadronic Endcap Baseplane Model and Measurements

The previous chapter demonstrated we could successfully model printed circuit boards. In this chapter the same techniques will be applied to model two pairs of interconnects on the prototype HEC baseplane. A set of interconnects will be chosen for modeling and measurement, then the model will be developed and, finally, the model will be compared with measurements. Again, the model will contain the patch cables and will be compared to measurements of the patch cables and prototype baseplane.

7.1 Interconnects of Interest

Though every interconnect on the final HEC baseplane will be measured, it is not necessary to do this for the prototype board. Instead, two pairs of interconnects have been selected for modeling. The first pair are two neighbouring interconnects, as highlighted in figure 7.1, that have striplines that are short and comparably straight. They do not go through via fields and have few bends. This pair was selected because it is the most simple interconnect on the prototype HEC baseplane and should be the easiest to model. The second pair, however, was the most complicated interconnect on the board (see figure 7.2). The striplines are long, turn several times and run through the via field of a LTDB connector twice, potentially adding more reflection or crosstalk. It is likely that if the model works for this more complicated stripline,

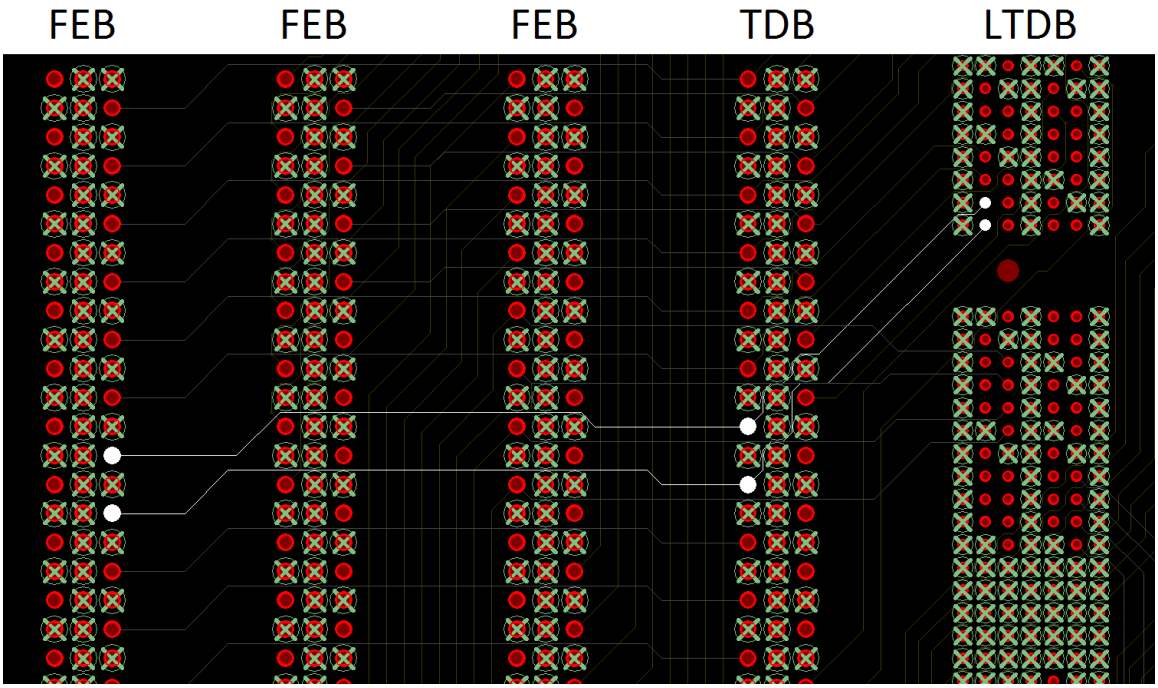

Figure 7.1: The pair of simple interconnects on the HEC prototype baseplane (CH2 44 and CH2 45 in design files). The daughter board for the connectors are labeled at the top.

then it will for all other striplines, which should have fewer perturbations from an ideal stripline. The interconnect pairs will be referred to as the simple and complicated interconnects, respectively.

There are two types of interconnects on the prototype HEC baseplane, those where the interconnect splits at the FEB and those where the interconnect splits at the TDB. Both the simple and complicated interconnects split at the TDB, however, since the TDB and FEB connectors are identical, measuring transmission/reflection from the TDB is equivalent to measuring transmission/reflection from the FEB for interconnects that are split at the FEB.

7.2 Patch Cables

In order to measure interconnects on the HEC prototype baseplane special connectors were needed. The two-pin connectors used for the test board could not be connected to neighbouring pairs of pins on the ERNI connectors because the two-pin connector is too big for the space between pins of the ERNI connector. Furthermore, not

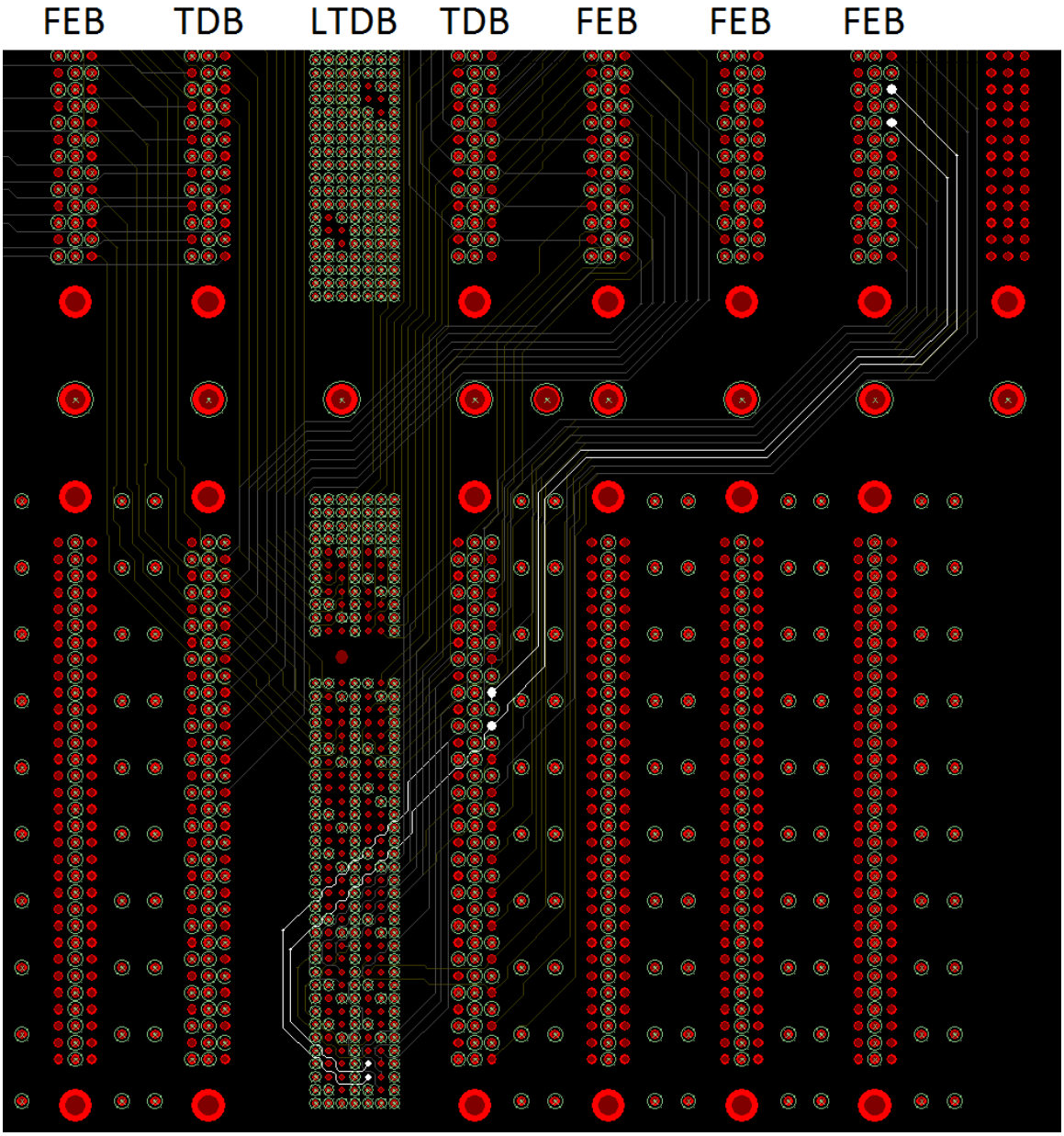

Figure 7.2: The pair of complicated interconnects on the HEC prototype baseplane (CH1 04 and CH1 05 in design files). The daughter board for the connectors are labeled at the top. Both the top and bottom connector in each column are for the same board.

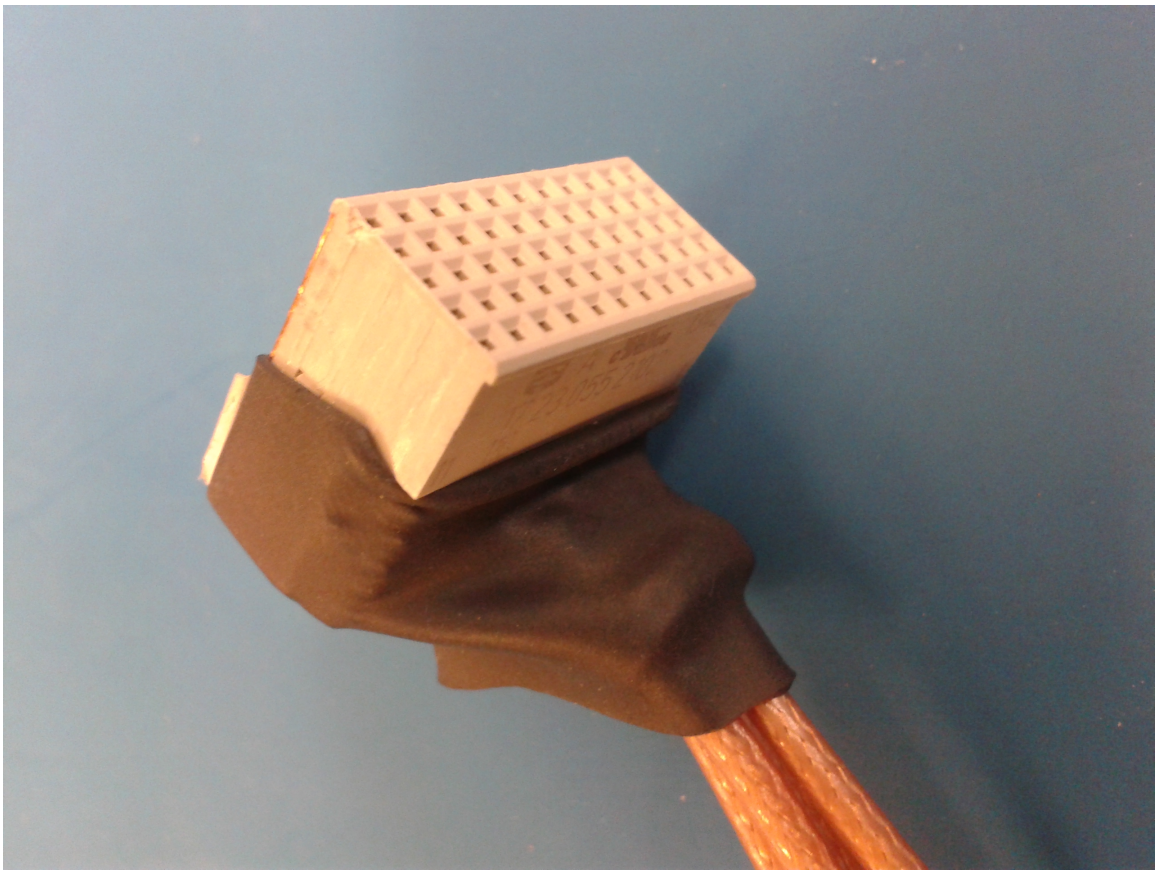

Figure 7.3: A picture of the patch cable for the LDTB.

connecting all the ground pins surrounding the signal pins of the ERNI and FCI connectors could significantly alter the reflection and transmission of the connectors, making the measurements a poor representation of baseplane to LTDB, FEB and TDB connections.

New patch cables were made using small (fewer pins than the connectors on the prototype HEC baseplane) female connectors with coaxial cables soldered on to them (see figures 7.3 and 7.4). The inner conductors of each cable was soldered to a signal pin and the outer conductors were soldered to the ground pins. This design allowed neighbouring signal pins to be simultaneously connected to the TDR and for appropriate grounding/shielding. A different LTDB patch cable was needed for each set of interconnects measured because of variation in signal and ground pin assignment for the LTDB connectors. For the FEB and TDB, identical signal and ground pin assignment was used, allowing for one patch connector design for all measurements.

For the LTDB connector a short version of the female connector on the LTDB

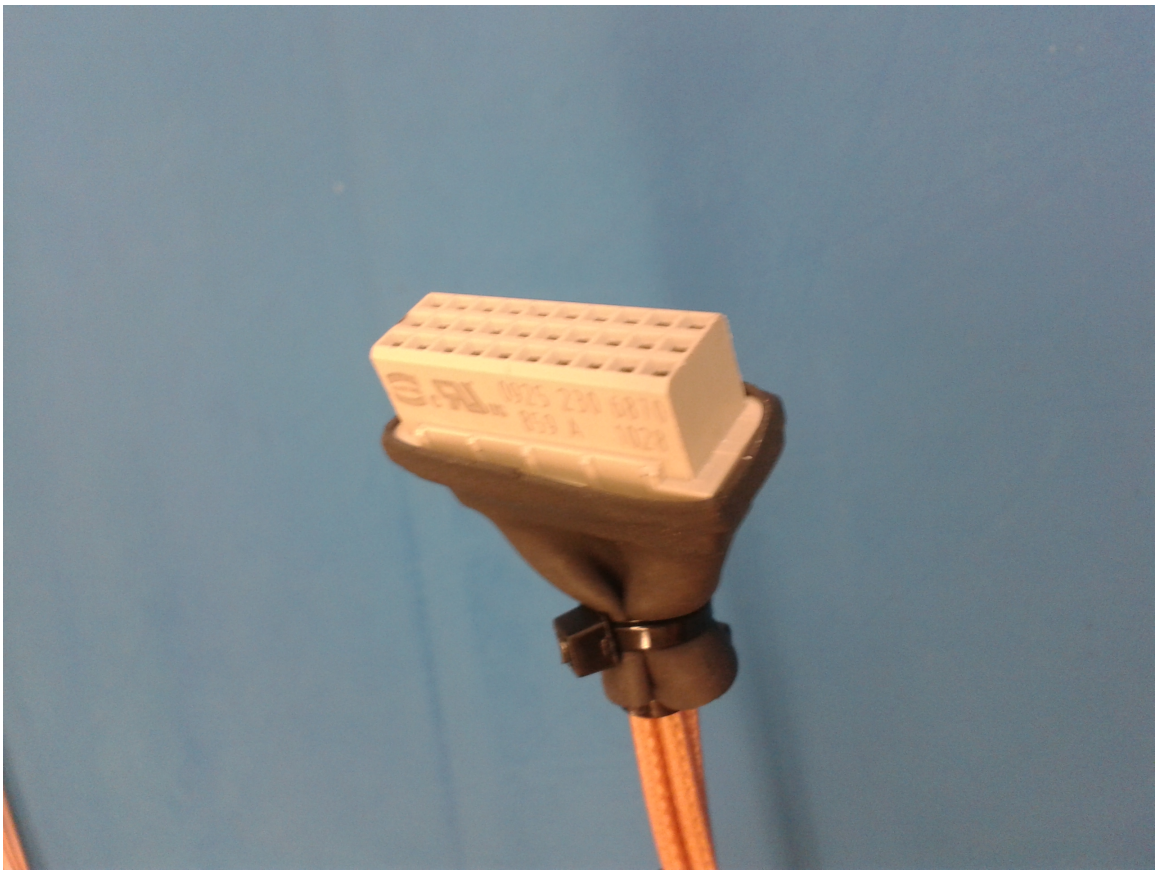

Figure 7.4: A picture of the patch cable for the FEB and TDB.

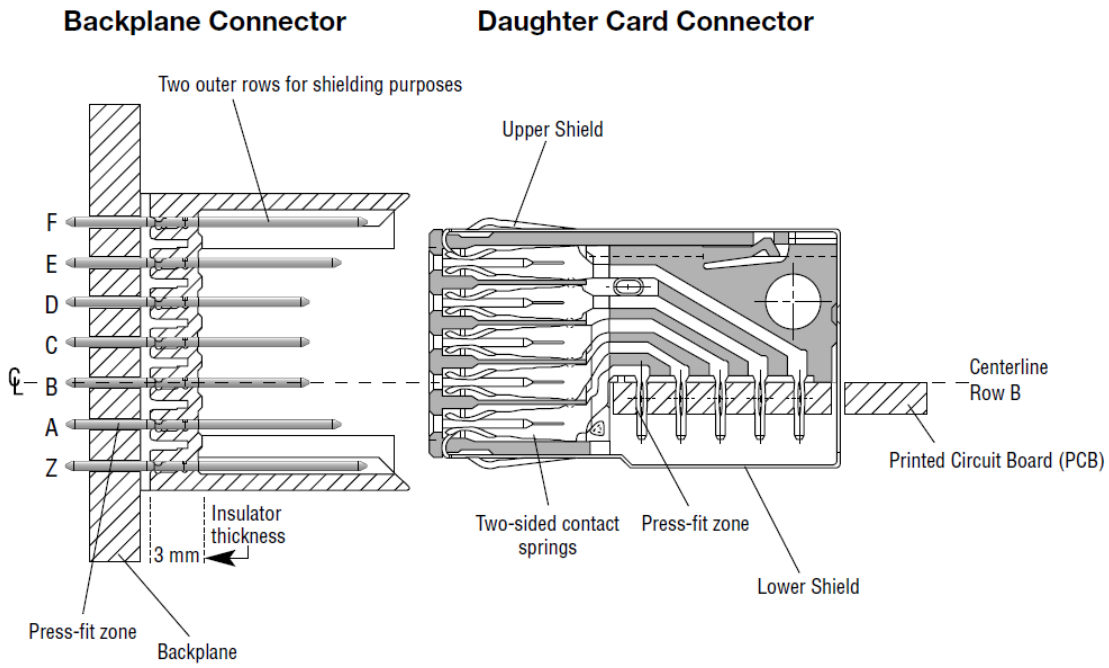

Figure 7.5: A diagram of the ERNI press-fit connectors showing male (backplane) and female (daughter card) connectors [43, p. 148]. Our connectors do not have the lower shield that is shown in the diagram.

was used (ERNI part no. 064198). The connector has a 90° bend (see figure 7.5 for a cross section of both the male and female ERNI connectors). This causes each row of pins to have a different path length through the connector.

The female connectors that are used on the actual FEB and TDB boards were not used for the patch cables. Instead a straight press-fit connector (Harting Connectors part no. 09252306870) was used. Using a different connector could alter the amount of reflection and transmission (including crosstalk), however, even if the correct female connector were used, soldering cables to them would create an interface that is different from imbedding the connectors in a printed circuit board, so results would not be identical. Still, results should not under estimate the amount crosstalk or distortion that occurs during transmission from one male baseplane connector to another because the correct connectors are present on the baseplane.

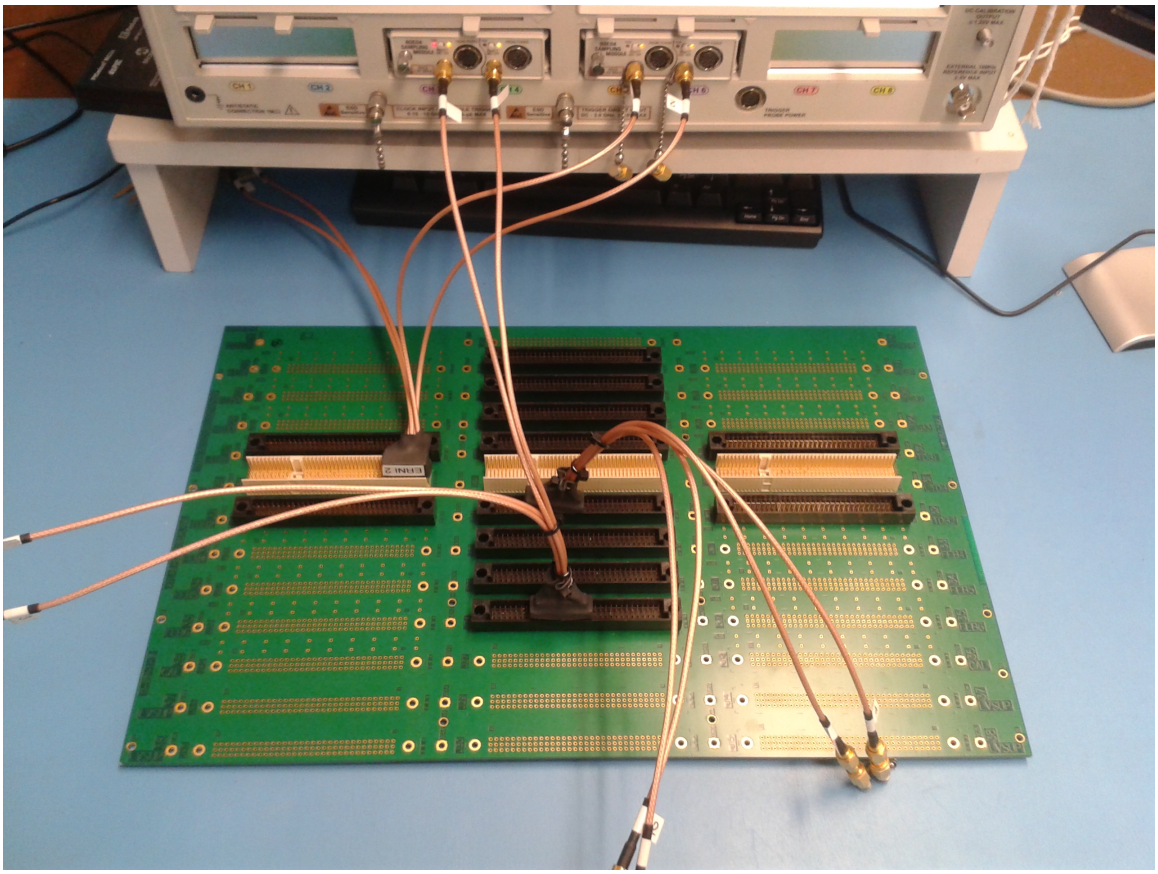

Figure 7.6: A picture the prototype HEC baseplane connected to the TDR for measurements. 50 Ω terminators are on the patch cables not connected to the TDR.

7.3 Measurements

Three types of measurements were taken for each of the interconnects of interest, i.e. two pair. IConnect cannot extract S-parameters from 3 port systems (only 2 port transmission lines, and coupled transmission lines with two ports each) so measurements were done in pairs of active connectors (FEB and TDB, FEB and LDTB and TDB and LTDB). For the connector that was not active, the patch cables were left in place, but were terminated into 50 Ω SMA terminators. Figure 7.6 shows the prototype HEC baseplane connected to the time domain reflectometer for measurements.

Compared to the test boards, the length of the measurement window was increased. This has decreased the frequency of the non-physical ripples discussed in chapter 6. When the ripples in the S-parameters are longer, they cause a large difference in 100 MHz range. Figure 7.7 shows measured reflection (S_{11}) using a 500

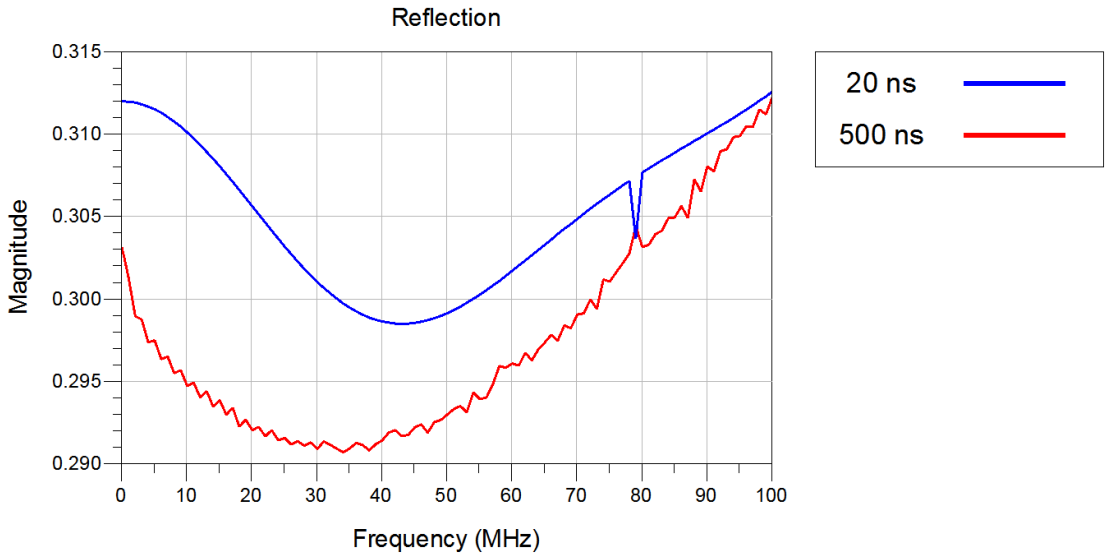

Figure 7.7: Reflection (magnitude of S_{11}) measured using 20 ns and 500 ns measurement windows. The S-parameters measured using the 500 ns measurement window have high frequency ripples. The S-parameters measured using the 20 ns measurement window have long ripples causing the difference between the reflection in the 500 ns and 20 ns measurements. Note, there is a sudden drop at 79 MHz for the 20 ns measurement. This is a measurement error and should be ignored.

ns measurement window and the 20 ns measurement window. The ripples for 500 ns sampling window are visible in the S-parameters in the 0 to 100 MHz range. The ripples caused by the 20 ns measurement window are longer, larger (not easily recognized as ripples in this frequency band) and causing a significant difference in the 0 to 100 MHz range.

For each variation of active connectors, and for the simple and complicated interconnects, S-parameters were measured. These measurements were repeated on the second prototype board. Between each identical measurement, at least one day passed, the modules were deskewed and 50 Ω terminators and FCI connector patch cables were chosen randomly. In this way, the S-parameters give a good estimate of the variability of the measurements and some estimate of the variability in the manufacturing process. The only difference between S-parameter measurements was the amplitude of the non-physical ripples. This may have been caused by differences in voltage between TDR channels that were several mV. Because there was little change in S-parameters (negligible compare to differences with model) only a single measurement will be shown.

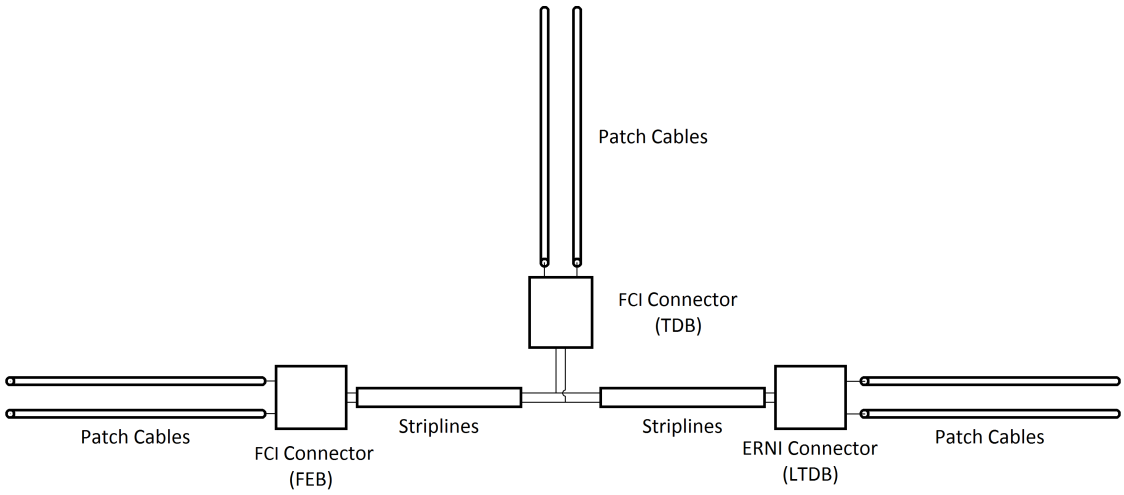

Figure 7.8: A schematic of the components of the prototype HEC baseplane model. The SMA connectors to the TDR are not shown.

7.4 Model

The model consists of three components: patch cables, connectors and stripline transmission lines. Similar to the test board, each component will be modeled and assembled as shown in figure 7.8. The coaxial cable for the prototype HEC baseplane and the test board patch cables were identical, so the coaxial cable model used for the test board was reused. The only change was adjusting the length for the particular cable used. The striplines were modeled in the same way as in chapter 6, but with a second stripline added to the model and the dimensions adjusted. A new model was created for the connectors because ideal transmission lines cannot be used to simulate crosstalk. The details of striplines and connectors are discussed below.

7.4.1 Stripline Parameters

The exact geometry of the striplines in the prototype baseplane is unknown because there is variability introduced by the manufacturing process. Schematics were created that specify the geometry based on what the design software calculated to produce 50 Ω transmission lines. Rather than use this geometry, the manufacturer instead used geometry they believed would produce 50 Ω transmission lines with their material and manufacturing process. Because of this, it is not known what the actual geometry of the board is, but it is expected that the geometry is similar to values in the design file.

Layer	Layer Thickness (mil)
Ground Layer	0.67
Dielectric	7
Signal Layer	0.67
Dielectric	7
Ground layer	0.67

Table 7.1: Dimensions of prototype HEC baseplane striplines. The dielectric is FR4 with $\epsilon_r = 4.5$ and $\tan\delta = 0.01$.

For the simulation, the nominal values were used for most geometries, but the width of the trace was adjusted to match 50 Ω. This required a width of 5.5 mil versus the width of 5.32 mil specified in the design file. Table 7.1 displays the geometry listed in the design file. The lengths were taken from the design file. The simulation was set to the shorter of the two stripline and ideal transmission lines were added to increase the length of the longer stripline.

Many aspects of the striplines were ignored. Bends were expected to have little impact at low frequencies so all striplines were approximated as straight. Furthermore, the way neighbouring striplines were routed caused the distance between them to change. Luckily, since the striplines are fairly far apart, there is little crosstalk between them and changes in distance should have little impact. For the model, an approximate separation was chosen for each segment of the stripline (e.g. from the TDB to the LTDB).

Trapezoidal trace profiles and neighbouring traces were ignored. The separation distance between traces was large enough that other traces did not impact the impedance of the active trace. Similarly, any impact of trapezoidal traces on crosstalk would be negligible compared to the crosstalk from the connectors.

7.4.2 Connectors

The connectors are responsible for large amounts of reflection and are the source of most of the crosstalk in the prototype HEC baseplane. A SPICE model[1] of the mated ERNI (LTDB) connectors was available from the manufacturer, but was found to be insufficient for modeling these connectors (too little impedance, resistance and

[1] A common electronic file format for describing the electrical response of devices. Most electronic design and simulation software can import SPICE models and many manufacturers provide SPICE models for electronic components.

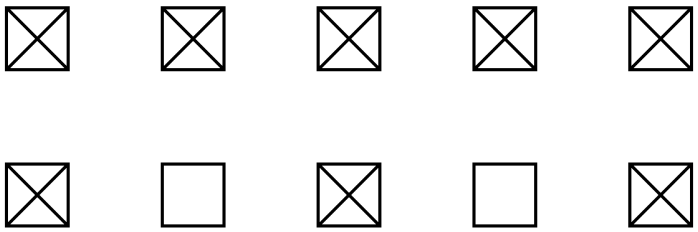

Figure 7.9: The cross section of the FCI connector model. The ground pins are marked with x's.

crosstalk).

The geometry of ERNI and FCI connectors is complicated with internal bends (ERNI only), varying conductor dimension (width, thickness) and conductors varying in length for different rows (ERNI only, see figure 7.5 on page 91), making an accurate 3D model would be beyond the scope of this thesis. The FCI (FEB and TDB) connectors vary in pin cross section, but are straight.

A simple model was used for the ERNI and FCI connectors. The connectors were assumed to be straight, rectangular, parallel pins of constant cross section of their measured length. These were simulated using ADS's multilayer transmission line model, which allows for multiple layers of square conductors. The dielectric constant of the material surrounding the pins was adjusted so that the model and measured TDR traces of the connectors were the same length. The geometry of the pins for the ERNI and FCI connectors were then both adjusted to match the TDR/T traces

The FCI connector model was comprised of two rows of five pins set $1/10^{th}$ of an inch apart with one row being ground and the second line alternating between ground and signal pins (see cross section in figure 7.9). The length was set to 26 mm and the relative permittivity to 2.5. The pins are 1.0 mm by 1.0 mm. There was a large drop in the TDR trace just after the connector. To model this, a short ideal transmission line was added in parallel to the stripline and left unterminated in order to lower the impedance.

The ERNI connector model consisted of three rows of 4 pins with the central two being signal lines and all others being ground (see cross section in figure 7.10). Along the rows the pins were 2 mm apart and the rows were 1.8 mm apart. This was done because the conductors inside the female portion of the connector turn 90°. During this turn the conductors are closer together in one direction. The length was set to 32 mm and the relative permittivity to 2.0. The dimensions of the pins were 0.25 mm

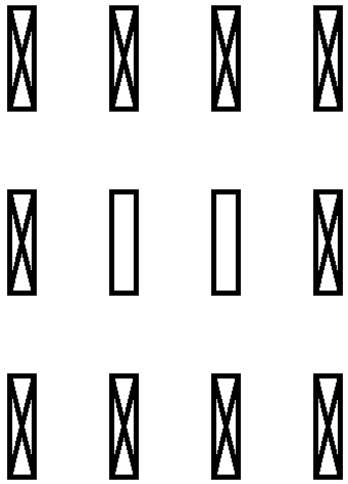

Figure 7.10: The cross section of the ERNI connector model. The ground pins are marked with x's.

(in the row directions) by 1.0 mm (in the column direction).

The ERNI connector model was matched to the measurements of the simple interconnects. However, the complicated interconnects use a different row of pins (row E for simple interconnects and row B for complicated interconnects as shown in figure 7.5 on page 91). This row has a shorter conductor inside the female ERNI connector. Therefore, the model of the ERNI connectors for the complicated interconnects was shortened to the length for this row, 24 mm.

7.5 Comparison with Measurements

Figures 7.11 and 7.12 show the time domain reflection, transmission, backward crosstalk and forward crosstalk for the simple interconnects with LTDB (ERNI connector) first and the FEB (FCI connector) first with the TDB terminated into 50 Ω. The reflections from the connectors are more complicated than what is present in the model. There is too much forward crosstalk and not enough backward crosstalk, but the correct shape is present.

Figures 7.13 through 7.20 show the magnitude and phase of the model and measured S-parameters for FEB to TDB, FEB to LDTB, TDB to FEB and TDB to LTDB transmission. For each situation the unused port is terminated into a 50 Ω

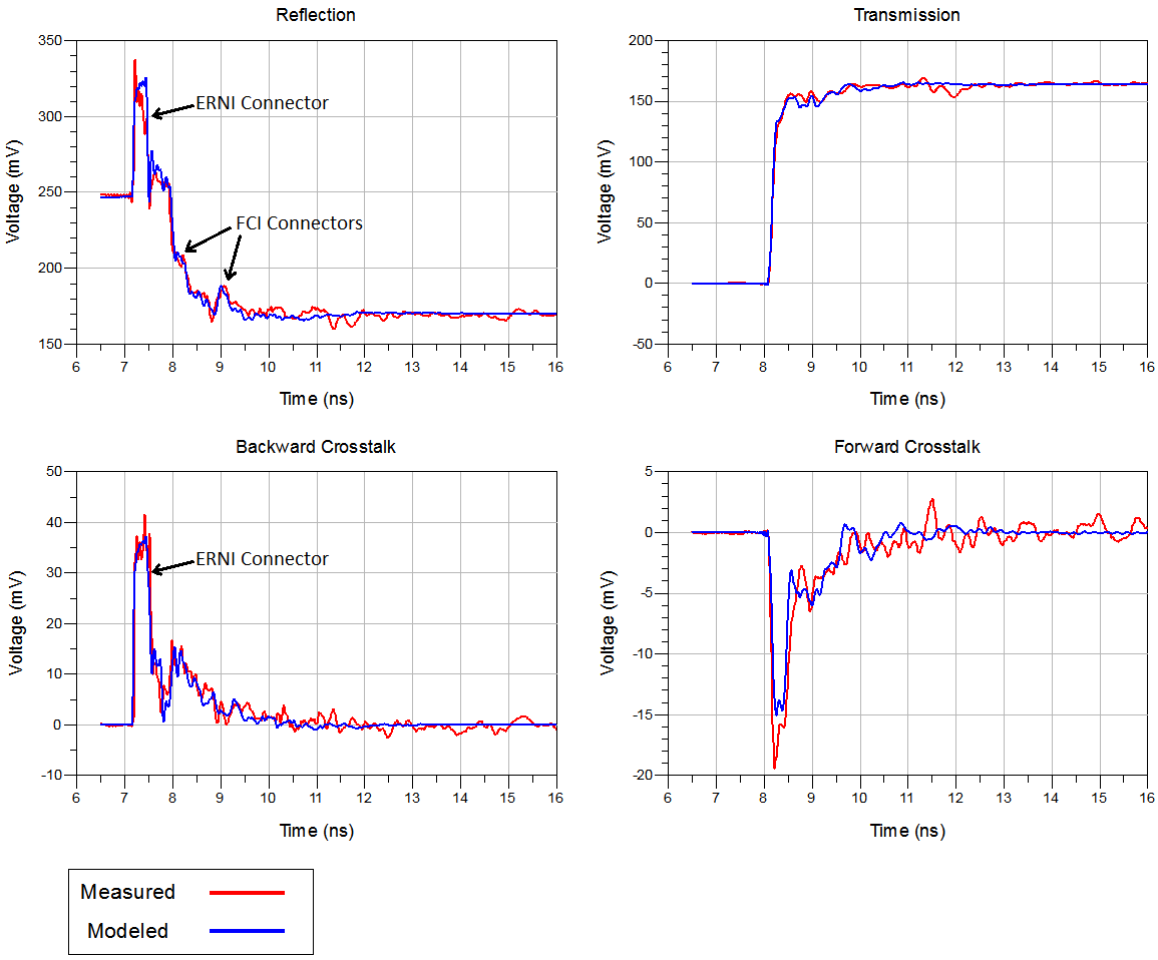

Figure 7.11: Model and measured TDR/T traces of the simple interconnects of prototype HEC baseplane for LTDB to FEB transmission showing reflection, transmission, forward crosstalk and backward crosstalk. The splitting of the interconnect causes the large inverted reflection seen $\approx$ 8 ns. This is because the parallel 50 Ω routes look like 25 Ω to the incoming wave. Note, the y-axis of some graphs does not start at zero in order to emphasize the observed features.

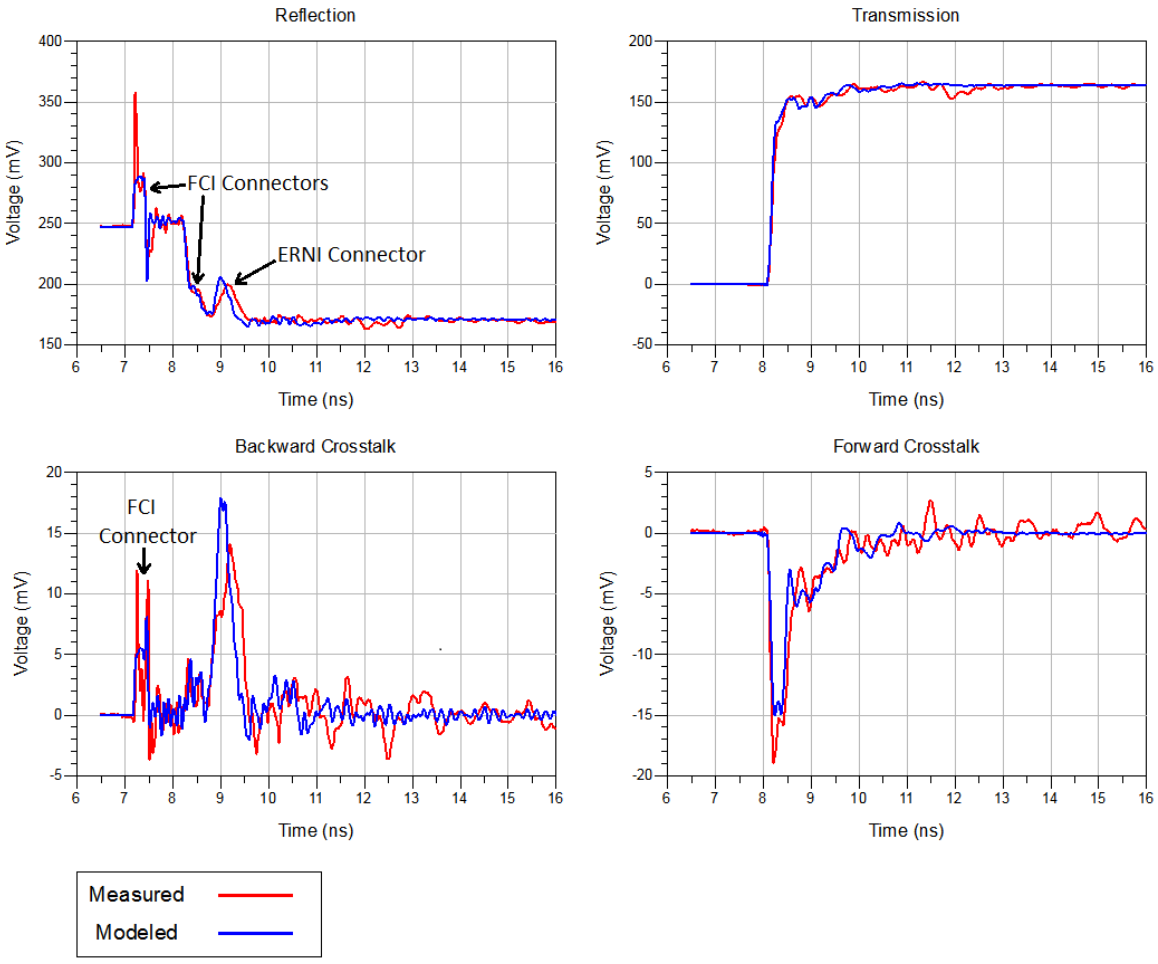

Figure 7.12: Model and measured TDR/T traces of the simple interconnects of prototype HEC baseplane for FEB to LTDB transmission showing reflection, transmission, forward crosstalk and backward crosstalk. The splitting of the interconnect causes the large inverted reflection seen ≈ 8.25 ns. This is because the parallel 50 Ω routes look like 25 Ω to the incoming wave. Note, the y-axis of some graphs does not start at zero in order to emphasize the observed features.

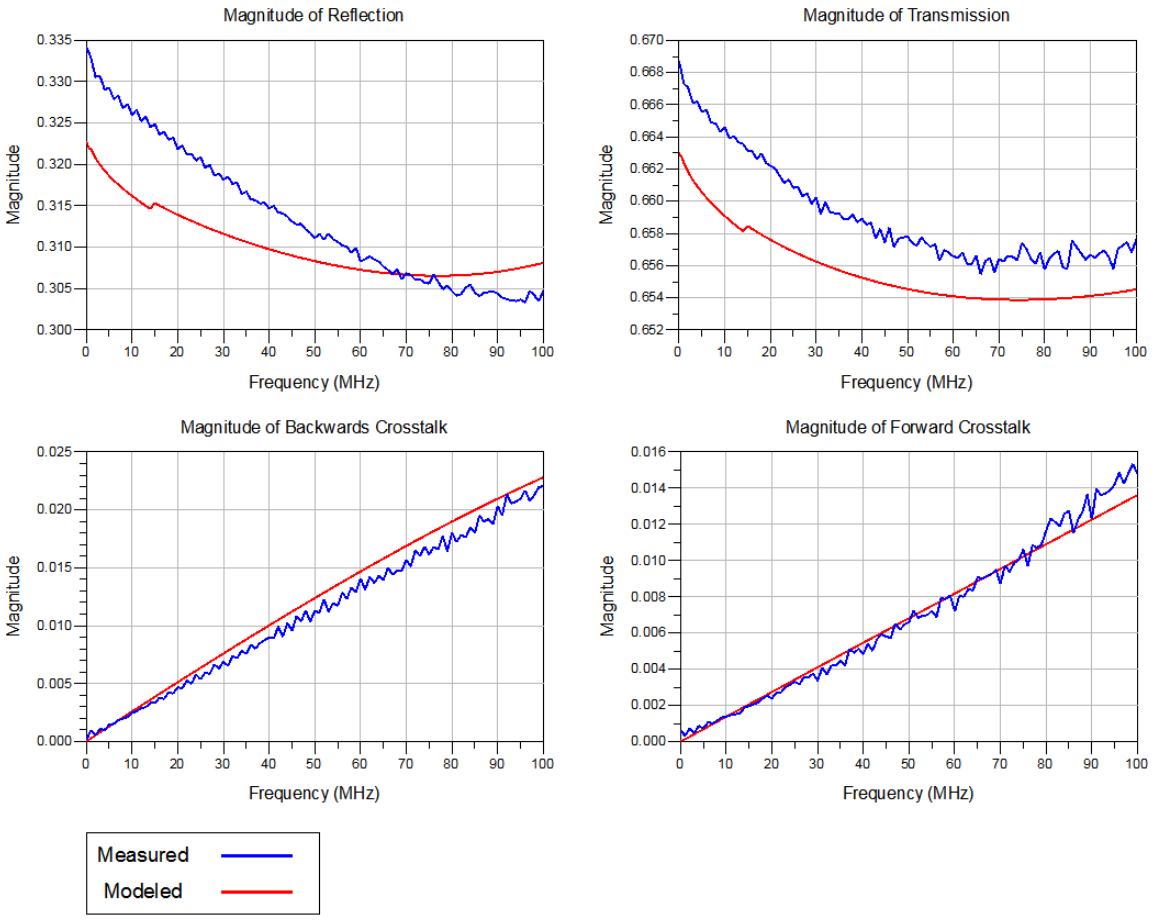

Figure 7.13: Magnitude of the measured S-parameters and the S-parameters of the model for FEB to TDB transmission for the simple interconnects. Note, the y-axis of some graphs does not start at zero in order to emphasize the observed features.

terminator. Figures 7.22 through 7.24 show the percent difference[2] for the magnitude of the model and measured S-parameters.

The magnitude of the transmission and reflection of the model and measurement are always less than 0.02 apart and are always within 5%. The magnitude of the forward and the backward crosstalk of the model and measurement are always within 0.01, but the amount of crosstalk is small compared to reflection and transmission, making the percent difference much larger than for reflection or transmission. This is greatly exaggerated at low frequency where the crosstalk approaches zero. The effects

[2]

$$\text{Percent Difference} = \frac{S_{ii\text{Model}} - S_{ii\text{Meas}}}{S_{ii\text{Meas}}} \times 100\% \tag{7.1}$$

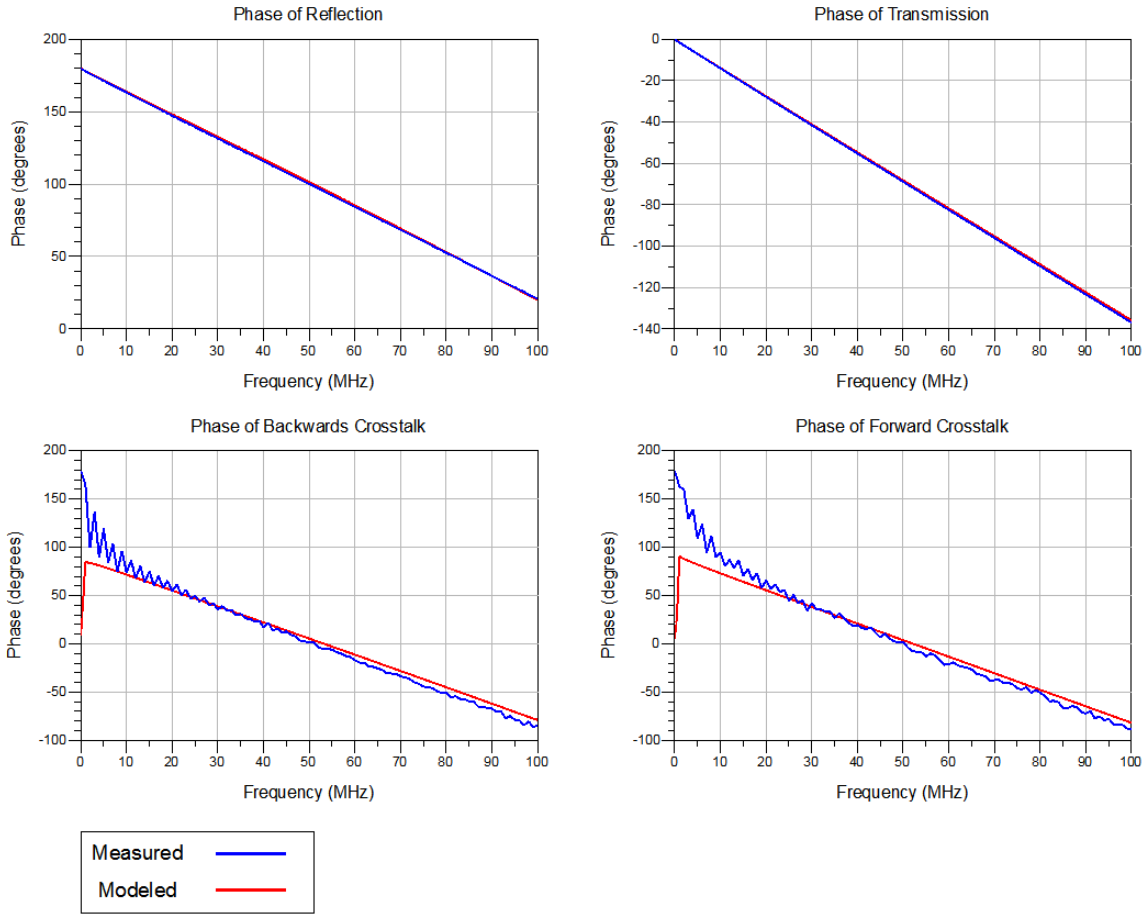

Figure 7.14: Phase of the measured S-parameters and the S-parameters of the model for FEB to TDB transmission for the simple interconnects.

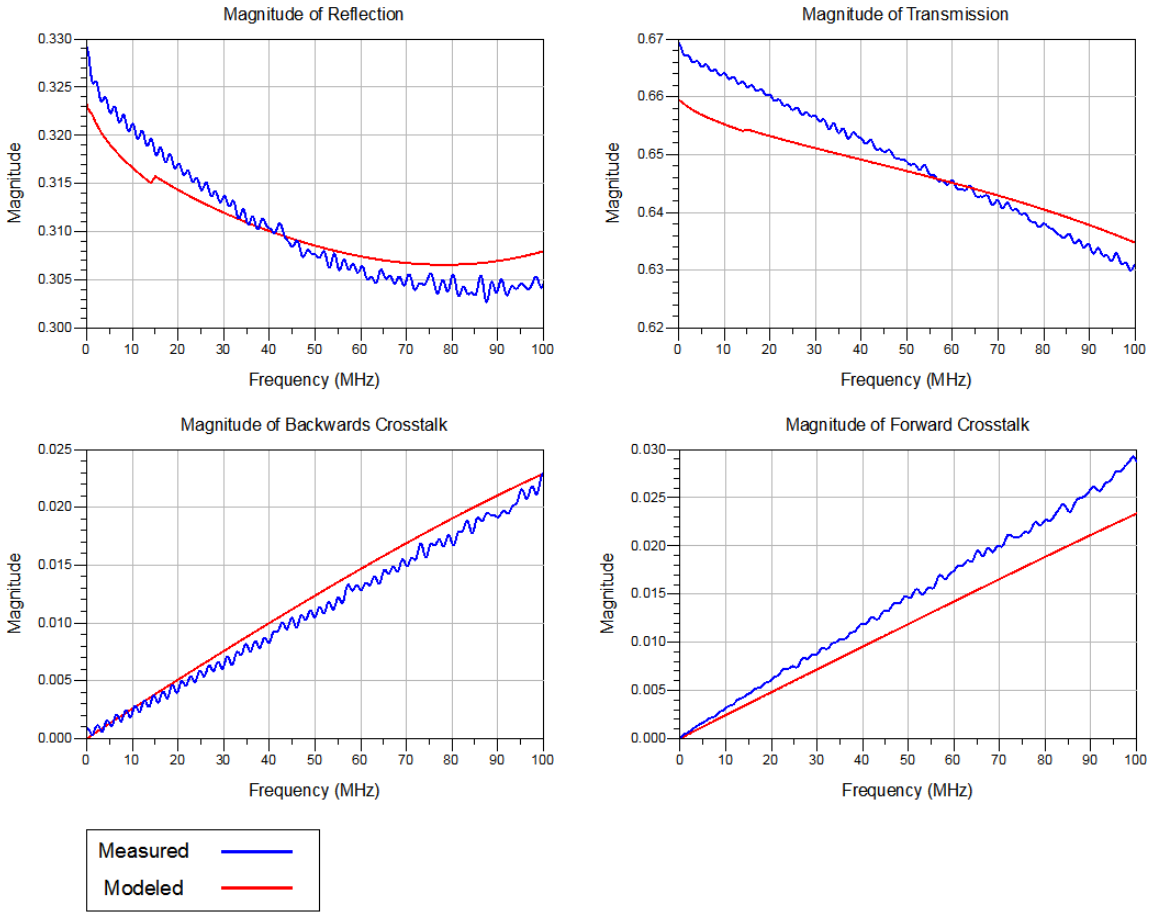

Figure 7.15: Magnitude of the measured S-parameters and the S-parameters of the model for FEB to LTDB transmission for the simple interconnects. Note, the y-axis of some graphs does not start at zero in order to emphasize the observed features.

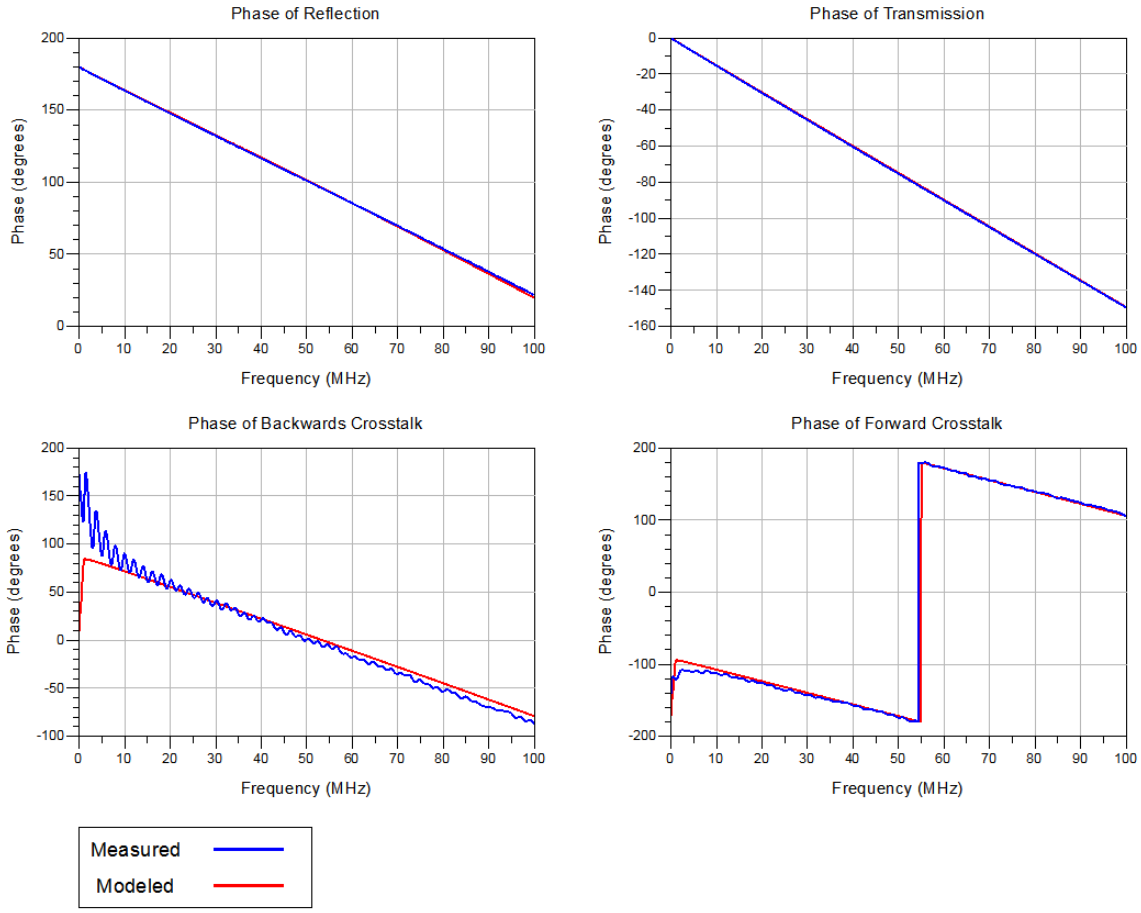

Figure 7.16: Phase of the measured S-parameters and the S-parameters of the model for FEB to LTDB transmission for the simple interconnects.

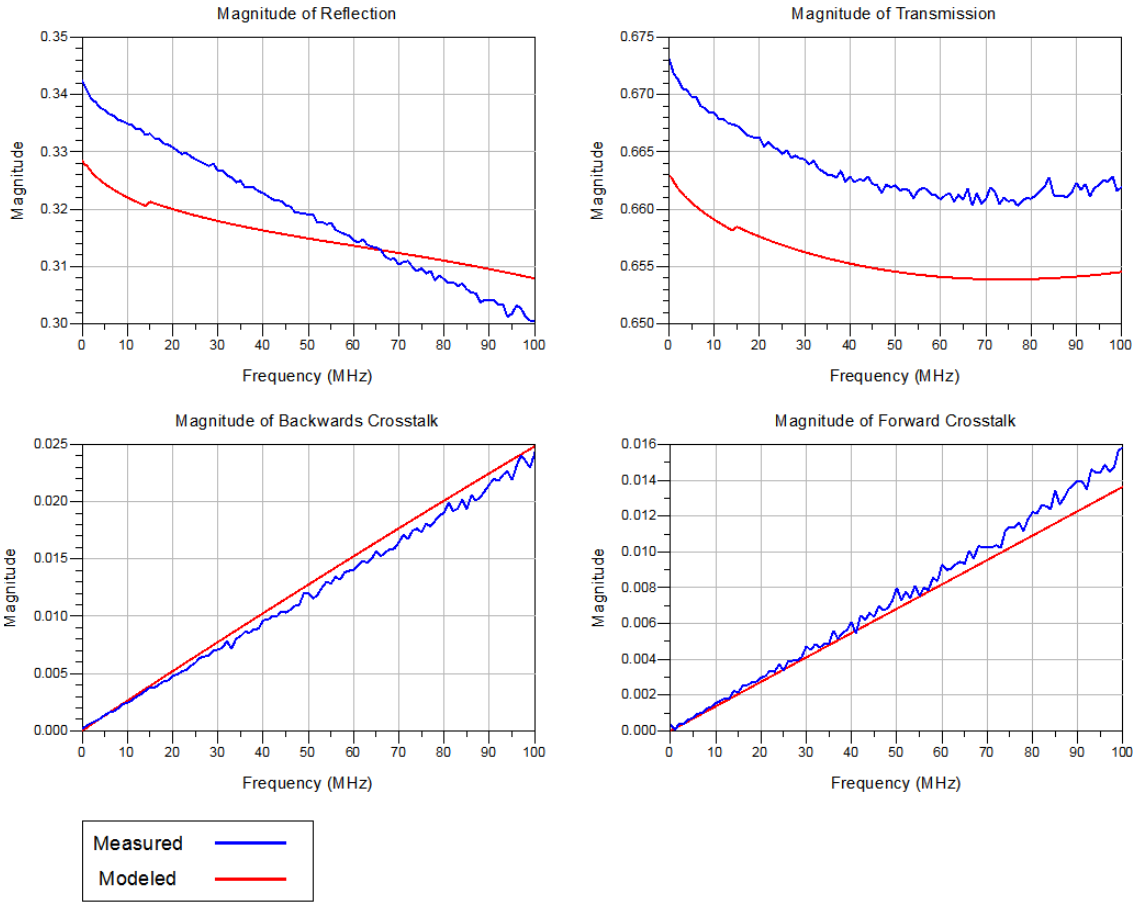

Figure 7.17: Magnitude of the measured S-parameters and the S-parameters of the model for TDB to FEB transmission for the simple interconnects. Note, the y-axis of some graphs does not start at zero in order to emphasize the observed features.

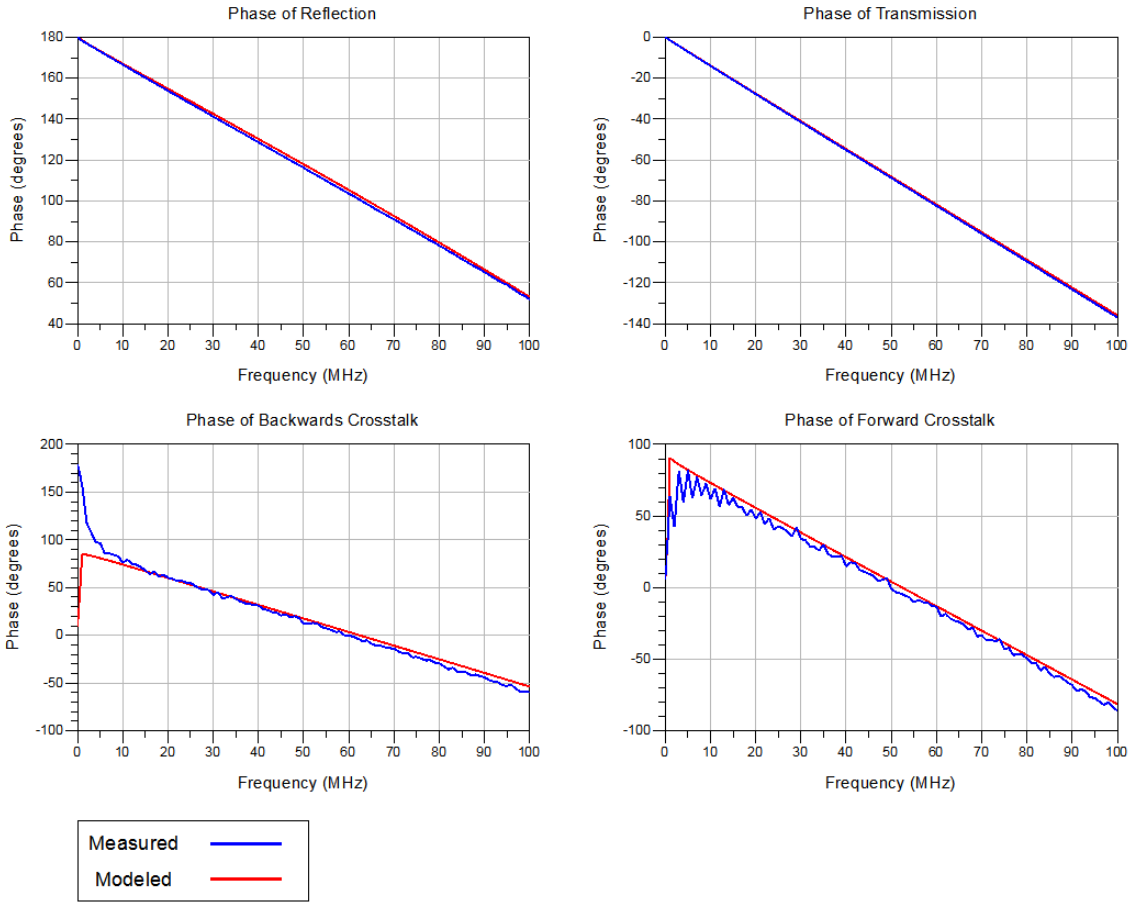

Figure 7.18: Phase of the measured S-parameters and the S-parameters of the model for TDB to FEB transmission for the simple interconnects.

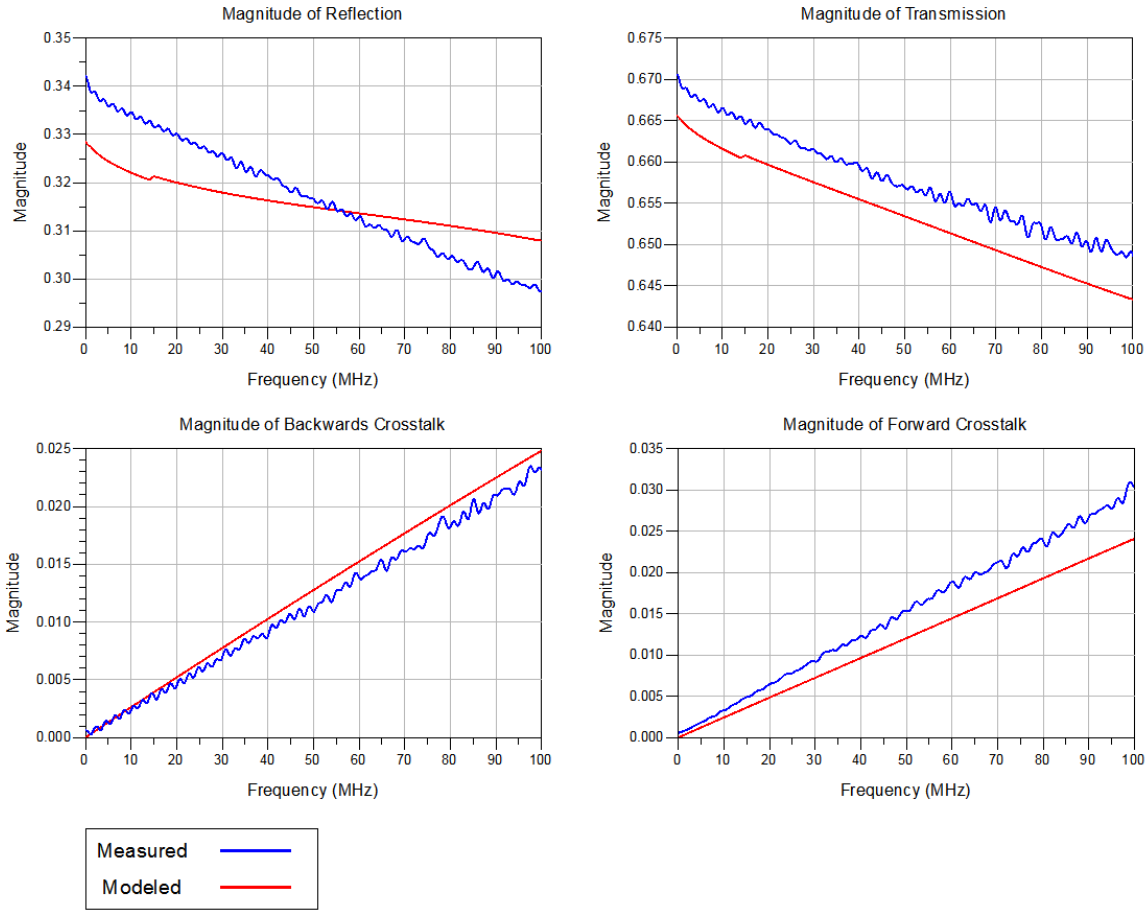

Figure 7.19: Magnitude of the measured S-parameters and the S-parameters of the model for TDB to LTDB transmission for the simple interconnects. Note, the y-axis of some graphs does not start at zero in order to emphasize the observed features.

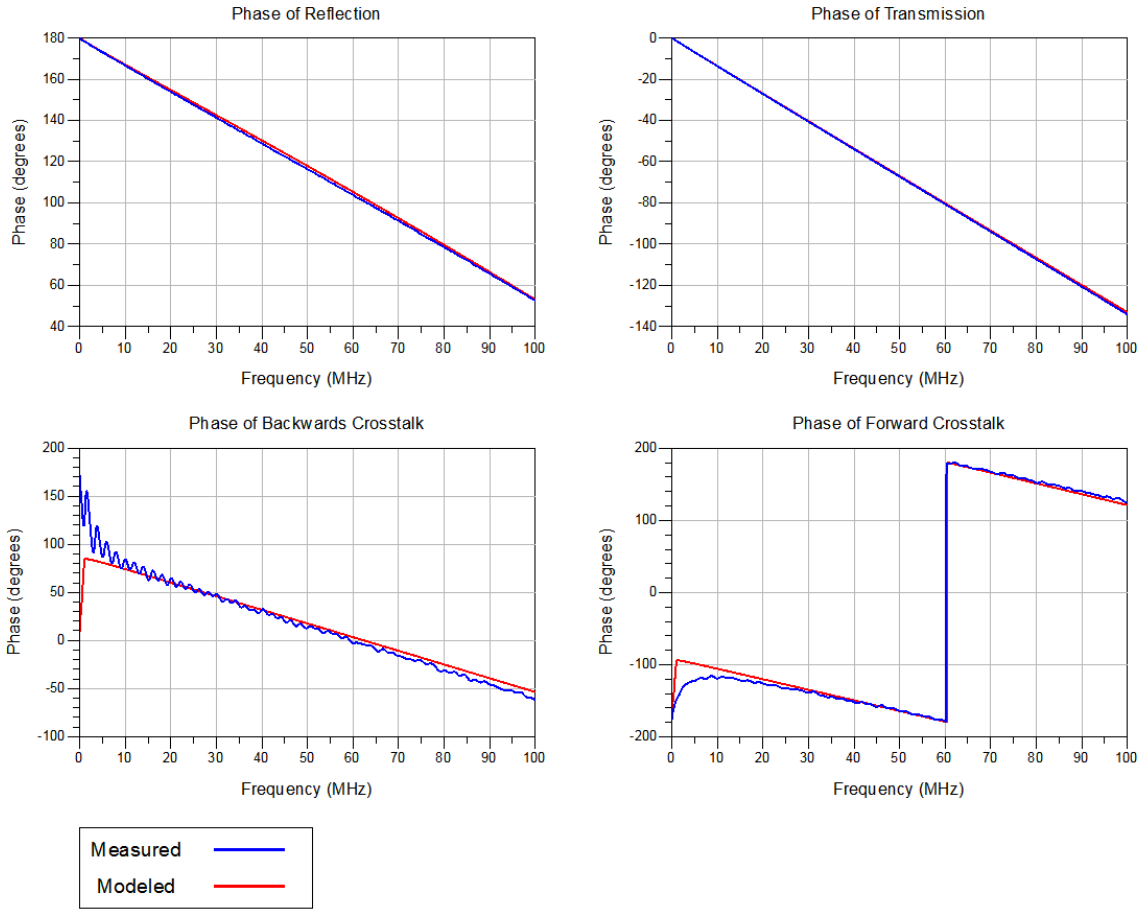

Figure 7.20: Phase of the measured S-parameters and the S-parameters of the model for TDB to LTDB transmission for the simple interconnects.

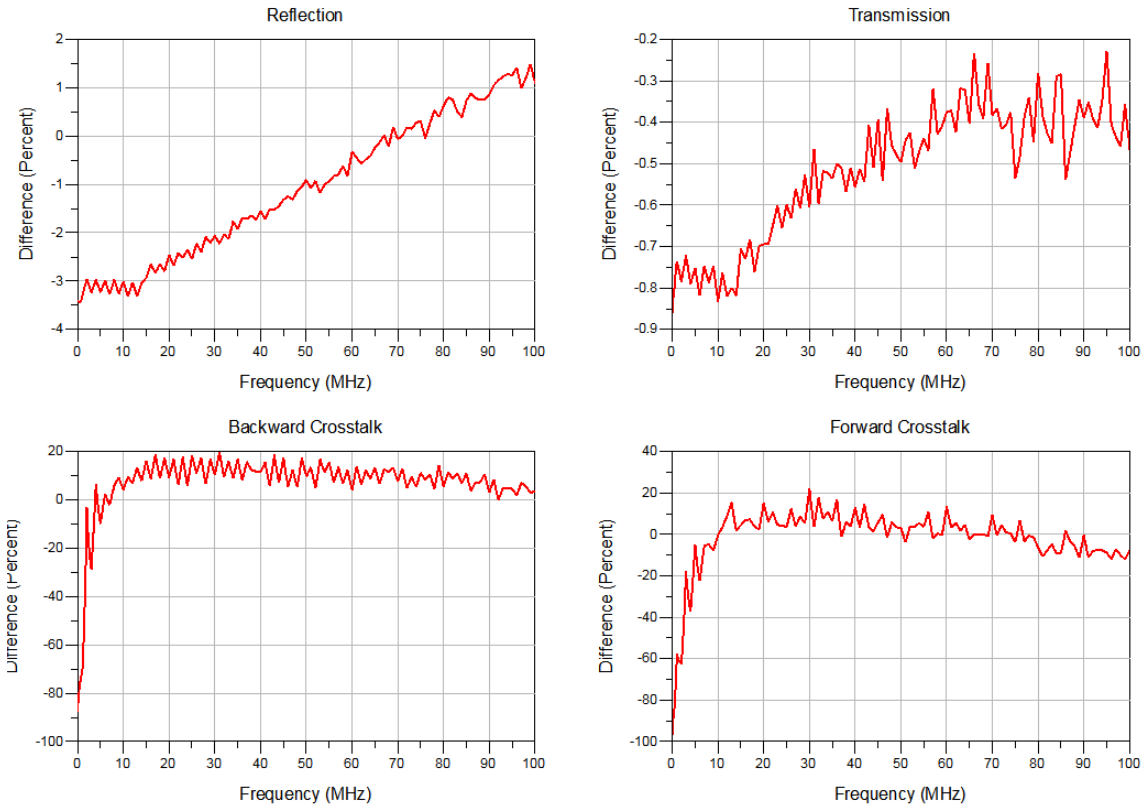

Figure 7.21: Percent difference between the magnitude of measured S-parameters and the S-parameters of the model for FEB to TDB transmission for the simple interconnects. Note, the y-axis of some graphs does not start at zero in order to emphasize the observed features.

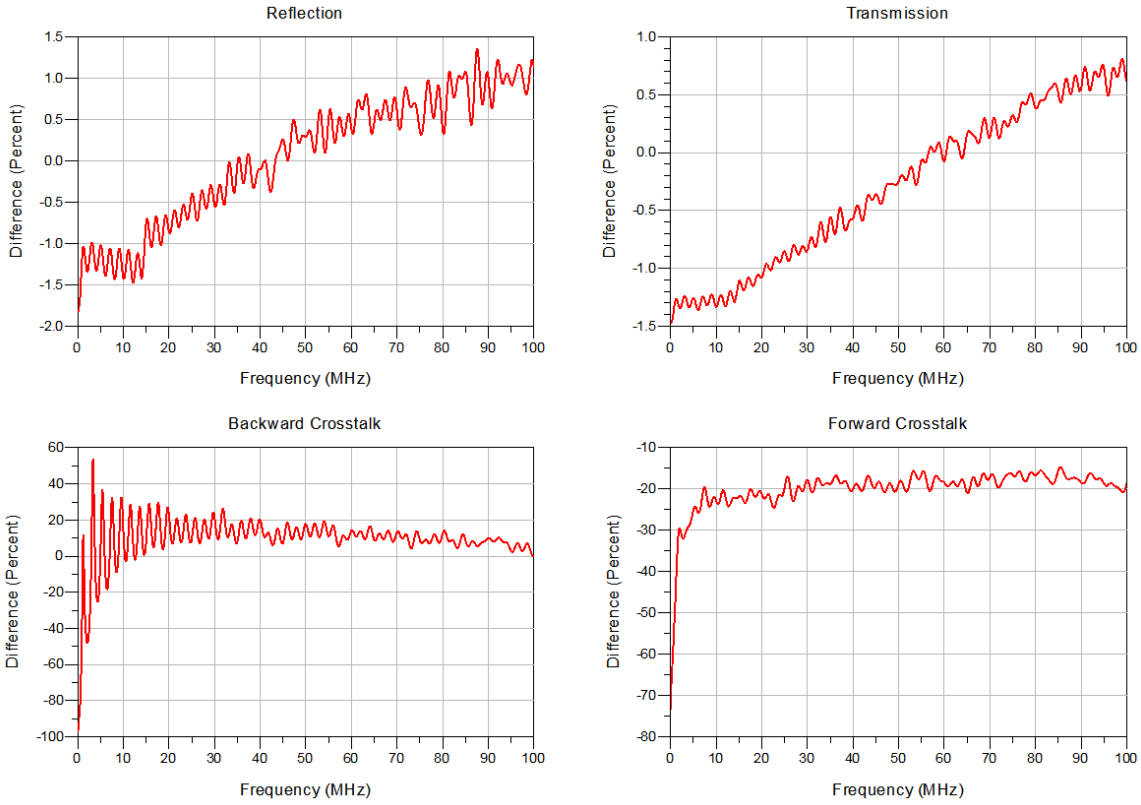

Figure 7.22: Percent difference between the magnitude of measured S-parameters and the S-parameters of the model for FEB to LTDB transmission for the simple interconnects. Note, the y-axis of some graphs does not start at zero in order to emphasize the observed features.

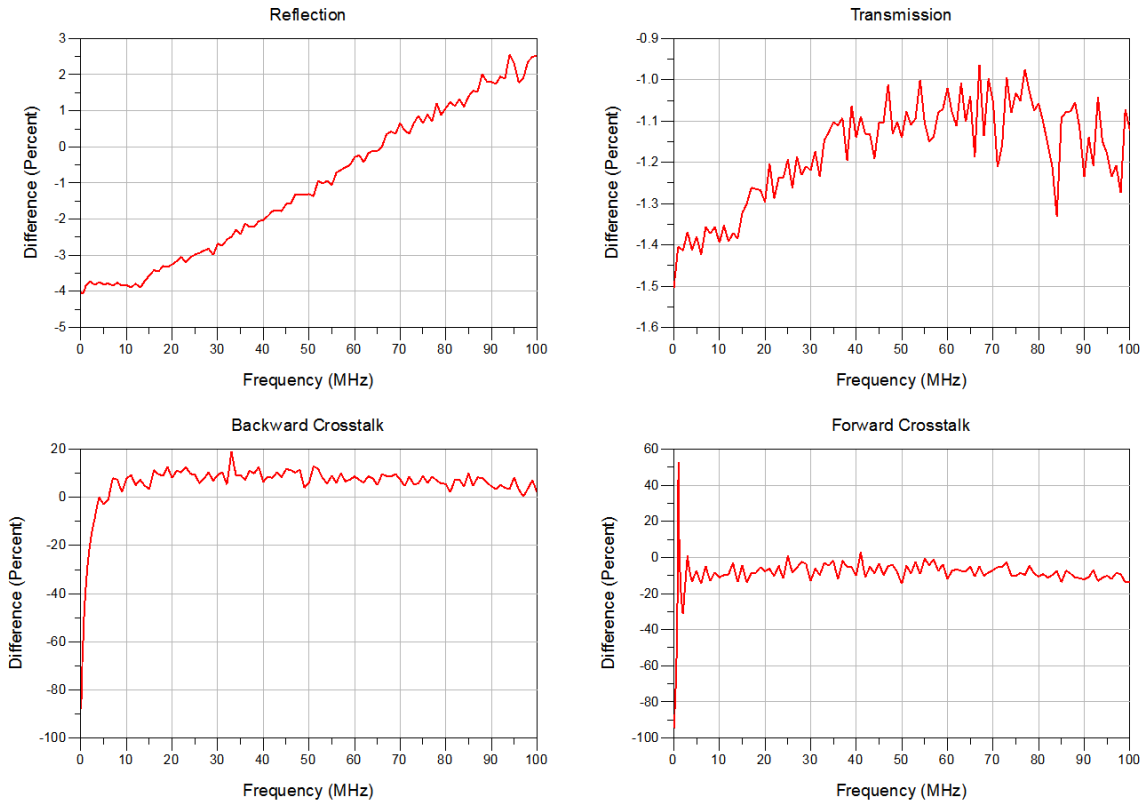

Figure 7.23: Percent difference between the magnitude of measured S-parameters and the S-parameters of the model for TDB to FEB transmission for the simple interconnects. Note, the y-axis of some graphs does not start at zero in order to emphasize the observed features.

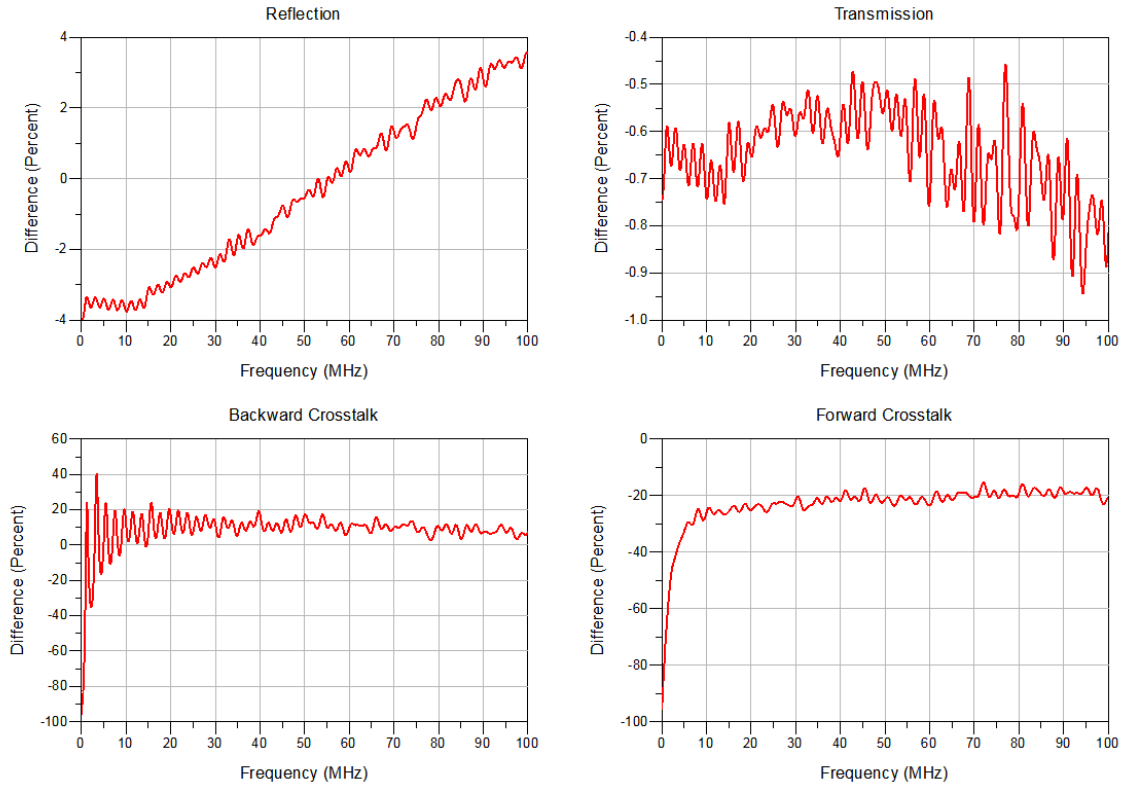

Figure 7.24: Percent difference between the magnitude of measured S-parameters and the S-parameters of the model for TDB to LTDB transmission for the simple interconnects. Note, the y-axis of some graphs does not start at zero in order to emphasize the observed features.

of non-physical ripples in the measurements (discussed in section 7.3) dominate at these low frequencies causing large percent differences. Outside of this area (above 5 MHz), the difference is always below 25%.

The phase of the simulated S-parameters are in good agreement, differing by at most 10° from the measured at 100 MHz.

Complicated Interconnects

The quality of the agreement between model and measured S-parameter is similar to simple interconnects for reflection and transmission (better than 5%). For the forward and backward crosstalk the amount of difference is similar to the simple interconnects (less than 0.01), but the forward and backward crosstalk is much smaller, increasing the percent difference to nearly 100%. Figure 7.25 and 7.26 show the magnitude and phase of the simulated and measured S-parameters for transmission from the FEB to LTDB and figure 7.27 shows the percent difference.

Adjusting the length of the ERNI connector model for the complicated interconnect may be insufficient to match the data. The female portion of the connector has a different shape than the male, shortening this segment will have more of an effect on the model than only changing the length. Adjusting other parameters of the model could lead to a better approximation of crosstalk. This study was not attempted as part of this thesis.

Overall, both the simple and the complicated interconnects are in good agreement with the measurement, suggesting the model is appropriate for both situations and that the effects of bends and via fields can be ignored. Because the ERNI connectors are the largest source of crosstalk in the baseplane, signals using row E (the longest path length in connector, see figure 7.5 on page 91) of the ERNI connector should have more crosstalk than other interconnects. This row is used for the simple interconnects, making the simple interconnect a good predictor of the maximum amount of crosstalk between interconnects of the baseplane.

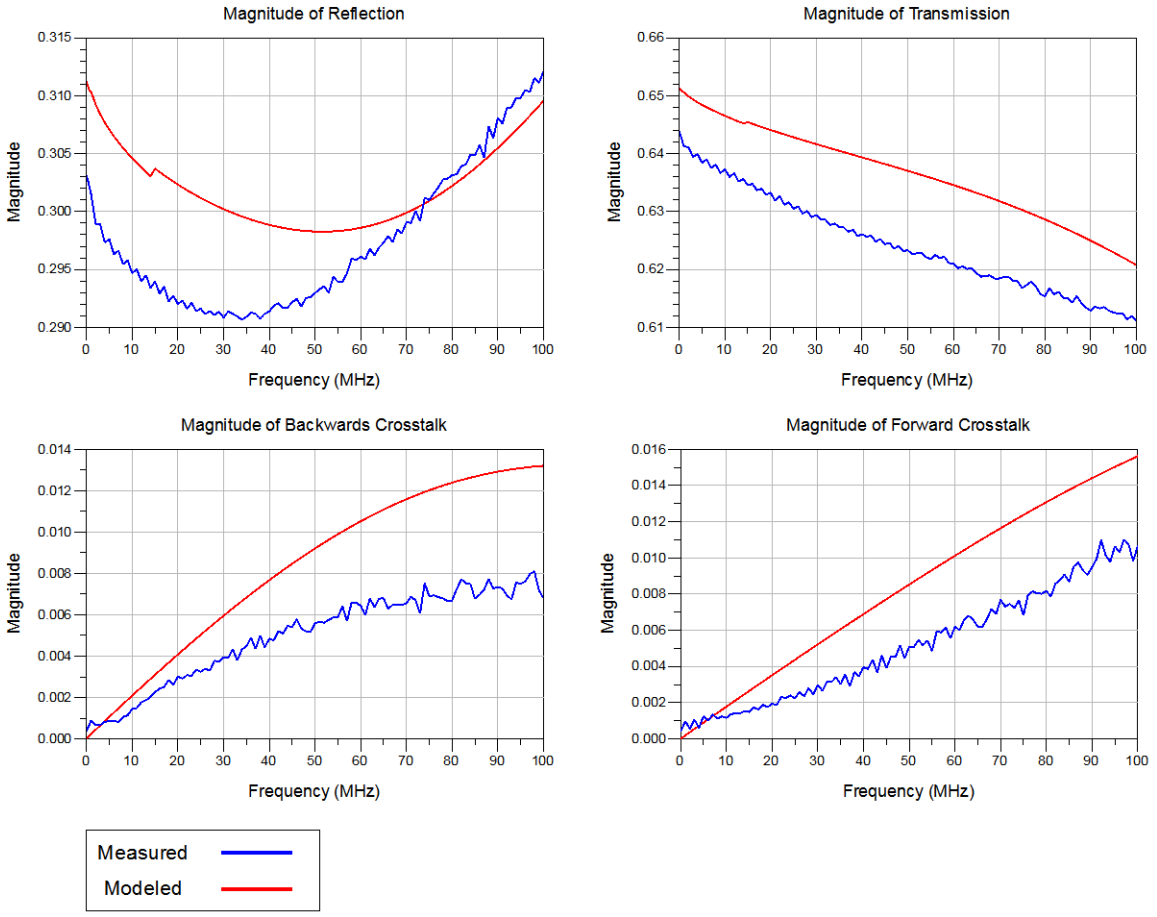

Figure 7.25: Magnitude of the measured S-parameters and the S-parameters of the model for FEB to LTDB transmission for the complicated interconnects. Note, the y-axis of some graphs does not start at zero in order to emphasize the observed features.

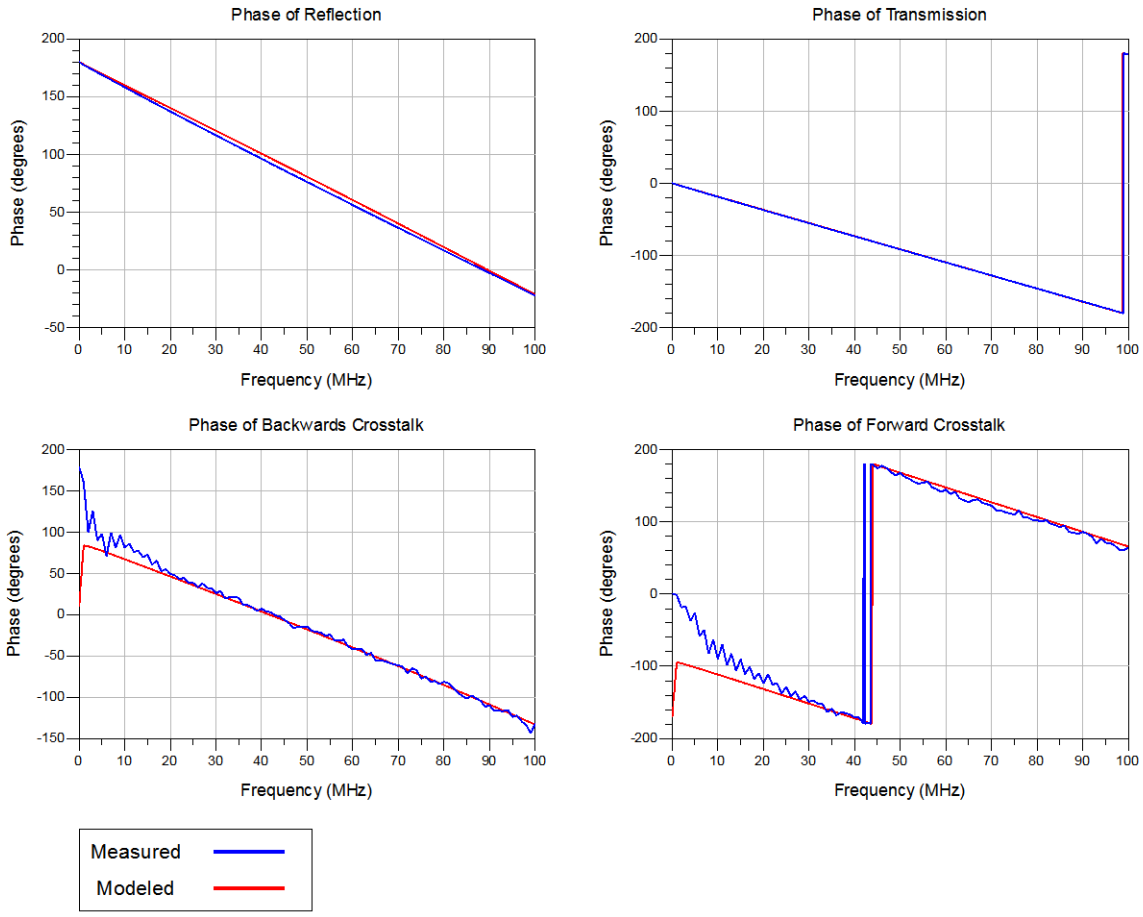

Figure 7.26: Phase of the measured S-parameters and the S-parameters of the model for FEB to LTDB transmission for the complicated interconnects. Note, the y-axis of some graphs does not start at zero in order to emphasize the observed features.

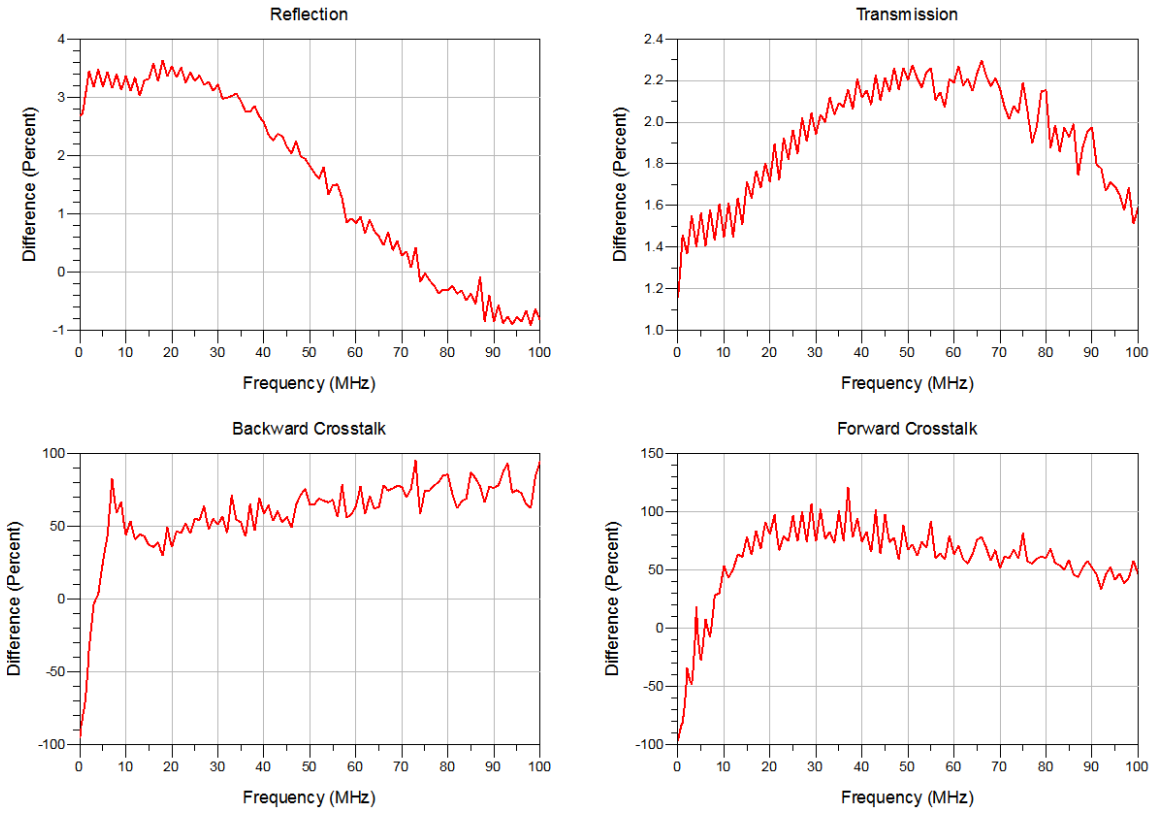

Figure 7.27: Percent difference between the magnitude of measured S-parameters and the S-parameters of the model for FEB to LTDB transmission for the complicated interconnects. Note, the y-axis of some graphs does not start at zero in order to emphasize the observed features.

Chapter 8

Results and Conclusions

This thesis creates an electrical model of two pairs of interconnects of the prototype HEC baseplane. Comparisons with measurements of prototype HEC baseplanes demonstrated the models efficacy up to 100 MHz (beyond which the frequency components of shaped Liquid Argon (LAr) Calorimeter pulse are negligible), with less than 0.02 difference in S-parameters for reflection and transmission. This corresponded to less than 5% difference from the measurements for reflection and transmission. For crosstalk the difference in S-parameters was less than 0.01, but due to the small magnitude of crosstalk, this corresponded to modeled values that range from 25% below to twice the measured values.

The model of the prototype HEC baseplane was created using several components. Keysight Technologies' Electromagnetic Professional (EMPro) was used to simulate the striplines in the baseplane using the Finite Element Method of 3D electromagnetic simulation. These models ignore bends and routing through via fields. Connectors were simulated using a built in multilayer transmission line model in Keysight Technologies' Advanced Design System (ADS). In order to make comparisons with measurements, coaxial cables were also modeled. This was done using built in coaxial cable models in ADS. ADS was used to combine all the components of the models together and calculate the S-parameters, as well as Time Domain Reflection and Transmission traces.

The measurements were made using a Tektronix' Time Domain Reflectometer (TDR). Using Tektronix' IConnect software, S-parameters were extracted from TDR measurements. It was discovered that this program could produce meaningful S-parameters when it was used to extract S-parameters of the combined system of our printed circuit boards and the patch cables used to connect the printed circuit to

the TDR. With our equipment, no other way was found to extract meaningful S-parameters of our printed circuit boards. Because S-parameter measurements could only be made of the combined patch cable and printed circuit board system, models had to include the patch cables when compared with measurements.

The techniques used for modeling and measurement were developed using a simple test board which provided a demonstration of our models efficacy. This was then applied to a subset of interconnects of the prototype HEC baseplane. The model of the prototype HEC baseplane agrees with measurements for both simple (few bends) and complicated (striplines with many bends, running through via fields) interconnects.

Ultimately, we are interested in a model of the prototype HEC baseplane that does not include the patch cables. The coaxial cable portion of the patch cable can easily be removed from the model, but the connectors have been modeled as a mated pair and are impossible to separate. Furthermore, the connectors were modeled to match the connectors of the patch cables, which may behave slightly differently than the connectors of the daughter boards (FEB, TDB and LTDB). This only affects the female (daughter board) portion of these connectors; the correct male (baseplane) connectors were included in the model. The addition of the female connectors of the patch cables will have increased the loses and crosstalk in comparison to the male connectors alone. As such, the model without the coaxial cables should overestimate the amount of the loss and crosstalk in the baseplane and the male connectors, but be a reasonable estimate of the loss and crosstalk in the baseplane with mated connectors.

The S-parameters of the model without coaxial cables are shown in figures 8.1 through 8.6. These show the magnitude and the phase of the reflection and backward crosstalk for each connector (FEB, TDB and LTDB) and the transmission and forward crosstalk from each connector to the others (simple trace, CH2 45 active, CH2 44 victim). For these S-parameters, the ports have been set to the nominal impedance for the daughter board (50 Ω for FEB and TDB, 1 kΩ for LTDB). The interconnect shown has the longest possible path through the female ERNI (LTDB) connector. Given that the ERNI connectors are responsible for most of the crosstalk in the prototype HEC baseplane, this interconnect is expected to represent the upper limit for crosstalk.

For all frequencies less than 50 MHz, the amplitude of the crosstalk is less than 0.5% of the transmitted signal. Above 50 MHz, the frequency components of shaped LAr Calorimeter pulses are negligible, so for a shaped LAr Calorimeter pulse the crosstalk is expected to be significantly less. The rise time of approximately 20 ns for

the shaped LAr Calorimeter pulse corresponds to a bandwidth of 17.5 MHz. At this frequency the crosstalk is less than 0.15%.

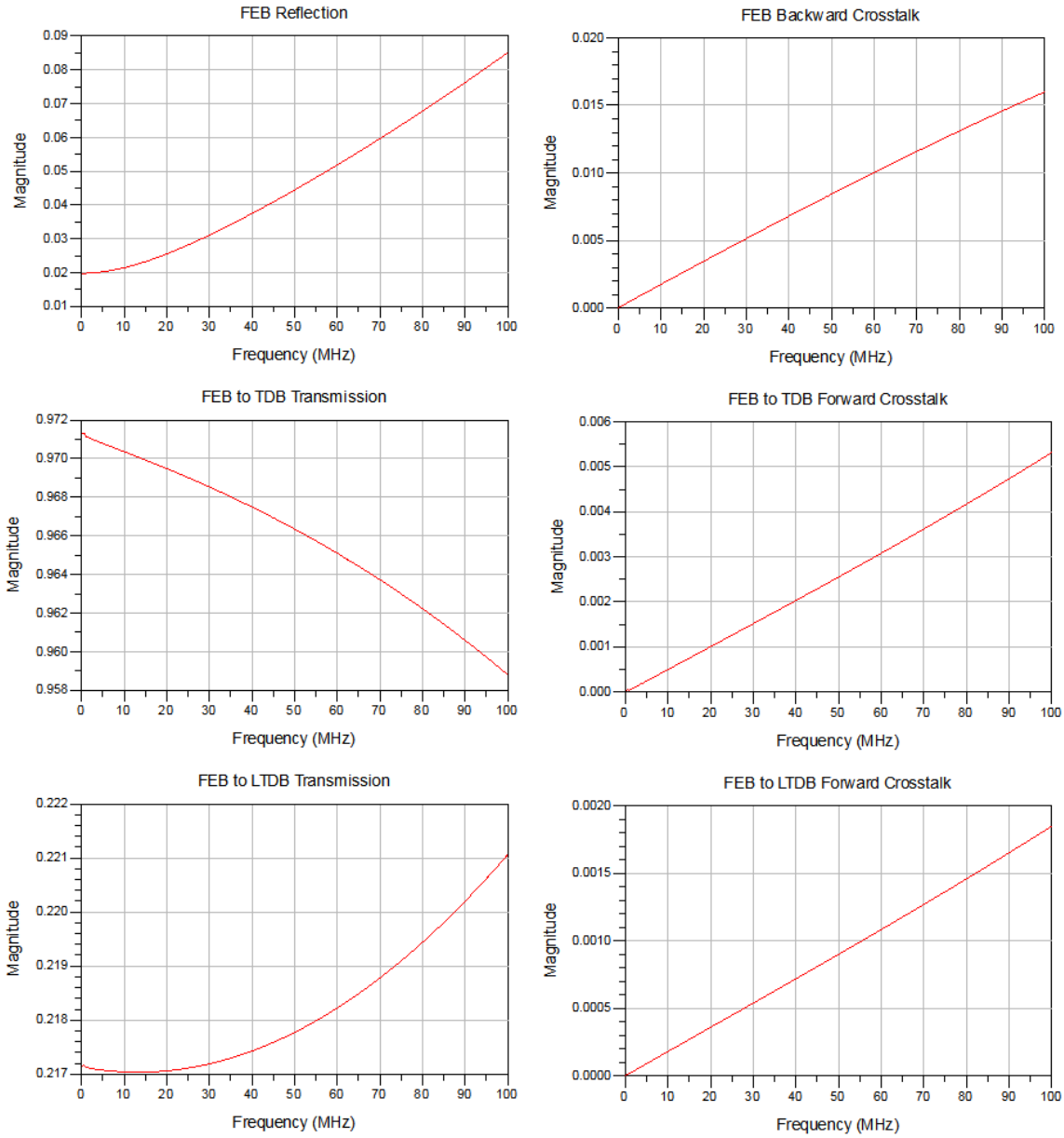

Figure 8.1: Magnitude of reflection, transmission and crosstalk for transmission from the FEB to TDB and LTDB for the simple interconnects of the prototype HEC baseplane (CH2 44 and CH2 45). Note, the y-axis of some graphs does not start at zero in order to emphasize the observed features.

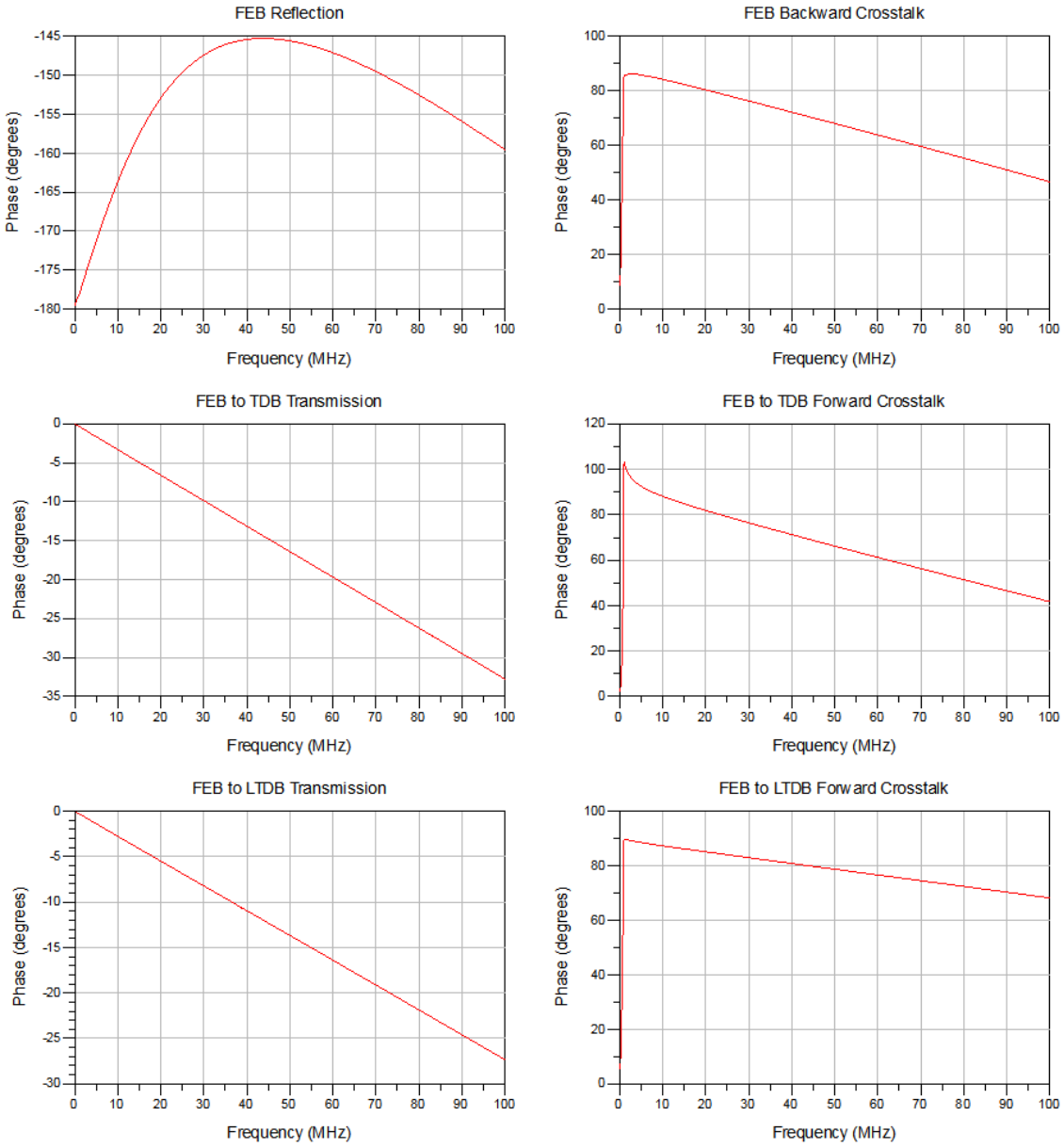

Figure 8.2: Phase of reflection, transmission and crosstalk for transmission from the FEB to TDB and LTDB for the simple interconnects of the prototype HEC baseplane (CH2 44 and CH2 45). Note, the y-axis of some graphs does not start at zero in order to emphasize the observed features.

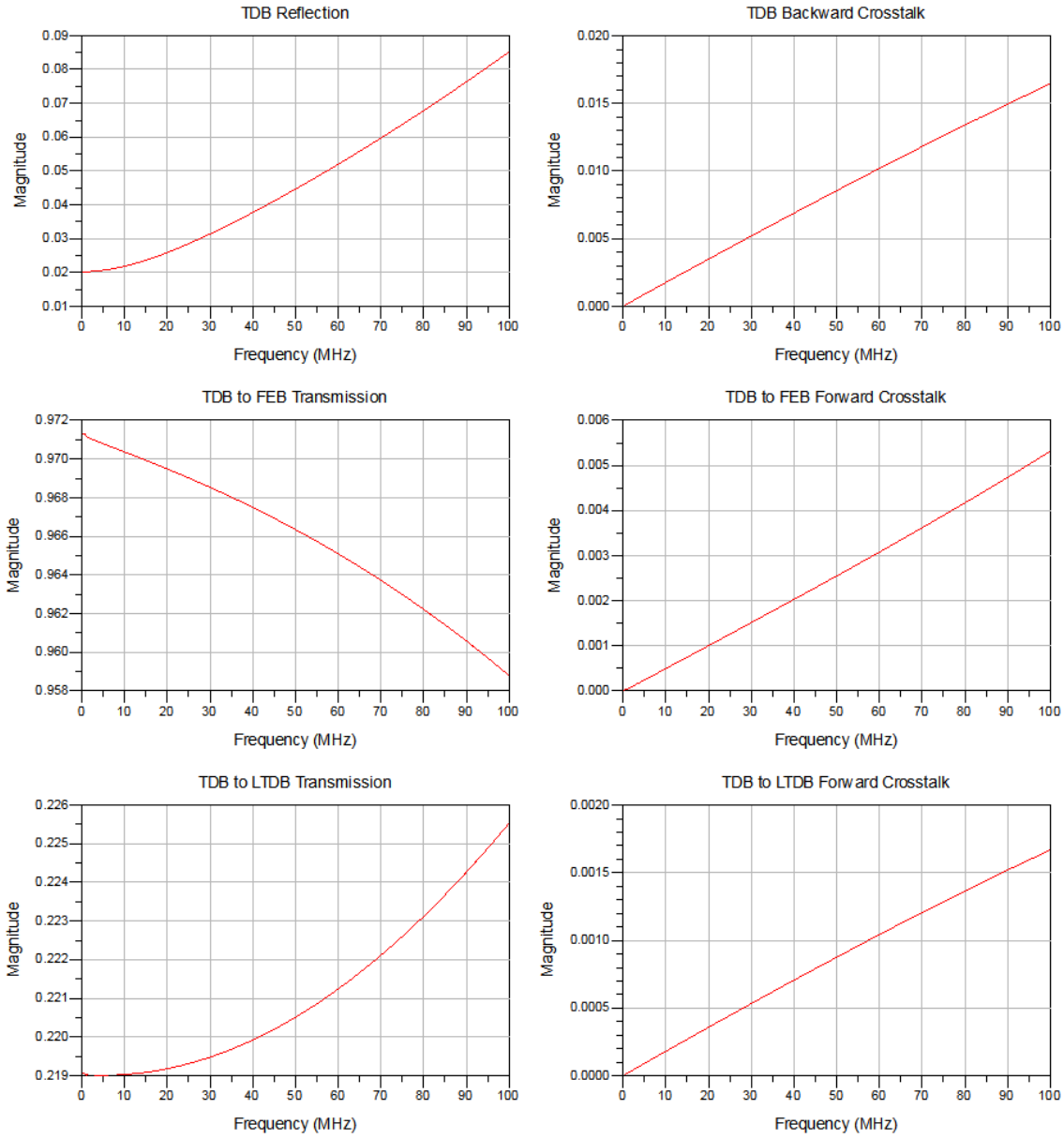

Figure 8.3: Magnitude of reflection, transmission and crosstalk for transmission from the TDB to FEB and LTDB for the simple interconnects of the prototype HEC baseplane (CH2 44 and CH2 45). Note, the y-axis of some graphs does not start at zero in order to emphasize the observed features.

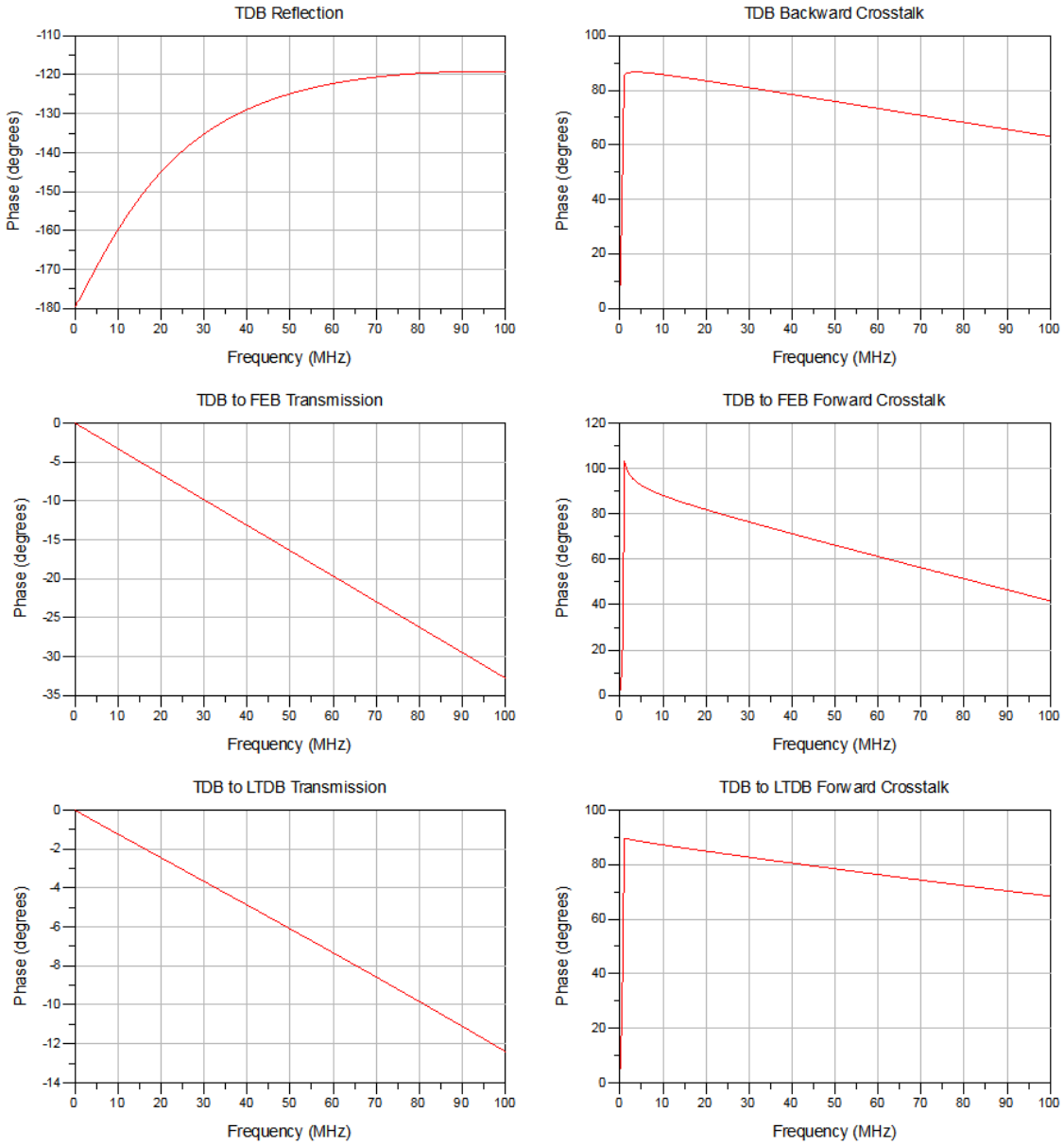

Figure 8.4: Phase of reflection, transmission and crosstalk for transmission from the TDB to FEB and LTDB for the simple interconnects of the prototype HEC baseplane (CH2 44 and CH2 45). Note, the y-axis of some graphs does not start at zero in order to emphasize the observed features.

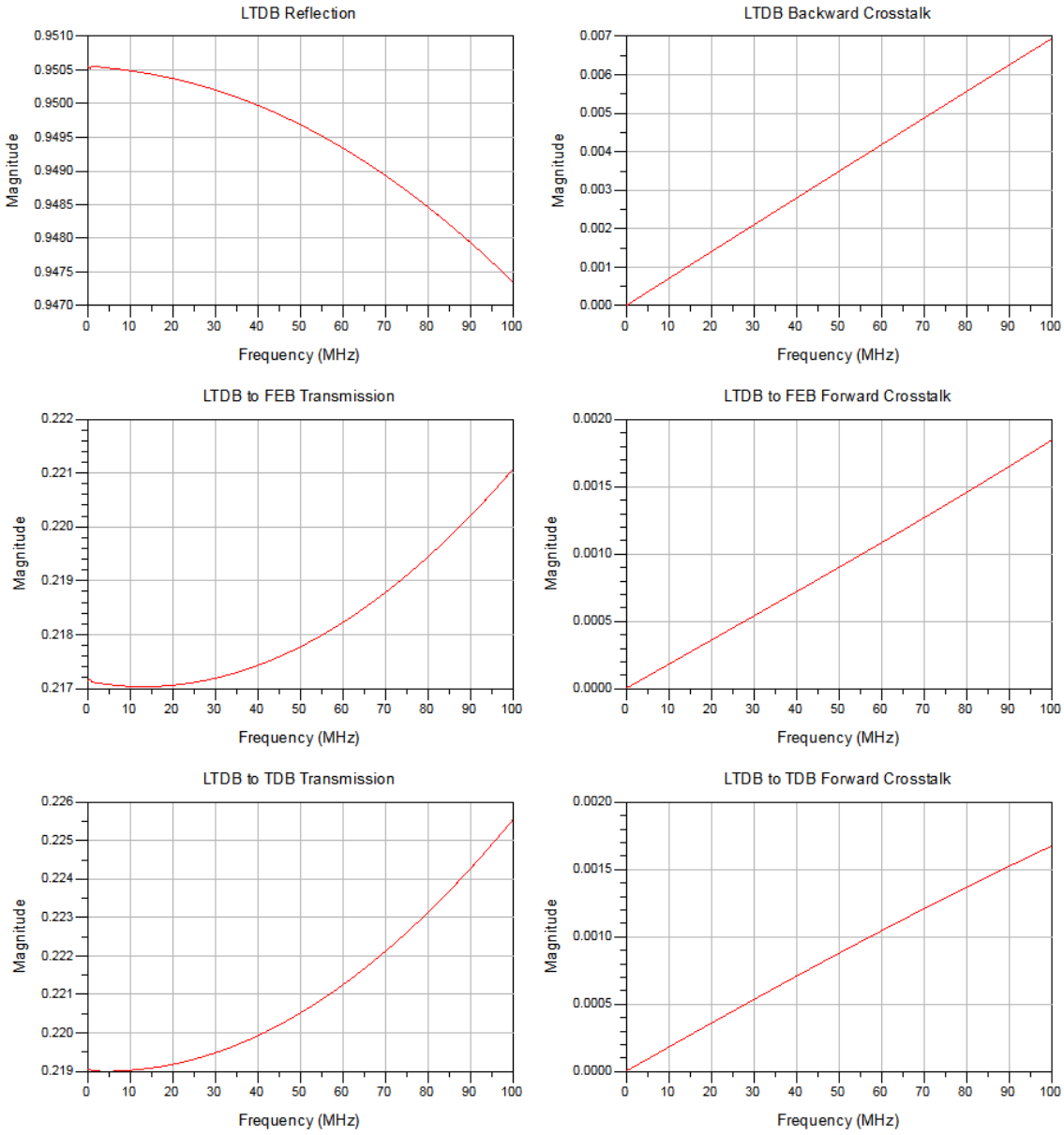

Figure 8.5: Magnitude of reflection, transmission and crosstalk for transmission from the LTDB to FEB and TDB for the simple interconnects of the prototype HEC baseplane (CH2 44 and CH2 45). Note, the y-axis of some graphs does not start at zero in order to emphasize the observed features.

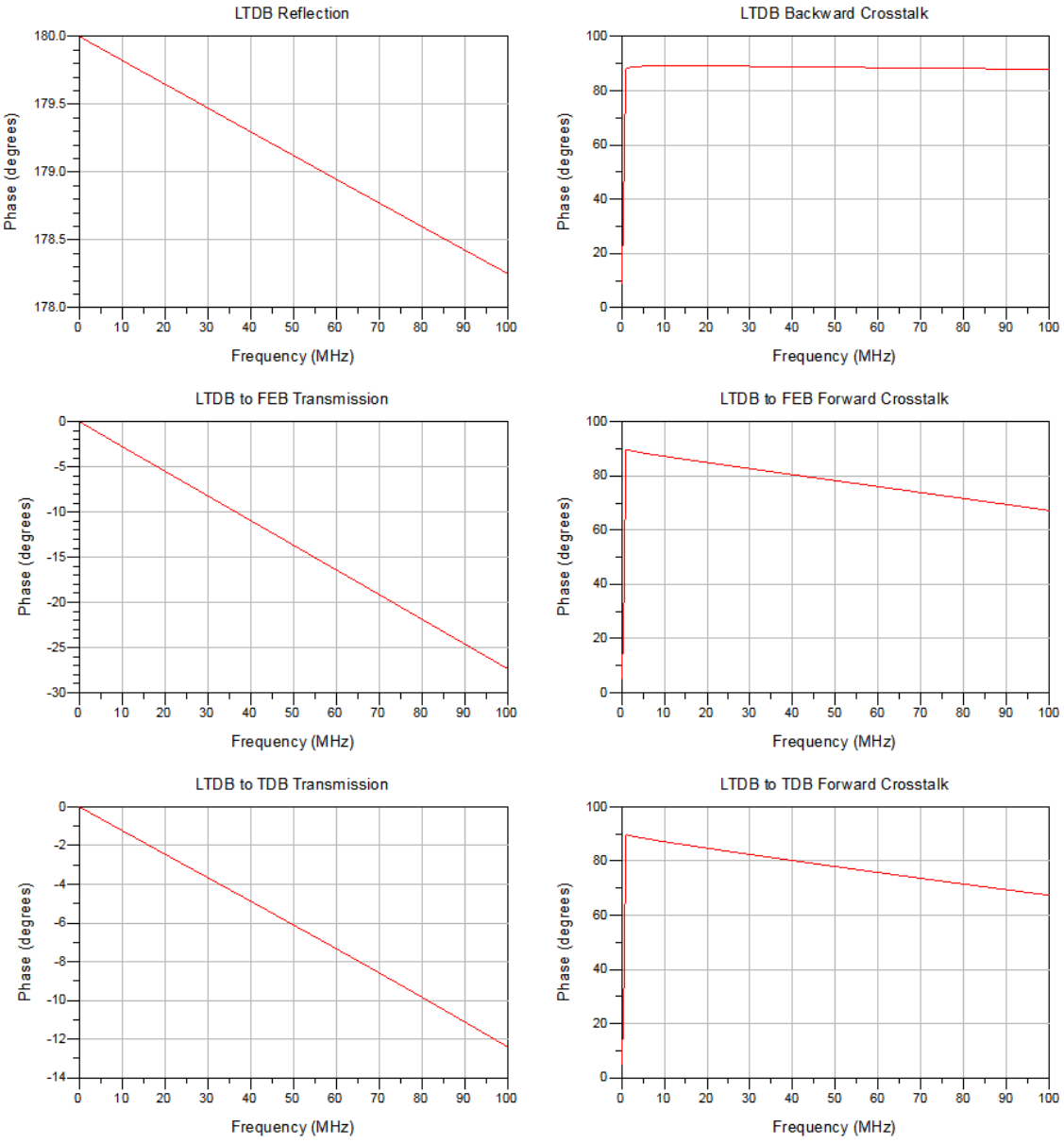

Figure 8.6: Phase of reflection, transmission and crosstalk for transmission from the LTDB to FEB and TDB for the simple interconnects of the prototype HEC baseplane (CH2 44 and CH2 45). Note, the y-axis of some graphs does not start at zero in order to emphasize the observed features.

Appendix A

Additional Information

A.1 The Finite Element Method of 3D Electromagnetic Simulation

The Finite Element Method is used to calculate the propagation of electromagnetic waves in materials [44, 39]. It is a numerical technique that can solve (using approximations) 3D electromagnetic problems of geometry for which no analytical solutions are known.

The technique begins by dividing the simulation volume into tetrahedral (in EMPro) mesh cells, called elements. A functional basis is created wherein the values between vertices in the mesh are approximated through interpolation. This approximation and calculus of variation are used to turn the differential equation into a matrix equation so that the values at the vertices can be solved for. The density of the mesh impacts the accuracy of the solutions, with the solution approaching the real value as the mesh sizes shrink to zero.

For a vector quantity, vector components are assigned in the corners of the mesh cells, pointing along the edges of the tetrahedra as in figure A.1. Because of the (minimum) 3 components for each vertex, the vectors span a 3D vector space and give both the total direction and magnitude of the vector quantity at that point. EMPro can assign two more vectors at the midpoint of each edge. These lie parallel to the faces and perpendicular to the edges of the tetrahedra.

The vector-values at points inside the volume are approximated by interpolation (linear or other). Using this approximation, Maxwell's equation can be manipulated into matrix relations between vectors, where one of the vectors is a list of all vector

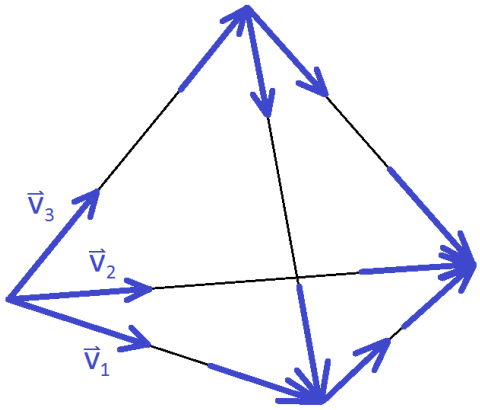

Figure A.1: An example of tetrahedral mesh cell for an FEM simulation of a vector quantity. Each corner has three vector components along the edge of the cells.

components for all points in the a mesh cell for all cells in the mesh.

Bibliography

[1] ATLAS Collaboration, "Observation of a new particle in the search for the standard model higgs boson with the ATLAS detector at the LHC," *Phys. Lett. B*, vol. 716, pp. 1 – 29, 2012.

[2] D. Griffiths, *Introduction to Elementary Particles*. Wiley-VCH, 2004.

[3] Liquid Argon Collaboration, *ATLAS Liquid Argon Calorimeter Phase-1 Upgrade Technical Design Report*. 2013.

[4] ATLAS Collaboration, *The ATLAS Experiment at the CERN Large Hadron Collider*. Institute of Physics Publishing and SISSA, 2008.

[5] ATLAS Collaboration, *ATLAS Letter of Intent Phase-1 Upgrade*. 2011.

[6] L. Evans and P. Bryant, *LHC Machine*. Institute of Physics Publishing and SISSA, 2008.

[7] CMS Collaboration, "Observation of a new boson at a mass of 125 GeV with the CMS experiment at the LHC," *Phys. Lett. B*, vol. 716, pp. 30 – 61, 2012.

[8] CMS Collaboration, *The CMS Experiment at the CERN Large Hadron Collider*. Institute of Physics Publishing and SISSA, 2008.

[9] LHCb Collaboration, *The LHCb Experiment at the CERN Large Hadron Collider*. Institute of Physics Publishing and SISSA, 2008.

[10] ALICE Collaboration, *The ALICE Experiment at the CERN Large Hadron Collider*. Institute of Physics Publishing and SISSA, 2008.

[11] TOTEM Collaboration, *The TOTEM Experiment at the CERN Large Hadron Collider*. Institute of Physics Publishing and SISSA, 2008.

[12] LHCf Collaboration, *The LHCf Experiment at the CERN Large Hadron Collider*. Institute of Physics Publishing and SISSA, 2008.

[13] MoEDAL Collaboration, "Technical design report of the MoEDAL experiment," Tech. Rep. CERN-LHCC-2009-006. MoEDAL-TDR-001, CERN, Geneva, Jun 2009.

[14] I. Vichou, "Performance of missing transverse momentum reconstruction in ATLAS with proton-proton collisions at $\sqrt{s} = 7$ TeV," *J. Phys. Conf. Ser.*, vol. 404, p. 012011, 2012.

[15] B. Aubert et al., "Construction, assembly and tests of the ATLAS electromagnetic barrel calorimeter," *Nucl.Instrum.Meth.*, vol. A558, pp. 388–418, 2006.

[16] M. Aleksa et al., "Construction, assembly and tests of the ATLAS electromagnetic end-cap calorimeters," *JINST*, vol. 3, p. P06002, 2008.

[17] ATLAS Collaboration, "ATLAS tile calorimeter: Technical design report," 1996.

[18] D. M. Gingrich, G. Lachat, J. Pinfold, J. Soukoup, D. Axen et al., "Construction, assembly and testing of the ATLAS hadronic end-cap calorimeter," *JINST*, vol. 2, p. P05005, 2007.

[19] A. Artamonov et al., "The ATLAS Forward Calorimeters," *JINST*, vol. 3, p. P02010, 2008.

[20] ATLAS Collaboration, "ATLAS liquid argon calorimeter: Technical design report," 1996.

[21] N. J. Buchanan et al., "ATLAS liquid argon calorimeter front end electronics," *JINST*, vol. 3, p. P09003, 2008.

[22] N. J. Buchanan et al., "Design and implementation of the front end board for the readout of the ATLAS liquid argon calorimeters," *JINST*, vol. 3, p. P03004, 2008.

[23] J. Colas et al., "Electronic calibration board for the ATLAS liquid argon calorimeter," *Nuclear Instruments and Methods in Physics Research A*, vol. 593, no. 3, pp. 267–291, 2008.

[24] C. W. Davidson, *Transmission Lines for Communications with CAD programs*. Macmillan Education Ltd, 1989.

[25] R. Collier, *Transmission Lines*. Cambridge University Press, 2013.

[26] T. C. Edwards and M. B. Steer, *Foundation of Interconnect and Microstrip Designs*. John Wiley & Sons, Inc., 3 ed., 2000.

[27] A. R. von Hippel, *Dielectrics and Waves*. John Wiley & Sons, Inc., 1954.

[28] D. B. Jarvis, "The effects of interconnections on high-speed logic circuits," *IEEE Trans. on Electronic Computers*, pp. 476–487, Oct. 1963.

[29] Hewlett-Packard Company, "Application note 62 time domain reflectometry," 1964.

[30] Hewlett-Packard Company, "Application note 62-1 improving time domain network analysis measurements," 1988.

[31] Hewlett-Packard Company, "Application note 62-3 advanced tdr techniques," 1990.

[32] T. Quarles, D. Pederson, R. Newton, A. Sangiovanni-Vincentelli and C. Wayne, "The SPICE page." URL: http://bwrcs.eecs.berkeley.edu/Classes/IcBook/SPICE/, Accessed: 2015-04-04.

[33] Sunstone Circuits, "PCBExpress Quickturn," 2014. URL: http://www.sunstone.com/pcb-products/pcbexpress-quickturn.

[34] Sunstone Circuits, "PCBExpress Quickturn PCB Construction Detail." URL: http://www.sunstone.com/pcb-products/pcbexpress-quickturn/quickturn-pcb-construction, Accessed: 2015-04-04.

[35] CINCH Connectivity Solutions, "SMA straight plug to SMA straight plug cable assembly, RG316 cable 415-0029-024," 2014. URL:https://cinchconnectivity.com/, Accessed:2015-05-29.

[36] Tektronix, Inc., "IConnect ® and MeasureXtractor ^{TM} TDR and VNA Software Version 4.0 User Manual," 2007.

[37] Agilent Technologies, "EMPro 2012 overview," 2012.

[38] Agilent Technologies, "EMPro 2012 geometry modeling," 2012.

[39] Agilent Technologies, "EMPro 2012 FEM simulation," 2012.

[40] Keysight Technologies, "ADS overview 2015.01," 2015.

[41] C. Railton and J. McGeehan, "An analysis of microstrip with rectangular and trapezoidal conductor cross sections," *IEEE Transactions on Microwave Theory and Techniques*, vol. 38, no. 8, pp. 1017–1022, 1990.

[42] T. Hasegawa, K. Atsuki, K. Li, and E. Yamashita, "An analysis of striplines with trapezoidal conductor cross sections," *Electronics and Communications in Japan*, vol. 78, no. 1, pp. 41–51, 1994.

[43] ERNI Electronics, "Catalog E 2.0 mm ERmet Hard Metric Connector System," 2010.

[44] T. Itoh, G. Pelosi and P. P. Silvester, *Finite Element Software for Microwave Engineering*. John Wiley & Sons, Inc., 1996.